

JAERI-M

8 6 2 2

IAEA INTOR WORKSHOP REPORT, GROUP3

— IMPURITY CONTROL, FUELING AND EXHAUST —

January 1980

Fusion Research and Development Center

日本原子力研究所
Japan Atomic Energy Research Institute

この報告書は、日本原子力研究所が JAERI-M レポートとして、不定期に刊行している研究報告書です。入手、複製などのお問い合わせは、日本原子力研究所技術情報部（茨城県那珂郡東海村）あて、お申しこしください。

JAERI-M reports, issued irregularly, describe the results of research works carried out in JAERI. Inquiries about the availability of reports and their reproduction should be addressed to Division of Technical Information, Japan Atomic Energy Research Institute, Tokai-mura, Naka-gun, Ibaraki-ken, Japan.

IAEA INTOR Workshop Report, Group 3
- Impurity Control, Fueling and Exhaust -

Fusion Research and Development Center,
Tokai Research Establishment, JAERI

(Received December 11, 1979)

The data bases of impurity control, fueling and exhaust for INTOR plasma are assessed. They include permissible levels of impurities, experimental results of plasma-wall interactions, specific means for decreasing plasma contamination, impurity control and ash exhaust with and without divertor, fueling by gas puffing and pellet injection, and related surface phenomena.

Key words: INTOR, Tokamak Reactor, Impurity Control, Ash Exhaust, First Wall, Plasma-Wall Interaction, Fueling, Divertor Effect, Data Base Assessment

Prepared by: Teruhiko TAZIMA (Group leader), Tetsuya ABE, Toshio HIRAYAMA, Koji KAMADA[†]), Masao KASAI^{*1}), Tetsuzan KUROKI, Koichi MAKI^{*2}), Hiroo NAKAMURA, Yukiharu NAKAMURA, Kiyoshi SAKO, Kazuho SONE, Kichiro SHINYA^{*3}), Norio SUZUKI, Seio SENGOKU, Yasushi SEKI, Yasuo SHIMOMURA, Masayoshi SUGIHARA, Reiji YAMADA.

†) Division of Physics, Tokai Research Establishment, JAERI.

*1) On leave from Mitsubishi Atomic Power Industries Inc.

*2) On leave from Hitachi, Ltd.

*3) On leave from Toshiba, Corp.

日本原子力研究所東海研究所核融合開発推進センター

(1979年12月11日受理)

INTOR プラズマを検討するに必要な, 不純物制御, 燃料補給, 灰除去に関するデータベースの評価を行った。これらの評価は, 不純物の許容レベル, プラズマと第1壁との相互作用の実験結果, プラズマへの不純物混入を減らす手段, ダイバータのある系とない系での不純物制御と灰除去, ガス注入かペレット入射による燃料補給および関連する表面現象のデータ等を含むものである。

執筆者 田島 輝彦 (グループリーダー)・阿部 哲也・平山 俊雄・
鎌田 耕治⁺・笠井 雅夫^{*1)}・黒木 鉄山・真木 紘一^{*2)}
中村 博雄・中村 幸治・迫 淳・曾根 和穂・
新谷 吉郎^{*3)}・鈴木 紀男・仙石 盛夫・関 泰・下村 安夫・
杉原 正芳・山田 礼司

+) 東海研究所物理部

*1) 外来研究員; 三菱原子力工業 (株)

*2) 外来研究員; 日立製作所 (株)

*3) 外来研究員; 東京芝浦電気 (株)

CONTENTS

(edited by T. Tazima)

1. INTRODUCTION & SUMMARY (T. Tazima)	1
1.1 Short Burn or Long Burn?	1
1.2 Plasma Contamination by Sorbed Impurities on the Wall Surfaces	1
1.3 Plasma Contamination by First Wall Materials	2
1.4 Ash Exhaust	3
1.5 What Roles Should Divertor Play?	3
1.6 Divertor or Non-Divertor?	4
1.7 Heat and Particle Flux to the First Wall and the Divertor Plate	5
2. PERMISSIBLE LEVELS OF IMPURITIES (Y. Nakamura, T. Hirayama, T. Tazima)	10
2.1 Evaluation of Radiation Losses	10
2.2 Effects of Impurity Diffusion and Plasma Distribution on Impurity Radiations	10
3. EXPERIMENTAL RESULTS OF PLASMA-WALL INTERACTIONS	18
3.1 Impurity Production	18
1) Metallic impurity production (Y. Shimomura, N. Suzuki)	18
2) Experiments of low Z limiters in JFT-2 (T. Hirayama)	23
3) Experiments of low Z materials in DIVA (DIVA Group)	27
3.2 Recycling of Plasma Particles (T. Hirayama)	34
4. SPECIFIC MEANS FOR DECREASING PLASMA CONTAMINATION	37
4.1 Wall Conditioning to Reduce Sorbed Impurities (T. Tazima, T. Hirayama)	37
4.2 Effects of Low Z Materials (H. Nakamura, T. Abe, R. Yamada)	52
5. DIVERTOR CASE FOR IMPURITY CONTROL & ASH EXHAUST	58
5.1 Results of Divertor Experiment in DIVA (Y. Shimomura, DIVA Group)	58
5.2 A Simple Poloidal Divertor with Exterior Coils (Y. Shimomura, K. Sako, K. Shinya)	70
5.3 Numerical Calculations of Helium Ash Enrichment and Exhaust by a Simple Poloidal Divertor (Y. Seki, Y. Shimomura, K. Maki)	74

5.4	Impurity Production and Recycling in the Scrape-Off Plasma of a Large Tokamak (S. Sengoku)	87
6.	NON-DIVERTOR CASE FOR IMPURITY CONTROL & ASH EXHAUST (T. Tazima, M. Sugihara)	94
6.1	"Wall Lapping Plasma" with Rotating Resonant Helical Islands and Mechanical Valves for Ash Exhaust	94
7.	FUELING	100
7.1	Gas Puffing (T. Tazima, M. Kasai, M. Sugihara)	100
7.2	Pellet Injection (T. Kuroki)	101
8.	DATA BASE ON SURFACE EFFECTS (K. Sone, K. Kamada)	105

目 次

1. 序論および概要 (田島輝彦)	1
1.1 プラズマ燃焼時間	1
1.2 壁面に収着された不純物によるプラズマ汚染	1
1.3 第一壁材料によるプラズマ汚染	2
1.4 灰除去	3
1.5 ダイバーターの役割	3
1.6 ダイバーター系と非ダイバーター系	4
1.7 第一壁とダイバーター板への熱流束と粒子束	5
2. 不純物の許容混入量 (中村幸治, 平山俊雄, 田島輝彦)	10
2.1 放射損失の評価	10
2.2 不純物拡散とプラズマ分布の不純物による放射への影響	10
3. プラズマと第一壁との相互作用の実験結果	18
3.1 不純物発生	18
1) 金属不純物発生 (下村安夫, 鈴木紀男)	18
2) JFT-2での低原子番号リミター材の実験 (平山俊雄)	23
3) DIVAでの低原子番号材の実験 (DIVAグループ)	27
3.2 プラズマ粒子のリサイクリング (平山俊雄)	34
4. プラズマ汚染を減らす方法	37
4.1 収着不純物を減らすための壁表面処理 (田島輝彦, 平山俊雄)	37
4.2 低原子番号材の効果 (中村博雄, 阿部哲也, 山田礼司)	52
5. ダイバーターのある場合の不純物制御と灰除去	58
5.1 DIVAでのダイバーター実験結果 (下村安夫, DIVAグループ)	58
5.2 外部コイル付単純ポロイダルダイバーター (下村安夫, 迫 淳, 新谷吉郎)	70
5.3 単純ポロイダルダイバーターによるヘリウム灰蓄積と除去の数値計算 (関 泰, 下村安夫, 真木絃一)	74
5.4 大型トカマクのスクレイプオフプラズマでの不純物生成とリサイクリング (仙石盛夫)	87
6. ダイバーターのない系での不純物制御と灰除去	94
6.1 不純物制御用の回転ヘリカル共鳴磁気島及び灰除去用機械的バルブを備えた “壁面攪動プラズマ” (田島輝彦, 杉原正芳)	94
7. 燃料補給	100
7.1 ガス注入 (田島輝彦, 笠井雅夫, 杉原正芳)	100
7.2 ペレット注入 (黒木鉄山)	101
8. 表面現象に関するデータベース (曾根和徳, 鎌田耕治)	105

1. INTRODUCTION & SUMMARY

Impurity control and ash exhaust are one of the most serious problems in INTOR. It is not clear whether we can control impurities sufficiently even in a case with the divertor. There are many unsolved problems as to impurity control as described below, but possible countermeasures can be imagined most of which have not been proved at present and should be tested in the next several years. Especially, high heat load to the divertor plate and/or the limiter is most stringent in INTOR which, unfortunately, will not be investigated even in the large Tokamak machines such as JET, JT-60, TFTR and T-15 because of their small heat load and short duration time.

1.1 Short Burn or Long Burn?

As long as we employ the burn time longer than 30 seconds, physical requirements for impurity control and ash exhaust are not different between short burn and long burn. It is because that impurities accumulate to the saturated level within the time several times longer than particle confinement time τ_p (i.e. it is shorter than 20 s, if $\tau_p = 1 \sim 5$ s), ashes accumulate to 10 % concentration of the plasma density within 20 s, and surface temperature of the first wall (including limiter and/or divertor plate) is saturated within 10 ~ 20 s.

Therefore, we should aim at long burn as long as possible, since we should sufficiently control impurities and ashes in any case of short burn or long burn.

1.2 Plasma Contamination by Sorbed Impurities on the Wall Surfaces

To obtain a clean surface of the first wall is the most simple and reliable countermeasure to the plasma contamination by sorbed impurities as proved in today's experiments. Consequently, requirements for divertor will be extremely mitigated.

In order to obtain the clean surface, many kinds of surface treatments before assembly such as surface polishing to remove absorbed impurities, and after assembly such as degreasing, baking, discharge cleaning and in-situ coating to remove adsorbed impurities are necessary. By such treatments, oxygen as main impurities were reduced down to 1 ~ 2 % of the electron density. However it is found difficult to reproduce such condition

for many successive shots except the cases where sufficient Ti gettering or Ti gettering between discharges were employed. However a frequent use of Ti gettering will result in the exfoliation of coated layers. Therefore, it is important to find means of maintaining sufficiently clean surfaces for a long time. To meet this requirement, it should be necessary to reduce impurity flows from diagnostic instruments and NBI sources, backstreaming from evacuating systems, and outgassing from walls not facing the plasma.

1.3 Plasma Contamination by First Wall Materials

More severe problem will be the contamination by first wall materials due to sputtering, self-sputtering, evaporation, and surface erosions.

Experimental results in DIVA show that

- (i) the self sputtering of the metallic impurity ions accelerated by the sheath potential near the limiter surface is the major mechanism of metallic impurity recycling in ordinary discharges,
- (ii) the evaporation of the limiter surface takes place by local deposition of high energy electrons in low density discharges,
- (iii) and evaporation by arcing in an unstable discharge or in the case of a dirty limiter surface.

The magnetic limiter has a powerful shielding effect to metallic impurities even in the case of a low concentration of light impurities where, in general, the metallic impurity concentration will increase by the strong interaction of the plasma with the limiter because edge-cooling by light impurities is reduced.

In large tokamaks with higher temperatures and longer duration times, there will be other production mechanisms;

- (iv) a large energy flow from the plasma will cause the evaporation of the limiter surface when the contact area of the limiter is not sufficiently enlarged,
- (v) the sputtering of the first wall materials by charge-exchange neutrals escaping from the plasma with a temperature of the order of keV will not be neglected, even though the high energy neutrals at the center cannot escape because of their short mean free paths,
- (vi) furthermore, in an additional heating phase by NBI, the orbit loss of fast ions and escaping charge-exchange neutrals during the slowing down process, especially the latter, will sputter the first wall,

(vii) in an initial phase of NBI, if 10 ~ 20 % of the beam flux will pass through the plasma, it can cause surface damages on the surface facing the beam such as grain ejection and blistering where anomalous erosion rates have been observed.

1.4 Ash Exhaust

Required ash exhaust efficiency ξ is estimated as

$$\xi \left[\frac{\bar{n}_\alpha}{\tau_\alpha} \right] V = c \frac{1}{4} \bar{n}^2 \bar{\alpha}_f V$$

where c is increase factor of fusion power in distributed plasma (e.g. $c = 1.8$ in parabolic distribution), mean fusion production rate $\bar{\alpha}_f \sim 10^{-22}$ m^3/s at 10 keV. We assume the particle confinement time of α particles $\tau_\alpha \sim \tau_p \sim \tau_E$.

$$\text{Then } \xi \sim \left[\frac{\bar{\alpha}_f}{2} \right] \bar{n} \left[\frac{\bar{n}_\alpha}{\bar{n}} \right]^{-1} \tau_p$$

If we employ $\bar{n} = 1.2 \times 10^{20}/\text{m}^3$, $\tau_p = 1 \sim 2$ s and allow 10 % of ash accumulation, i.e. $(\bar{n}_\alpha/\bar{n}) \sim 0.1$, $\xi = (5 \sim 10) \times 10^{-2}$. Therefore, we should exhaust only 5 ~ 10 % of α particles flow escaping from the plasma and it seems rather easy to pump out such particles. However, ash exhaust will become difficult with long τ_p .

1.5 What Roles Should Divertor Play?

Although the roles of divertor in common sense are exhaust of

- heat,
- gas impurities,
- fuel particles,
- sputtered and/or evaporated first wall materials,
- ashes.

It is possible to attain and keep a clean surface of the first wall, and realize a plasma free from contamination by gas impurities such as oxygen. Recycling and/or fueling neutrals will cause sputtering the first wall materials through charge-exchange process which can be suppressed employing suitable materials (e.g. low Z one) or suitable structures (e.g. honeycomb one) of the first wall, and metallic and also carbon

impurities stick easily onto the vacuum surface. Therefore, an artificial pumping system is not necessary for gas impurities, fuel particles, and metallic impurities. The pumping system only for ash exhaust is necessary.

1.6 Divertor or Non-Divertor?

1) Divertor

Most promising divertors are simple poloidal divertor with exterior coils and improved bundle divertor as summarized below.

	Advantages	Disadvantages	Measures	Problem
simple poloidal divertor	<ul style="list-style-type: none"> •small power consumption •simple coil 	<ul style="list-style-type: none"> •small heat unload •hardly-repairable divertor plate 	<ul style="list-style-type: none"> •spreading the scrape-off layer by ergodization and flux swinging 	<ul style="list-style-type: none"> •design of divertor plate
bundle divertor	<ul style="list-style-type: none"> •large heat unload •easily-repairable divertor plate 	<ul style="list-style-type: none"> •large power consumption •large ripple diffusion •complicated coil 	<ul style="list-style-type: none"> •4-6 number of large toroidal coils 	<ul style="list-style-type: none"> •drastic change of machine structure

We employ a simple poloidal divertor with exterior coils. Major results are:

- (i) At least a half of plasma particles and ash flows will backflow from the inside divertor chambers to the main plasma but the outside divertor chambers which have pumping ports will sufficiently play a role of ash enrichment and exhaust.
- (ii) Impurities emitted from the divertor plate hardly backflow to the main plasma.
- (iii) Heat load to the divertor plate will be $80 - 150 \text{ w/cm}^2$ which is under technological limitation for heat removal as long as we employ refractory metal for the plate material, but high heat deposition on the edge of the divertor plate is still stringent.
- (iv) Shielding effect of the divertor for fuel particles is not powerful as well as for impurities emitted from the wall. Therefore, gas puffing might be still applicable for fueling even in the case with the divertor.

2) "Wall Lapping Plasma" as an alternative of the divertor

In any case, the divertor will cause technological difficulties. It is very important to develop alternative ideas of the divertor. As non-divertor case, we propose "Wall Lapping Plasma" with rotating resonant helical islands for impurity control and mechanical valves for ash exhaust. At present, we cannot put on priority such alternatives, since they have not been tested in experiments, but they should be tested in next several years in actual devices.

1.7 Heat and Particle Flux to the First Wall and the Divertor Plate

Heat and particle flux to the first wall and the divertor plate is calculated for various cases both by time dependent 1D simulation code and by steady state calculation of density profile. We include the inward flow by Ware pinch effect in particle flow and others are same as guiding model, i.e. electron thermal conductivity $\chi_e = 5 \times 10^{19}/n_e$, ion thermal conductivity $\chi_i = 3(\chi_i)_{neoclas.}$, and diffusion coefficient $D = \chi_e/12$.

The following profile of the temperature has been employed in the steady state calculation;

$$T_e(r) = T_i(r) = [T(0) - T(a)] \left[1 - \left(\frac{r}{a}\right)^4\right]^{2.5} + T(a).$$

Actually, however, we found that the results of the calculations are insensitive to the temperature profile. Changing the amount of the fuel source (gas puffing and/or pellet), we searched steady state solutions of density profile, which given neutron wall loading of about 1 MW/m². In 1D simulation code, recycling of helium is not considered, while steady state code calculates both recycling and no recycling cases of helium. Both codes take account of the recycling of fuel particles (D,T). However, only mono energetic neutrals are considered, so that recycling hot neutrals and cold neutrals of gas puffing cannot be treated simultaneously. Since steady state calculations do not solve energy balance equations, the solved state is not necessarily consistent with self-sustaining state from the view point of power balance.

The results are summarized in Table 1 for 1D simulation calculations, and in Table 2 for steady state calculations. Cases I-5 and I-6 give results of sharp density profile by a deep pellet injection which, however, may be unrealistic. The cases with 50 % recycling of fuel particles

correspond to a simple poloidal divertor case (e.g. I-2, II-4). Gas puffing case corresponds to "Wall Lapping Plasma" (e.g. I-1, II-1-3). The case with no-recycling of both fuel particles and helium particles corresponds to an ideal divertor case (e.g. I-3, II-5).

Overall helium particle confinement time τ_{He} obtained in no helium recycling cases (e.g. I, II-2) represents the confinement time of helium ash in bulk plasma, so that the concentration of helium should be determined by this τ_{He} (i.e. $N_{\text{He}} = \tau_{\text{He}} \times S_{\alpha}$, where S_{α} is source of helium particles). Although in most cases of 1D simulation calculations, the ash accumulation f is considerably large, this is due to excessively large source of α -particles (i.e. excessively large α -particle power P_{α}). In fact, when we reset P_{α} to the target value of 90 MW, the accumulation f^* ($f^* = f \times 90/P_{\alpha}$) is below 10 % in most cases. The accumulation of ash is determined by $f = N_{\text{He}}/N_i = \tau_{\text{He}} P_n / N_i a$ (P_n : neutron wall loading, a : plasma minor radius). If we assume $\tau_{\text{He}} \propto a^2$, then $f \propto a P_n / N_i$. Thus, if $a P_n$ value of commercial reactor becomes 3 ~ 4 times larger than INTOR value, $f = 30 \sim 40$ % even though all of the helium particles diffusing from the bulk plasma are completely exhausted, so that the ash accumulation will become a serious problem unless we have margin of beta value.

Notations

- τ_p : Overall fuel particle confinement time.
- τ_{He} : Overall helium ash confinement time.
- Γ_p : Out flux of fuel ions.
- Γ_{He} : Out flux of helium ash.
- Γ_{cx} : Out flux of neutral particles (mainly by charge exchange).
- \bar{E}_{cx} : Average energy of outflux neutral particles.
- T_{n0} : Energy of neutrals.
- P_{cx} : Total power loss by charge exchange.
- P_r : Total power loss by radiation (including bremsstrahlung, synchrotron).
- P_{α} : Total α -heating power.
- P_{tr} : Total power loss by transport.
- f : Fraction of helium ash ($f = \bar{n}_{\text{He}}/\bar{n}_i$)
- f^* : Fraction of helium ash with P_{α} being normalized to 90 MW (i.e., $f^* = f \times 90/P_{\alpha}$).
- ⊛ 1 : This value cannot be obtained, since energy balance equations are not solved in steady-state calculations.

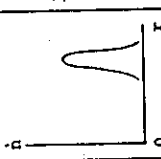
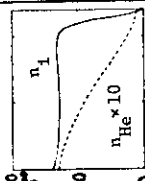
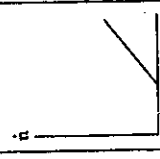
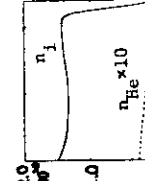
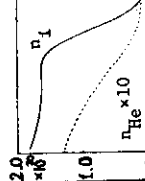
⊗ 2 : Not converged for helium.

Note: Power loss P_{cx} , P_r , P_α , P_{tr} are calculated for noncircular plasma
(i.e., $V_p = 213 \text{ m}^3$, $S_p = 302 \text{ m}^2$)

Table 1

I. 1D Simulation Code		Particle source profile	Recycling of fuel particles	Density profile in nearly steady-state	Plasma parameters	Recycling of He	τ_p (sec)	τ_{He} (sec)	Γ_p ($1/m^2 s$)	Γ_{He} ($1/m^2 s$)	Γ_{cx} ($1/m^2 s$)	\bar{E}_{cx} (keV)	P_{cx} (MW)	P_r (MW)	P_a (MW)	P_{tr} (MW)	Case															
Recycling case	100 %		500 eV		$\bar{n}_i = 24.7$ (keV) $\bar{n}_i = 1.2 \times 10^{20}$ ($1/m^3$) $\bar{n}_{He} = 1.8 \times 10^{19}$ ($1/m^3$) $f = 15\%$ ($f^* = 7\%$) $(t = 22.6s)$	0 %	0.9	10	8.2×10^{19}	1.1×10^{18}	6.2×10^{19}	6.0	14.2	17.5	184	167	(I-1)															
																		50 %		$T_i = 11.1$ $\bar{n}_i = 1.1 \times 10^{20}$ $\bar{n}_{He} = 8.3 \times 10^{18}$ $f = 7.5$ ($f^* = 8$) $(t = 18s)$	0 %	1.0	12	6.5×10^{19}	4.1×10^{17}	1.5×10^{19}	1.5	2.0	10.5	84	73.5	(I-2)
	50 %		500 eV	$T_i = 11.7$ $\bar{n}_i = 1.3 \times 10^{20}$ $\bar{n}_{He} = 2.2 \times 10^{19}$ $f = 17$ ($f^* = 9$) $(t = 33s)$	0 %	2.4	15	3.4×10^{19}	8.8×10^{17}	1.0×10^{19}	3.1	2.3	38	175	133	(I-4)																
																	0 %		$T_i = 11.8$ $\bar{n}_i = 1.4 \times 10^{20}$ $\bar{n}_{He} = 2.5 \times 10^{19}$ $f = 18$ ($f^* = 7$) $(t = 35s)$	0 %	3.8	16	2.2×10^{19}	9.4×10^{17}	-	-	53	237	178.5	(I-5)		
																															0 %	
Pellet injection case		500 eV	0 %		$T_i = 11.8$ $\bar{n}_i = 1.4 \times 10^{20}$ $\bar{n}_{He} = 5.0 \times 10^{19}$ $f = 36$ ($f^* = 6.2$) $(t = 21s)$	0 %	10.0	21	8.1×10^{18}	1.4×10^{18}	-	-	234	520	273	(I-6)																

Table 2

II. Steady State Solution		Particle source profile	Recycling of fuel particles	Density profile in nearly steady-state	Plasma parameters	Recycling of He	τ_p (sec)	τ_{He} (sec)	Γ_p ($1/m^2 s$) ($1/m^2 s$)	Γ_{He} ($1/m^2 s$) ($1/m^2 s$)	Γ_{CX} ($1/m^2 s$) ($1/m^2 s$)	E_{cx} (keV)	P_{cx} (MW)	P_r (MW)	P_a (MW)	Plasma Case
Recycling case	100 %		T=500eV n_0		$\bar{T}_i=10.3$ (keV) $\bar{n}_i=1.15 \times 10^{20}$ ($1/m^3$) $\bar{n}_{He}=5.1 \times 10^{18}$ ($1/m^3$) $f=4.4\%$ ($f^*=4.6$)	0.89	0.31	1.25	2.3×10^{20}	2.5×10^{18}	7.9×10^{19}	0.7	4.1	6.9	87	(II-1)
Pellet injection case	50%		5 eV n_0		$\bar{T}_i=9.8$ $\bar{n}_i=1.27 \times 10^{20}$ $\bar{n}_{He}=5.9 \times 10^{18}$ $f=6.9$ ($f^*=6.6$)	0.63	0.21	$\Phi 2$	3.7×10^{20}		1.43×10^{20}	0.1	1.0	9.2	93	(II-3)
	0 %		0 %		$\bar{T}_i=9.9$ $\bar{n}_i=1.05 \times 10^{20}$ $\bar{n}_{He}=4.0 \times 10^{18}$ $f=3.8$ ($f^*=4.3$)	0.58	0.76	3.2	8.22×10^{19}	7.6×10^{17}	-	-	-	6.9	80	(II-5)

2. PERMISSIBLE LEVELS OF IMPURITIES

2.1 Evaluation of Radiation Losses

Radiation losses due to various impurities from reactor-grade plasma give rise to a severe problem and many theoretical and/or experimental investigations on this problem have been made. In particular, high Z impurities such as tungsten, molybdenum and iron cause their strong radiation even in high temperature plasmas of multi-keV, since their atomic ions are not fully ionized and the valence electrons emit a large number of photons.

Tazima et al.¹⁾ estimated the radiation power due to such as carbon, oxygen and iron, including the effect of the impurity diffusion. Jensen et al.²⁾ numerically calculated the impurity radiation using an "average-ion model". The comparison of the steady state (coronal equilibrium) ionic species of oxygen and iron have been performed and give the results that an "average-ion model" is well established in the estimation of impurity radiation of the moderate atomic number (See Fig. 1, 2). Although "average-ion model" gives the radiation due to the impurities of higher atomic number such as molybdenum, tungsten and gold, further investigations are necessary as to precise atomic data of high Z atomic ions, since these calculations have not been proved in experiments.

2.2 Effects of Impurity Diffusion and Plasma Distribution of Impurity Radiations

We calculate oxygen and iron radiation including impurity diffusion and this shows that the impurity diffusion affects the total impurity radiation. The much reduction of charge state from coronal equilibrium due to impurity diffusion increases the impurity radiation from tokamak plasmas. The impurity diffusion effects on that radiation is conspicuous near the plasma edge, in this region the impurity charge state is under the ionizing phase balanced by the impurity diffusion.

In the estimation of impurity radiation from a given plasma parameter, total impurity radiation is influenced significantly by the radial distribution of the electron temperature and density. In Case A (where temperature and its gradient are low and moderate in the boundary region, but high and steep in the central region), significant amount of partially ionized impurity ions is distributed in the boundary region and excitation

loss in this region due to those ions is much larger than bremsstrahlung loss from the center region (see Table 1, and Fig. 2-(a) as the case of O). On the other hand in Case B (parabolic distribution case), most of impurity ions, which are highly-ionized, are distributed in the central region, and consequently bremsstrahlung loss becomes large and excitation loss in the boundary region becomes extremely small (see Table 1. and Figs. 2-(b), 3, as the case of O and Fe, respectively).

Guiding parameters of INTOR give mean ionic charge of the plasma $Z_{\text{eff}} = 1.5$. However, calculated results show it is possible that in Case A, considerable amount of light impurities (e.g. 6 - 8 % of carbon) does not heavily deteriorate the hot core plasma. Although $Z_{\text{eff}} = 1.7 - 1.8$ in this case, most of impurity ions distribute in the cold region surrounding the hot core so that ion density $n_i \sim 0.9n_e$ in the hot core, and bremsstrahlung loss increases to 17 ~ 21 MW at most but excitation and ionization losses in the boundary region extremely increases to 29 ~ 45 MW. In such plasma most of energy losses carried by plasma particles from the hot core is converted into radiation in the boundary region and consequently edge temperature should be considerably low. Above results are derived from temperature-screening effect, i.e. strong inward diffusion of impurities is suppressed by temperature gradient of plasma ions. However when temperature-screening effect is neglected, strong edge-cooling by C impurity can not be expected even in Case A, as shown in Fig. 4. In this case, large minor radius of 1.4 - 1.5 m might be required to meet required τ_E for ignition.

Therefore, when we can except temperature-screening effect and high β value of 6 - 7 %, we can allow 5 - 10 % light impurity concentration and expect sufficient edge-cooling by light impurities without decrease of fusion power. In such plasmas, requirement for control will be extremely mitigated. However, these conclusions strongly depend on density and temperature distributions of the plasma, as well as impurity diffusion. Therefore, it is necessary to further investigations about the transport models for the plasma and impurities.

References

- 1) T. Tazima, Y. Nakamura, K. Inoue, Nucl. Fusion 17 (1977) 419 and
CORRIGENDA to this paper: Nucl. Fusion 17 (1978) 1393.
- 2) R.V. Jensen, D.E. Post, W.H. Grasherger, C.B. Tarter, W.A. Lokke,
Nucl. Fusion 17 (1977) 1187.
- 3) D.P. Cox, W.H. Tucker, Astrophys. J. 157 (1969) 1157.
- 4) R. Mewe, Astro. & Ap. 20 (1972a) 215.

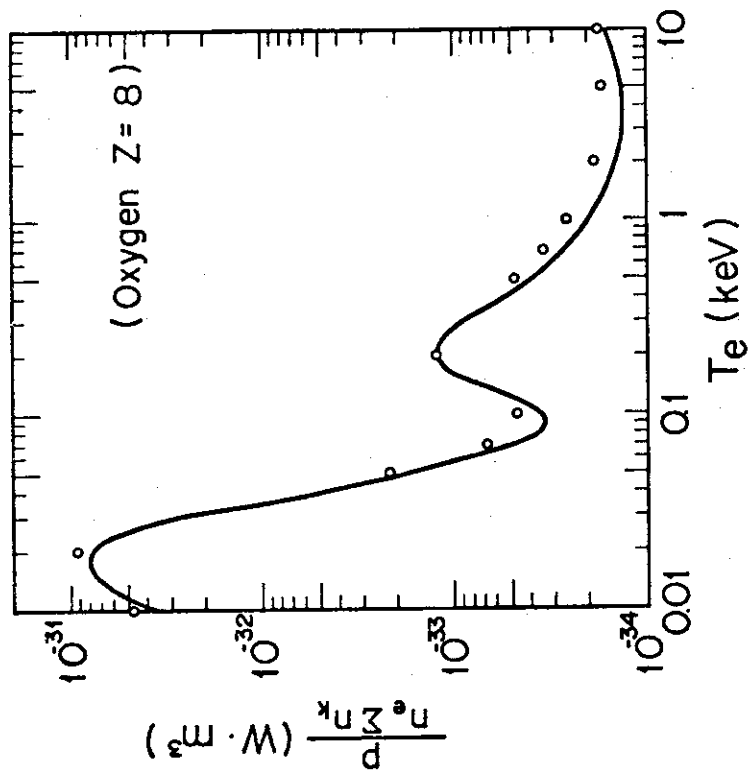


Fig. 1. Total radiation power as a function of electron temperature for oxygen. Solid lines are calculated by "average ion model" and circles are by ours where excitation loss P_{ex} is described as
$$P_{ex} = 1.73 \times 10^{-21} T_e^{-1/2} n_e \sum_{k=2}^{z+1} n_k \times \sum_{\lambda=1}^3 (8\pi/\sqrt{3}) f_{\lambda} \bar{g}_{\lambda}$$
 Most of known lines and oscillator strengths f_{λ} are considered and effective Gunt factors \bar{g}_{λ} is calculated by a formula given by Mewe.⁴⁾

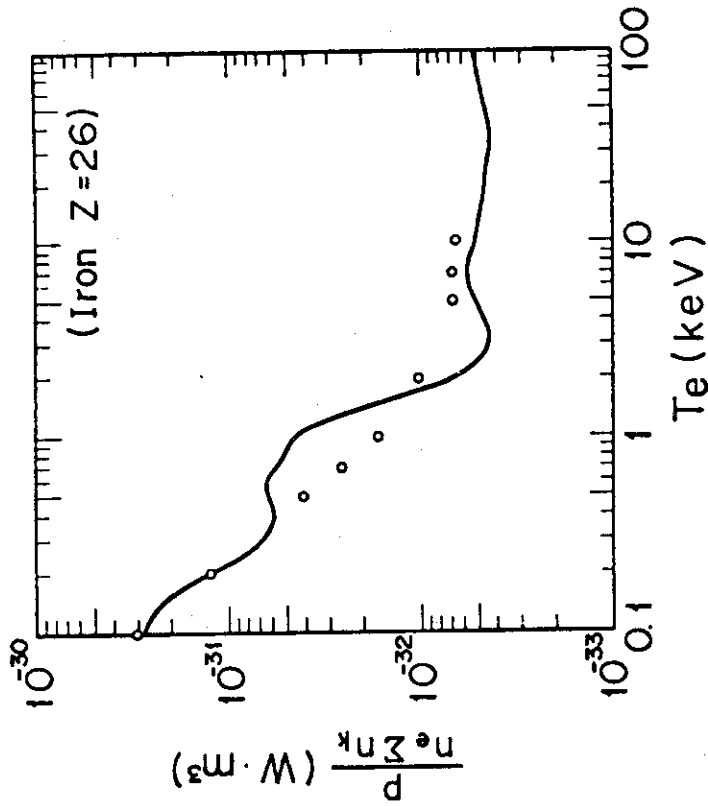


Fig. 2. Total radiation power as a function of electron temperature for iron. Otherwise, similar to Fig. 1.

Table 1. Energy losses caused by impurities from the given deuterium plasma, where C_z : impurity content, Z_{eff} : mean effective ionic charge, \bar{n}_e : mean electron density, P_{br} : total bremsstrahlung loss, P_{ex} : total excitation loss, P_i : total ionization loss. These losses are calculated in the circular plasma with 1.2 m minor radius, 5 m major radius and 242 m³ volume, and are multiplied by 1.5 to estimate those in the elongated plasma with 1.5 elongation ratio and 300 m³ volume.

Impurities	Carbon				Oxygen			Iron
	2	4	6	8	1	2	3	
C_z (%)	2	4	6	8	1	2	3	0.1
Z_{eff}	1.3	1.5	1.7 [2.2]	1.8	1.2 (1.4)#	1.4	1.6	(1.3)#
n_e ($\times 10^{20}/m^3$)	1.3	1.5	1.5 [1.6]	1.7	1.3 (1.3)#	1.3	1.4	(1.2)#
P_{br} (MW)	10.0	13.7	17.4 [29.7]	21.3	9.4 (11.1)#	11.7	14.1	(9.2)#
P_{ex} (MW)	4.2	10.9	20.2 [3.7]	31.8	13.0 (0.3)#	34.4	63.3	(3.7)#
P_i (MW)	2.4	5.4	9.0 [8.9]	13.3	2.5 (2.9)#	5.7	9.3	(7.0)#

Plasma parameters are;

ion density $n(r) = 2\bar{n}_i\{1-(r/r_p)^2\} + 5 \times 10^{18}$

electron and ion temperature $T_e(r) = T_i(r)$

Case A: $T_e(r) = 2.4\bar{T}\{1-(r/r_p)^4\}^{2.5}$ at $0 \leq r \leq 1.1$ m
 = 50 eV at $1.1 \leq r \leq 1.2$ m

Case B: $T_e(r) = 2\bar{T}\{1-(r/r_p)^2\}$ at $0 \leq r \leq 1.2$ m
 ()# = 50 eV at $r = 1.2$ m

where, $\bar{T}_e = \bar{T}_i = 10$ keV, $\bar{n}_i = 1.2 \times 10^{20} /m^3$. We assume that outward diffusion is anomalous (an anomalous factor of 10 for classical diffusion coefficient is employed) and inward diffusion is classical. The case without temperature-screening effect, i.e. where ion temperature gradient effect is neglected in the term of impurity inward diffusion, is also shown in this Table with a brace for 6 % carbon impurities of Case A.

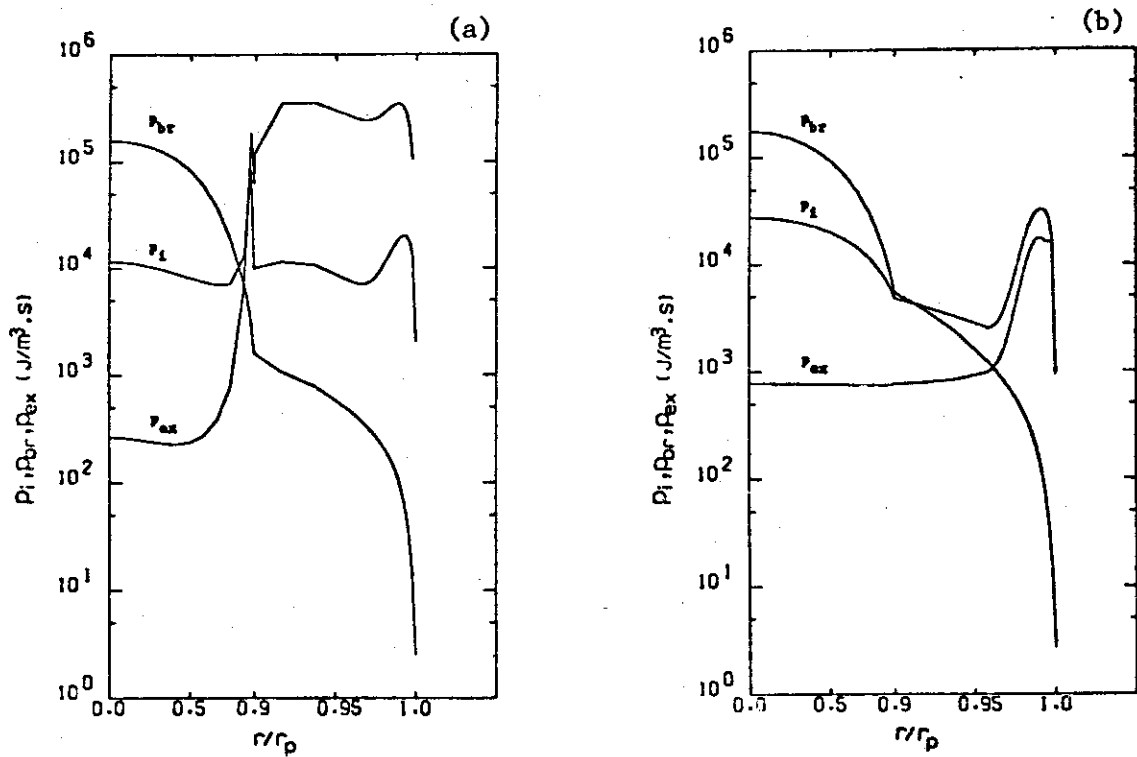
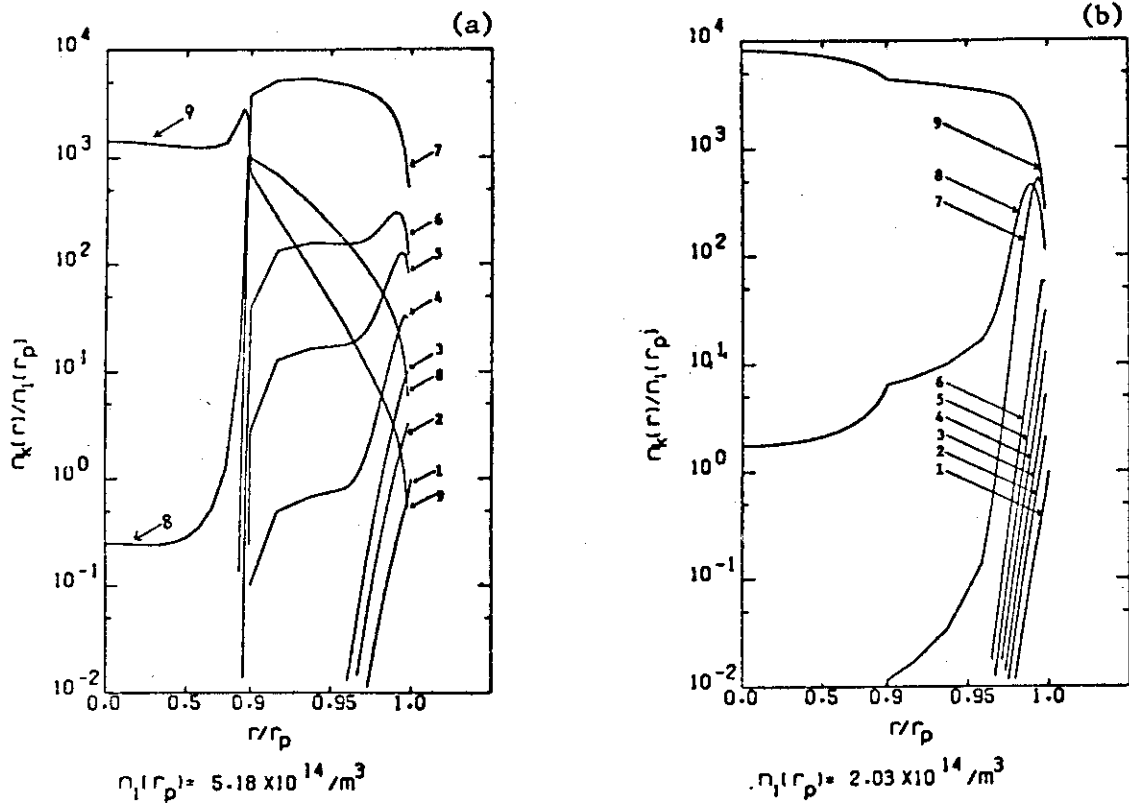
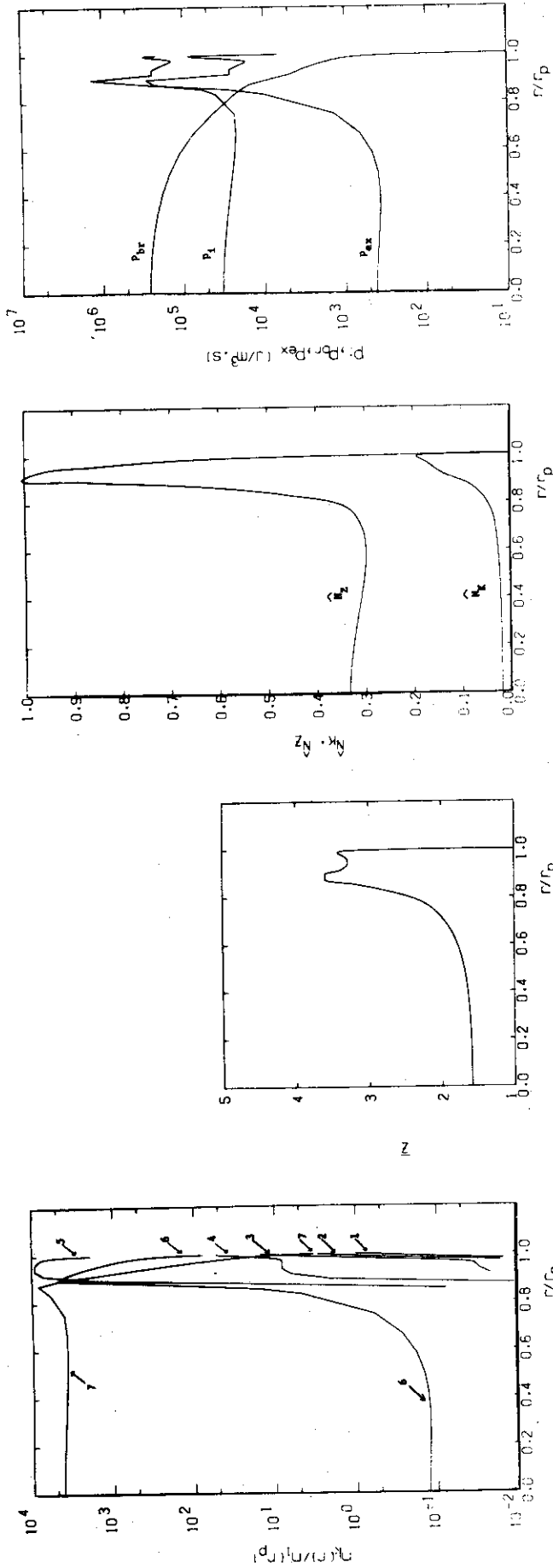


Fig. 3 Radial density distribution of 1% of oxygen impurities normalized by the boundary value of neutral oxygen density and related energy losses, in (a): Case A, and (b): Case B. Note that the scale of the normalized radius shown in the abscissa is changed at 0.9.



$n_i(r_p) = 1.26 \times 10^{15} / m^3$

Fig. 4-(a) Calculation for 6% carbon impurities of Case A with temperature-screening effect.

- 1): radial density distribution of carbon impurities normalized by the boundary value of neutral carbon density;
 - 2): mean effective ionic charge profile;
 - 3): normalized total impurity density profiles, $N_k = \sum_{k=2}^Z n_k(r)/n_e(r)$,
 - 4): radial distribution of related energy losses,
- $N_z = \sum_{k=2}^Z n_k(r) / \max_{k=2}^Z n_k(r)$
- P_{br} : bremsstrahlung loss, P_{ex} : excitation loss, P_i : ionization loss.

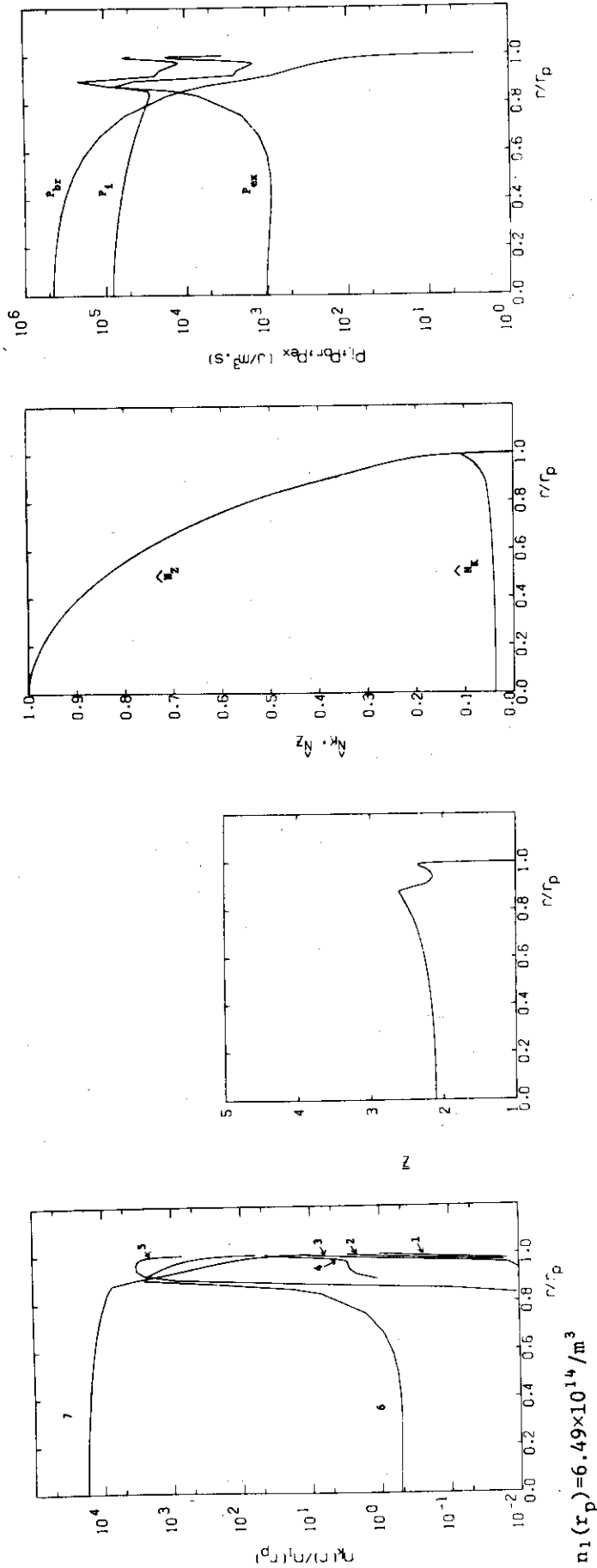


Fig.4-(b) Calculation for 6% carbon impurities of Case A without temperature-screening effect. Otherwise similar to Fig.4-(a).

3. EXPERIMENTAL RESULTS OF PLASMA-WALL INTERACTIONS

3.1 Impurity Production

1) Metallic impurity production¹⁾²⁾³⁾⁵⁾

It has been made clear what is the major mechanism of metallic impurity production.

Experimental results in DIVA (Figs. 1, 2) show that the self-sputtering of the metallic impurity ions accelerated by the sheath potential near the limiter surface is the major mechanism of metallic impurity recycling in ordinary discharges (Photo. 1). The evaporation of the limiter surface takes place by local deposition of high energy electrons in low density discharges (Photo. 2), and by arcing in an unstable discharge or in the case of a dirty limiter surface (Photo. 3). These studies were done by using the boundary scrape-off plasma of parameters $n_e = (1.5 \sim 5) \times 10^{12} \text{ cm}^{-3}$, $T_e = 20 - 100 \text{ eV}$ and $T_i = 20 - 80 \text{ eV}$. The limiters are electrically biased up to 500 V.¹⁾⁴⁾

A predominant mechanism for metal contamination in JFT-2 is the sputtering by highly ionized light impurities.⁵⁾ The relations among the metal impurity (mainly Mo), light impurity and the electron temperature of scrape-off plasma (T_{es}) are investigated by taking notice of dependences of the sputtering yields on incident ion species. The T_{es} is one of the important factors to determine the metal impurity as shown in Fig. 3. On the other hand, under the same T_{es} the metal concentration depends on the light impurity one that is mainly oxygen (Table 1). Working gas species are changed from H_2 to D_2 or He under the same T_{es} and concentration of light impurity. Table 2 shows that the sputtering by He ion, of which sputtering yield is greater than 10^2 of that for H_2 and D_2 , is the dominant source of Mo contamination. As is analogized from the He sputtering yield, the sputtering yield of oxygen ion may be roughly estimated at 10^{-1} and seems a reasonable value. Therefore, the Mo density can be explained as the sputtering by oxygen ion in the normal H and D plasma.

References

- 1) H. Maeda, S. Sengoku, K. Kimura, H. Ohtsuka, et al., Plasma Physics and Controlled Nuclear Fusion Research (Innsbruck, 1978) T-3-1.
- 2) K. Ohasa, H. Maeda, S. Yamamoto, M. Nagami, et al., Nuclear Fusion 18 (1978) 872.
- 3) K. Ohasa, S. Sengoku, H. Maeda, et al., JAERI-M 7935 (1978).
- 4) Y. Shimomura, Nuclear Fusion 17 (1977) 1377.
- 5) N. Suzuki, N. Fujisawa, S. Konoshima, M. Maeno, et al., Proc. 9th Europ. Conf. on Controlled Fusion and Plasma Physics (Culham 1979).

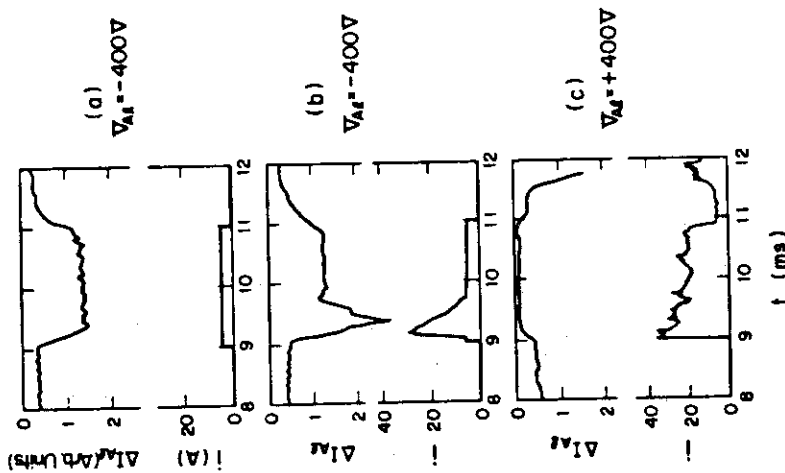


Fig. 1
 Typical time evolutions of Al III line radiation intensity (3620 Å) and the probe current. The target is biased from 9ms to 11ms. The applied voltage of the pulse is shown. (a) Ion sputtering; (b) arcing; (c) evaporation.

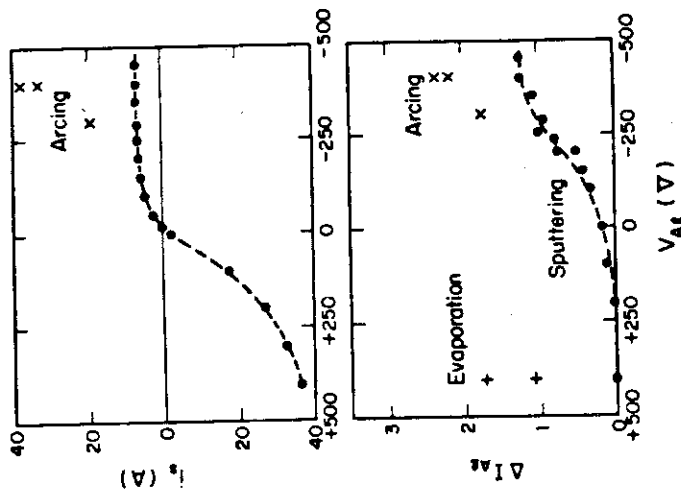


Fig. 2
 Probe current and Al III line radiation intensity versus voltage applied to Al target. The experimental results are classed clearly into three types. Full circles correspond to type(a) in Fig. 1 (ion sputtering), crosses to type(b) in Fig. 1 (arcing), and "+" points correspond to type(c) in Fig. 1 (evaporation).



Photo.1 Normal Discharge Plasma With Clean Surface: Self-Sputtering of Heavy Ion (Gold limiter or Aluminum limiter): Proton Sputtering (Carbon limiter): Sputtered corns observed on the gold protection plate exposed to about 100,000 discharges.

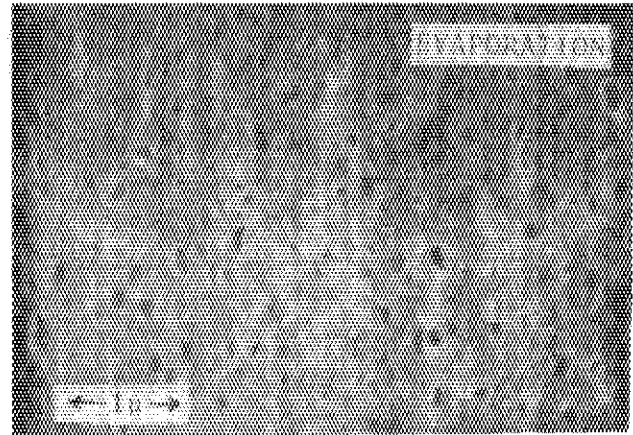


Photo.2 Abnormal Discharge Plasma: Runaway Discharge: Evaporation due to heat concentration: Scanning electron micrographs of the many melted spots on the electrically floated aluminum target in a divertor. These spots are created by high energy electrons from the main plasma

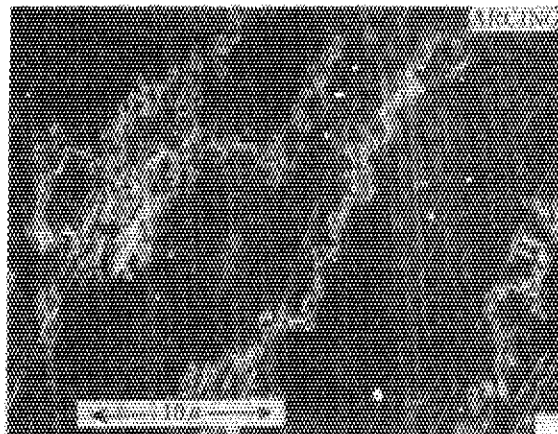


Photo.3 Disruptive Discharge or Normal Discharge with Dirty Surface Arcing: Scanning electron micrographs of arc tracks on the electrically floated aluminum target located in a divertor.

Table 1. Effect of light impurity (mainly Oxygen)

	V_1 (Volt)	OVI (cm^{-3})	OVIll (cm^{-3})	MoXIII (a.u.)	T_{es} (eV)	Z_{eff}	P_R (kW)
without Ti-getter	2.7	3×10^{10}	1×10^{12}	28	30	5.5	60
with Ti-getter	1.5	3×10^9	2×10^{11}	2.6	30	2.0	20

Table 2. Dependence on working gas species

Working gas	V_1 (Volt)	OVI (a.u.)	MoXIII (a.u.)	T_{es} (eV)	P_R (kW)	Sputtering yield (atoms/ion)
H ₂	1.2	2.3	~ 1.5	~ 12	12	$< 10^{-4}$
D ₂	1.2	2.5	~ 2.5	~ 13	15	$< 10^{-4}$
He	2.0	2.7	~ 22	~ 12	83	$< 10^{-2}$

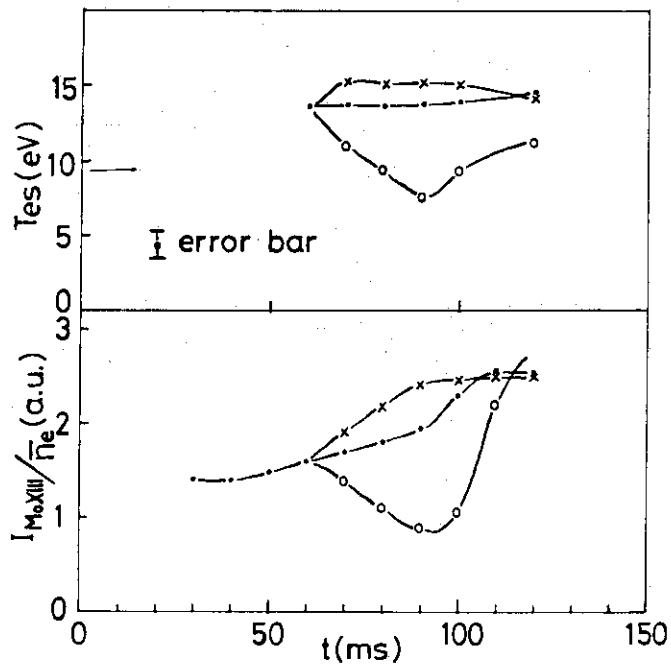


Fig. 3 The correlation between electron temperatures of the scrape-off layer and Mo line intensities in the plasma.

2) Experiments of low Z limiters in JFT-2¹⁾²⁾

Pyrolytic graphite (PG), silicon carbide (SiC), and Molybdenum (Mo) were used for the limiter in the JFT-2 tokamak and following experimental results were obtained.

(i) Comparison of the time behaviour of the CV and SiXII line radiances with that of the limiter surface temperature shows that the C and Si impurities in the plasma were not produced by evaporation due to surface temperature rise of the limiter.

(ii) Residual gas analysis during and after the discharge shows that the chemical reaction between the plasma and the C/SiC limiters was not a dominant mechanism for impurity generation from the limiter.

(iii) It has been hypothesized that physical sputtering by ions is one of the dominant mechanisms for impurity generation from the limiter.

Figure 1 shows the surface temperature rise on the four limiters in the typical period of the discharge. In all cases, the surface temperature increases continuously until $t = 100$ msec and then decreases slightly in the rest part of discharge. On the contrary, the time behaviours of the CV line radiance with the low-Z limiters and the SiXII one with the SiC limiter establish their plateaus near $t = 30$ msec as shown in Fig. 2. These two facts show that the C and Si impurities in the plasma were not generated by evaporation due to surface temperature rise of the limiter. Figure 3 shows the time behaviour of the CH_4 peak during and after the discharge with the four limiters. It has a peak at $t = 200 - 210$ msec which corresponds to the time at the end of discharge plus the delay time (50 ms) due to tubulation from the torus to the mass spectrometer. Comparison of the CH_4 peak value at $t = 200 - 210$ msec with the CV line radiance in the quasi-steady state of discharge (Fig. 4) indicates that methane formation on the limiter is not a dominant mechanism for carbon generation from the limiter.

If carbon is produced due to sputtering of the limiter by ions, the ratio of the total carbon ions N_c to the total protons N_p in the plasma is given by³⁾

$$\frac{N_c}{N_p} = \frac{\tau_c}{\tau_p} \frac{S_1}{1-R-S_s},$$

where τ_c is the mean particle confinement time of carbon ions, τ_p is the particle confinement time of protons, S_1 and S_s are the sputtering yields

of carbon by protons and self-sputtering yield, respectively, and R is the reflection coefficient of carbon ions. If we assume $\tau_c = \tau_p$, $N_e = N_p$, and $R + S_s = 0.5$ for rough estimation, $N_c/N_e = 0.01$ means $S_1 = 0.005$. The sputtering yield of this amount can be well realized in case of the PG limiters, since the physical sputtering yield of the same material by 100 eV protons is 2×10^{-3} to 1.5×10^{-2} ⁴⁾, and T_e in the limiter shadow region is 50 - 30 eV ⁵⁾. The protons bombarding the limiter should be about 100 eV due to acceleration by sheath potential ⁶⁾. The impurity ions other than carbon may assist to increase S_1 , since their mass is large and they are accelerated more by the sheath potential.

References

- 1) Y. Gomay, S. Konoshima, et al., Jpn. J. Applied Phys. 18 (1979) 1317.
- 2) T. Hirayama, N. Fujisawa, et al., J. Nuclear Materials, Vol.76, 1 & 2, (1978) 452-458.
- 3) Y. Gomay, T. Tazima, Japan Atomic Energy Research Institute Report, JAERI-M 6297 (1975).
- 4) K. Sone, H. Ohtsuka, et al., Proc. Int. Symp. on Plasma Wall Interaction, Julich, 1976 (Pergamon Press, 1977) 323.
- 5) Y. Gomay, N. Fujisawa, et al., Nuclear Fusion, 18 (1978) 849-857.
- 6) Y. Shimomura, Nuclear Fusion 17 (1977) 1377.

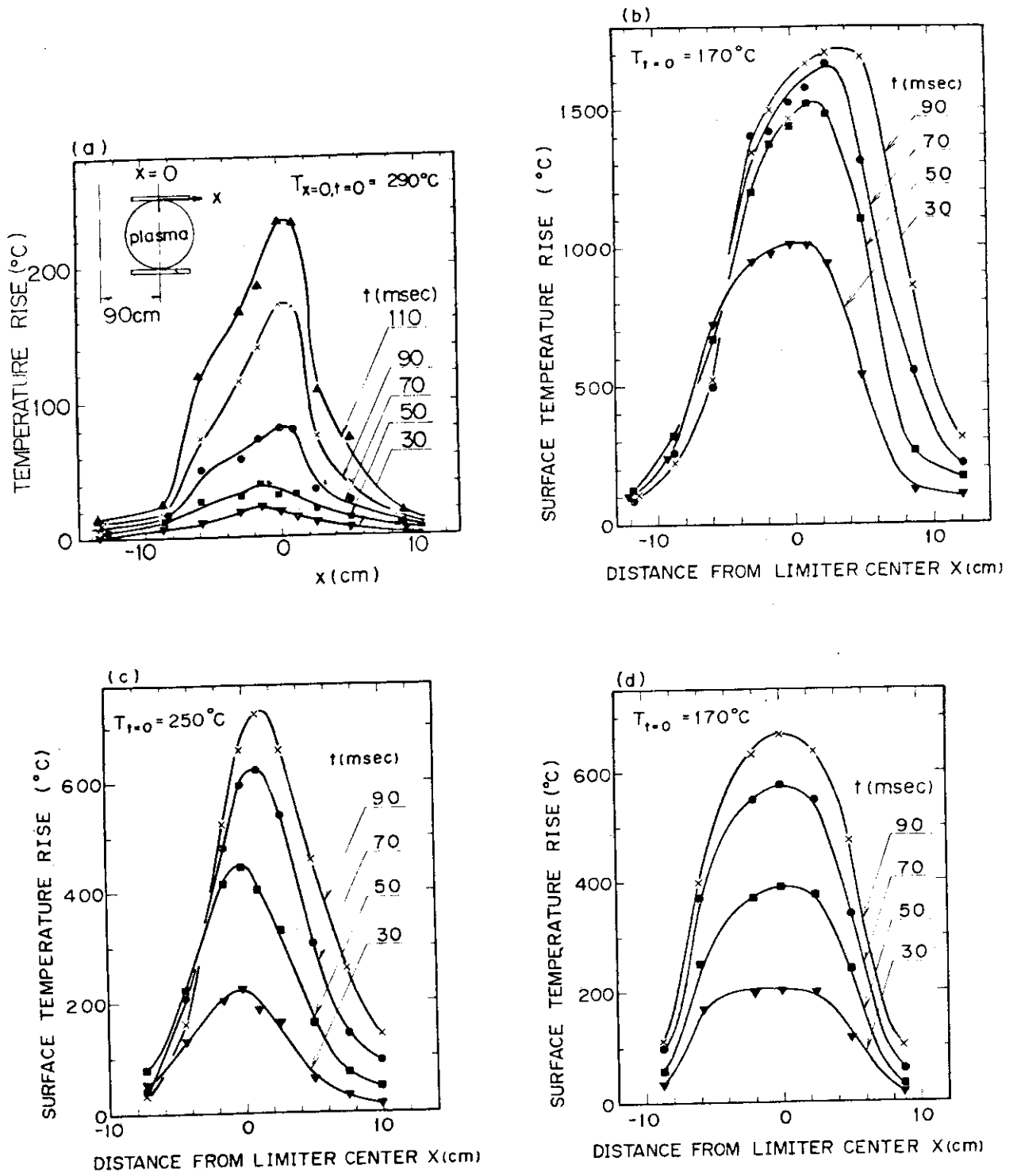


Fig. 1 Surface temperature rise every 20 msec in the typical period of the discharge on the (a) Mo, (b) PG//, (c) FGL, and (d) SiC limiters.

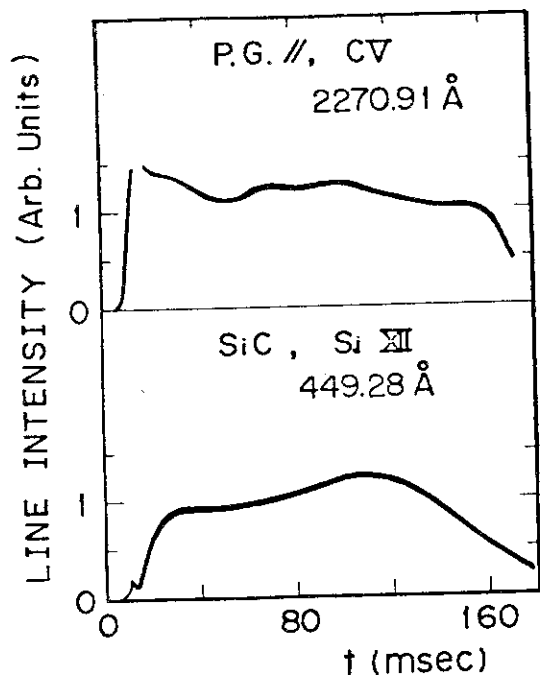


Fig.2 Time behaviour of CV line radiance horizontally observed at Z=12 cm in the discharge with the PG// limiter and the SiXII radiance observed at Z=0 with the SiC limiter.

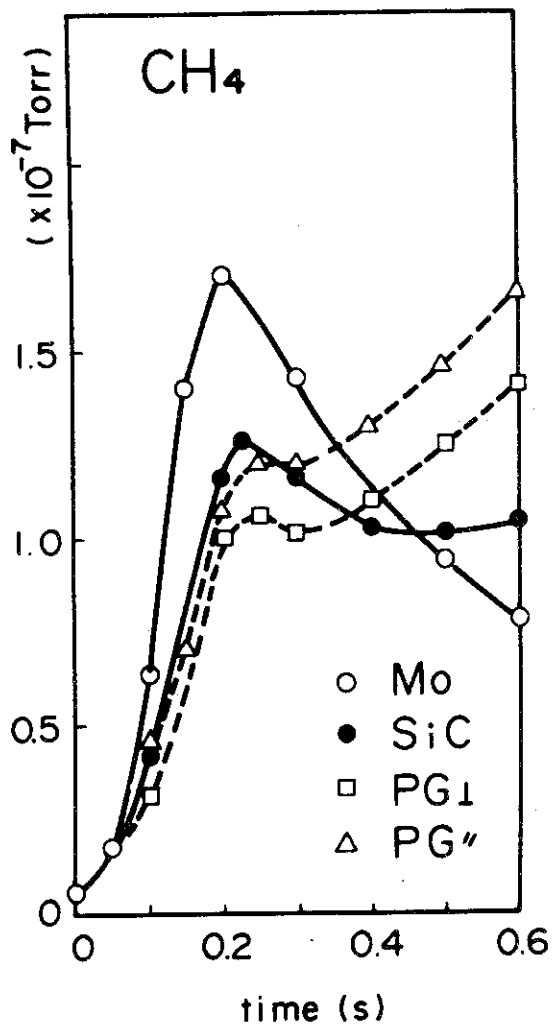


Fig.3 Comparison of methane partial pressure vs. time for limiter materials.

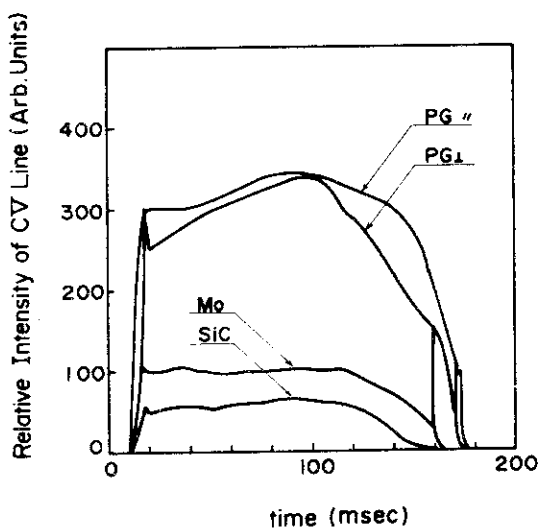


Fig. 4 Comparison of CV line intensity vs. time for limiter materials.

3) Experiments of low Z materials in DIVA¹⁾

Pyrolytic graphite (P.G.), carbon films produced by methane discharges and pre-coated carbon layer by rf sputtering device in pre-coating chamber with low initial vacuum of 2×10^{-5} Torr, were tested as limiter surfaces in a tokamak.⁽²⁾ Plasma with the P.G. limiter and the carbon wall in-situ coated by two sets of rf sputtering device in high initial vacuum of 2×10^{-7} Torr was also investigated.

(1) Figures 1, 2 and 3 are SEM pictures of three kinds of the carbon. The carbon produced by rf sputtering has the form similar to powder. The carbon produced by methane discharges is rather similar to the P.G. surface. In the methane discharges, the carbon ions which flow onto the surface have energy of about 100 eV because they are accelerated by the sheath potential. Thickness of a few Å on the limiter surface is obtained by one discharge. The discharge current is 20 kA, the duration is 30 ms and the filling methane pressure is 1×10^{-4} Torr.

The standard method to investigate sputtering and arcing on a surface contacting to a plasma is used²⁾. A part of the limiter is biased. The current to the limiter and the intensity of CII line radiation near the limiter are observed. The emitted carbon from the limiter is ionized within 100 μsec. Therefore the intensity of CII line is proportional to the efflux from the limiter surface. Figure 4 shows the results. Arcing is frequently observed on the carbon surface produced by rf sputtering, e.g. the probability of arcing is 17 % with 400 V of applied voltage. This situation simulates the surface which contacts to the plasma with $T_e \sim 200$ eV. Arcing is observed only in disruptive discharges on the P.G. surface and the carbon film produced by methane discharges. This result is very similar to those of metal surfaces¹⁾. Figure 5 shows ΔI_{CII} v.s. V wher ΔI_{CII} is increment of CII line intensity and V is bias voltage. This figure shows the efflux of C is due to the proton sputtering. Therefore the ion sputtering is the dominant process of the carbon impurity origin.

The next problem is a chemical sputtering at a high temperature regime. The part of the limiter is heated up to 750 °C and the standard method is employed to measure the relative sputtering yield. Figure 6 shows sputtering yield is enhanced by the chemical sputtering with $T_{limiter} \geq 250$ °C. However, the enhancement by the chemical sputtering can not be observed on the surface which was bombarded by protons at a

high temperature (Fig. 7(a), (b)). Therefore the chemical sputtering is easily suppressed. A similar result is also obtained by T. Abe et al.³⁾

(2) The first wall is in-situ coated with carbon. The AES picture is shown in Fig. 8, which shows the surface is pure. The spectrum does not change during 500 normal discharges after 50 cleaning discharges. This kind of carbon covers 70 % of the first wall. The plasmas have a good confinement time as shown in Fig. 9. And a $q_a < 2$ discharge with the good confinement time is also stably obtained. Figure 10 shows typical temperature and radiation loss profiles with Ti wall and with C wall, are shown.

References

- 1) DIVA Group, to be published.
- 2) K. Ohasa, et al., Nuclear Fusion 18 (1978) 872, J. Nuclear Material 76 & 77 (1978) 487, J. Phys. Soc. Japan 46 (1979) 1635, JAERI-M 7935.
- 3) T. Abe, et al., "Interaction of Atomic Hydrogen with Carbon" submitted to J. Nucl. Material.
- 4) J.N. Smith, Jr., C.H. Meyer, Jr. and J.K. Layton, J. Nucl. Material 67 (1977) 234.



Fig. 1 Scanning electron micrograph (SEM) picture of pyrolytic graphite surface.

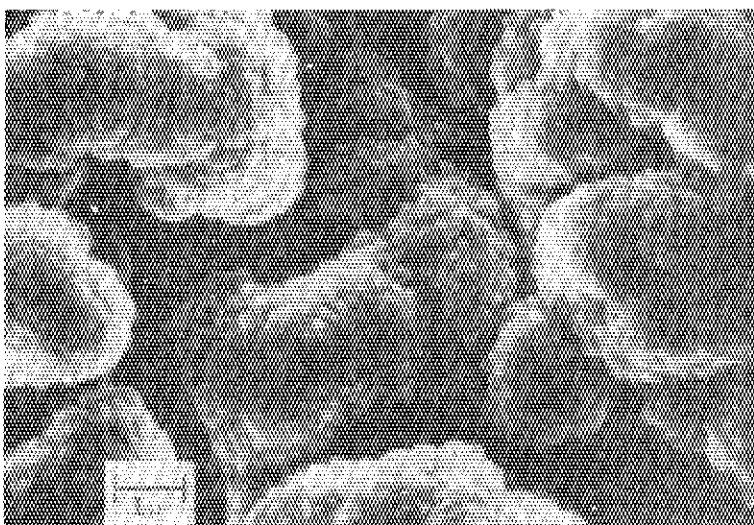


Fig. 2 SEM picture of carbon surface produced by rf sputtering method

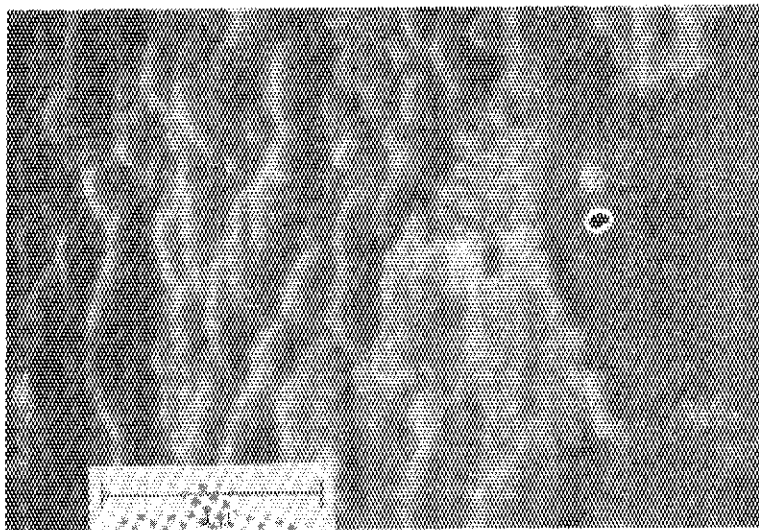


Fig. 3 SEM picture of carbon surface produced by methane discharges

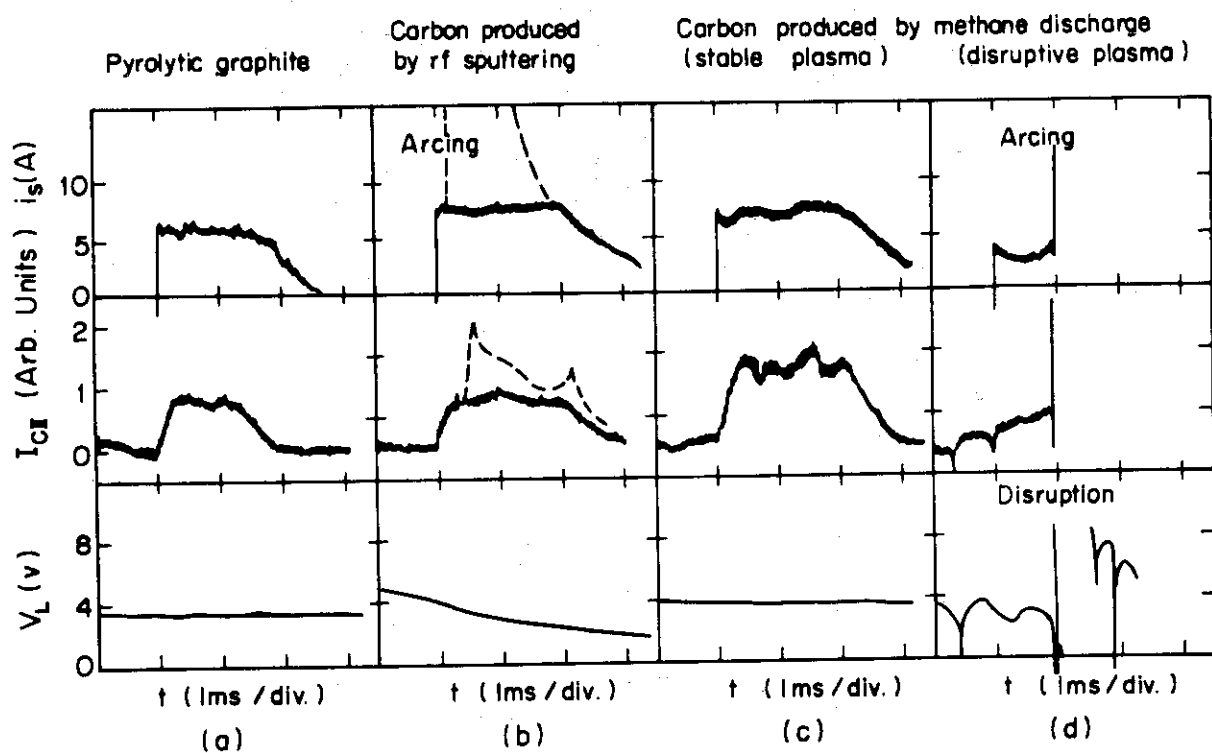


Fig. 4 Typical wave forms of ion saturation currents i_s of a part of the limiter, increment of CII line intensity ΔI_{CII} and loop voltage V_L

- (a) Pyrolytic graphite
- (b) Carbon surface pre-coated by rf sputtering method. Arcing is observed.
- (c) Carbon surface produced by methane discharges.
- (d) Carbon surface produced by methane discharges in a disruptive discharge. Arcing is observed.

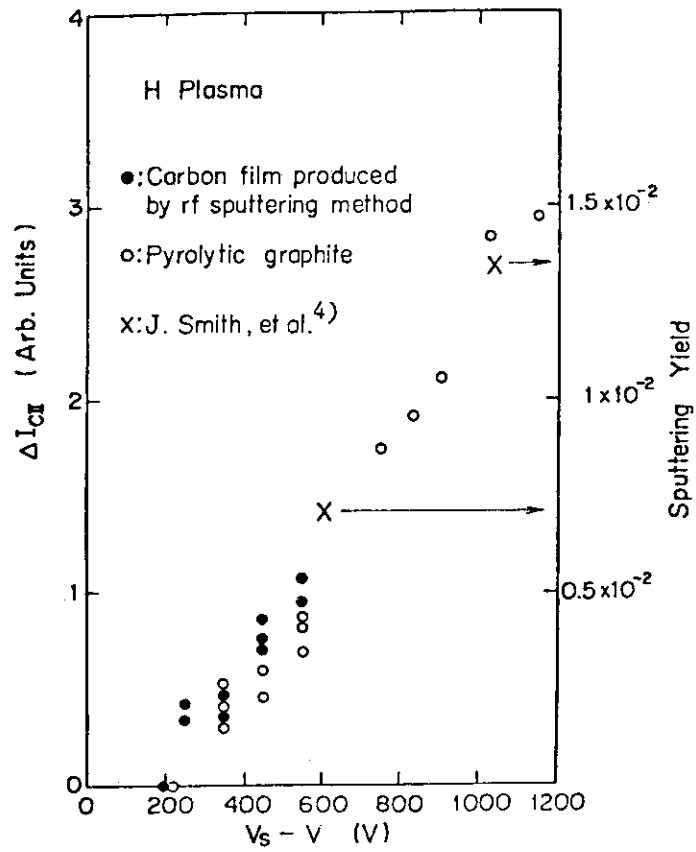


Fig. 5 ΔI_{CII} v.s. V where ΔI_{CII} is increment of CII line intensity and V is bias voltage.

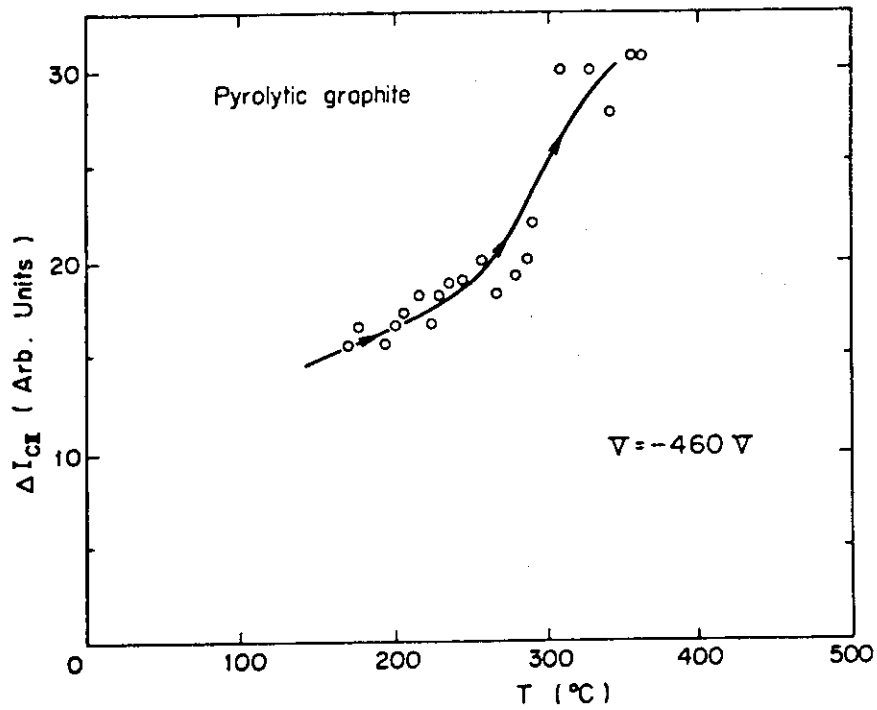


Fig. 6 ΔI_{CII} v.s. T where ΔI_{CII} is increment of CII line intensity and T is temperature of a limiter surface.

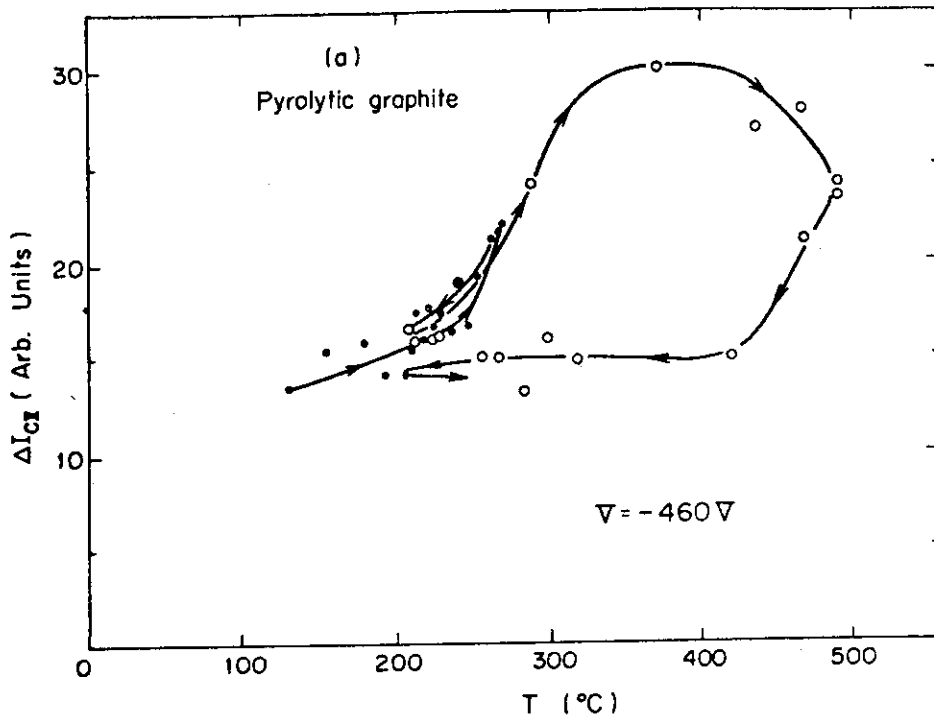


Fig.7-(a)

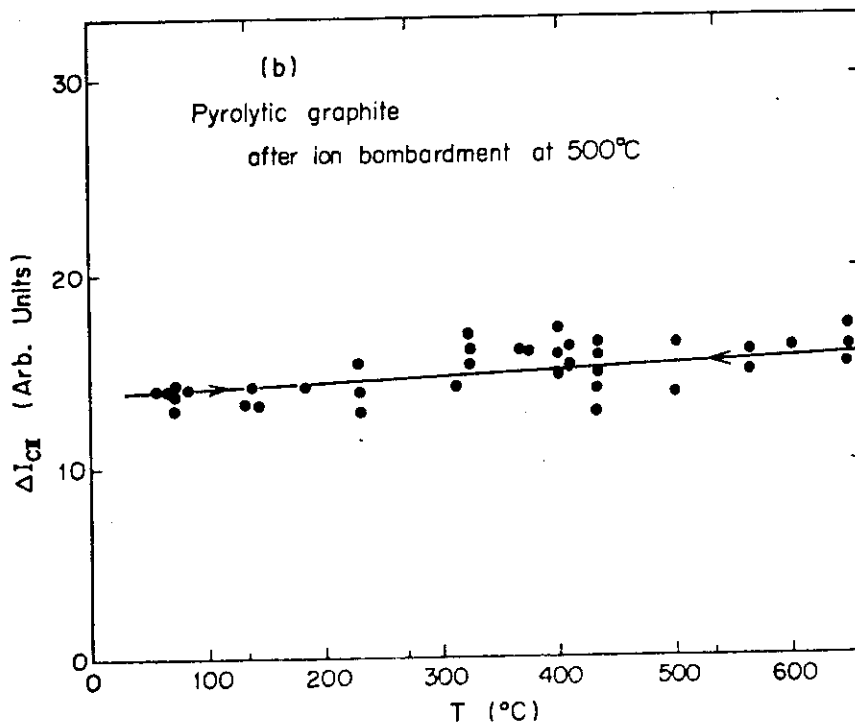


Fig.7-(b)

Fig. 7 ΔI_{CII} v.s. T. Suppression of chemical sputtering is observed after (a) one heat cycle; (b) a few heat cycles, with ion bombardments.

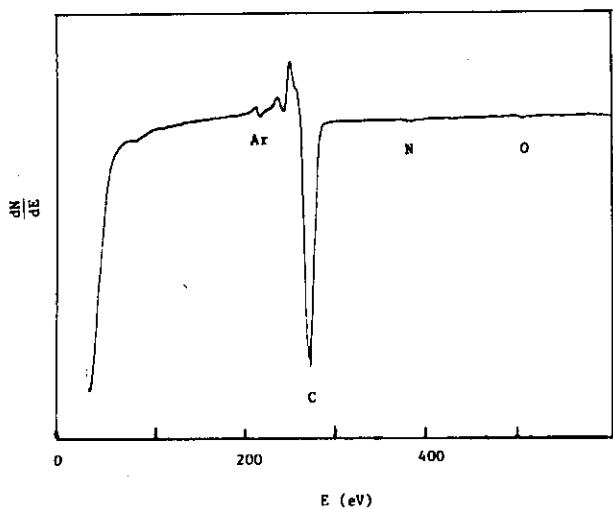


Fig. 8 AES of carbon film coated on the first wall in DIVA. The spectrum does not change during 500 discharges after 50 cleaning discharges.

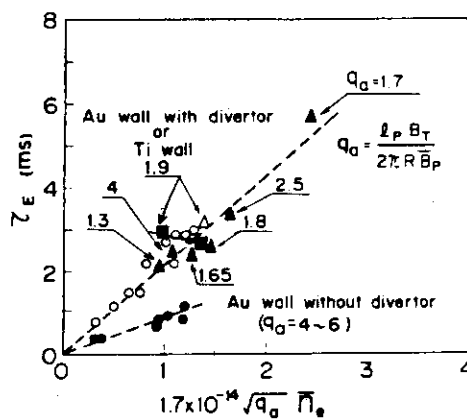


Fig. 9 Energy confinement time v.s. $q_a^{1/2} \bar{n}_e$ where \bar{n}_e is mean electron density in cm^{-3} .
 ○ ● : Au; △ ▲ : Ti;
 ■ : Carbon

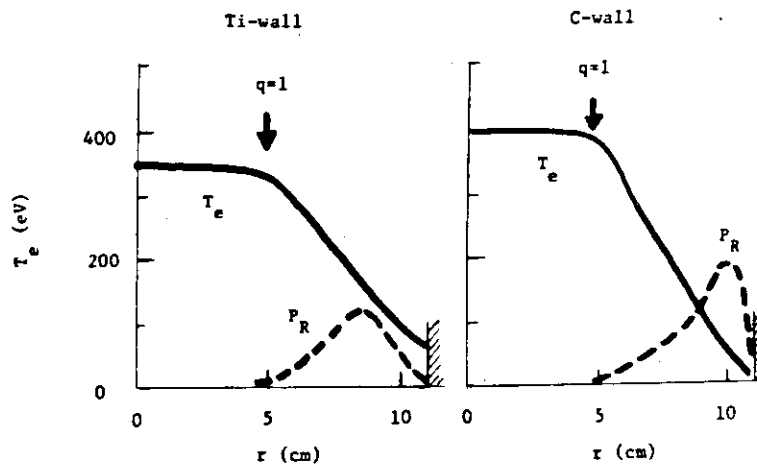


Fig. 10 Very low q discharges with C-wall and Ti-wall at $q_a \sim 1.9$.
 $n_{e0} = 7 \times 10^{13} \text{ cm}^{-3}$, $\tau_E = 3.2 \text{ ms}$, radiation loss $P_R \sim (15-20)\%$ of input power and $Z_{eff} \leq 1.5$ with Ti-wall. $n_{e0} = 5 \times 10^{13} \text{ cm}^{-3}$, $\tau_E = 2.8 \text{ ms}$, $P_R \sim 30\%$ and $Z_{eff} \leq 2.0$ with carbon wall.

3.2 Recycling of Plasma Particles

Recycling ratio $\gamma^{1)}$ is estimated as ~ 0.9 , in normal operation of the JET-2 device with a stainless steel wall and a molybdenum limiter. Flashing titanium onto the half torus wall surface, the ratio γ is reduced to 0.7. In order to estimate the experimental recycling ratio, the particle balance is studied with a simple model such as

$$\frac{dN_e}{dt} = -(1 - \gamma) \frac{N_e}{\tau_p} + \alpha \cdot Q$$

N_e : total number of electrons,

Q : influx of hydrogen atoms through a control puff,

α : effective ionization rate,

τ_p : particle confinement time.

The electron density increases linearly with time through the constant gas feeding by control puff and decreases monotonously after an end of the feeding, as shown in Fig. 1. Figure 1 is represented by Fig. 2 with dN_e/dt , as the ordinate and Q , as the abscissa.

Figure 2 shows that gradients of dN_e/dt are constant in a build up phase and dN_e/dt is constant in a decreasing phase of the density. Therefore, we can conclude that α , γ , and τ_p/N_e are constant during a discharge, and independent of the electron density. Then, we can estimate the recycling ratio as follows,

	Limiter	Ti flash (20 mg/shot)	
A	B ₄ ϕ 390	without Ti	0.93
B	B ₂ ϕ 400	without Ti	0.91
C	B ₄ ϕ 390	with Ti	0.75
D	B ₂ ϕ 400	with Ti	0.68

where a pair of movable rail - limiters of 40 cm distance is used at the observation box B₂, and the other pair of movable rail - limiters (39 cm distance) is placed at the B₄ box opposite the B₂ box along the torus direction. JET-2 tokamak plasmas have been simulated by a one dimensional transport code.²⁾³⁾ The recycling ratio γ of the plasma particles is estimated to explain the evolution of the electron density with gas puffing. In the code the particle flux is represented as (influx of neutrals) = $\gamma \cdot$ (outflux of ions and neutrals) + (puffing gas flux), where the puffing

gas flux is measured experimentally by a fast manometer. Simulation results are in good agreement with experimental ones when γ is 0.9, as shown in Fig. 3.

References

- 1) N. Suzuki, private communication and JAERI-M 7479 (1978) 27.
- 2) T. Hirayama, private communication and JAERI-M 7479 (1978) 30.
- 3) T. Tazima, JAERI-M 7717 (1978).

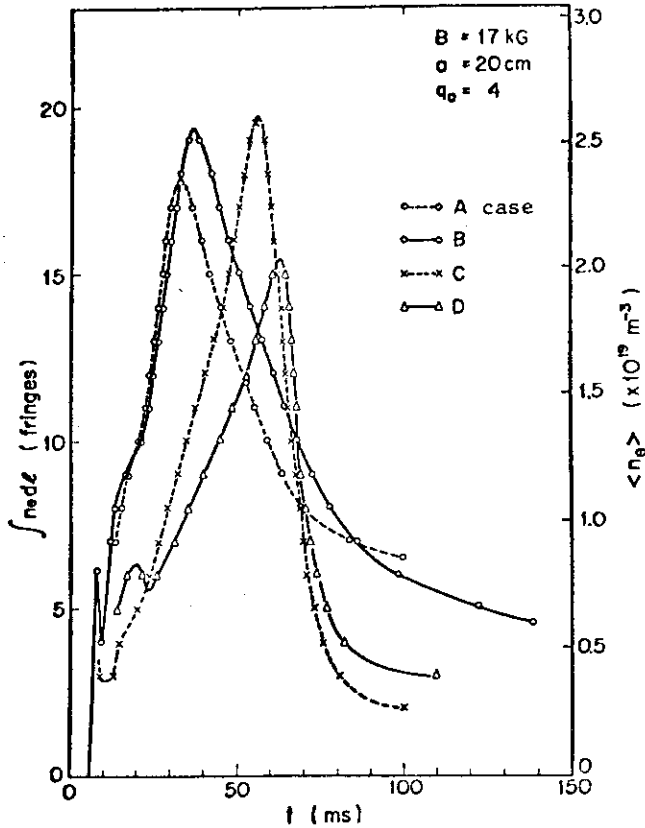


Fig. 1 Temporal behaviours of electron densities corresponding to various amounts of gas puffing, where cases A & B : without Ti coating; case C: with Ti coating onto the wall(1/2); case D: with Ti coating onto the wall and the limiter.

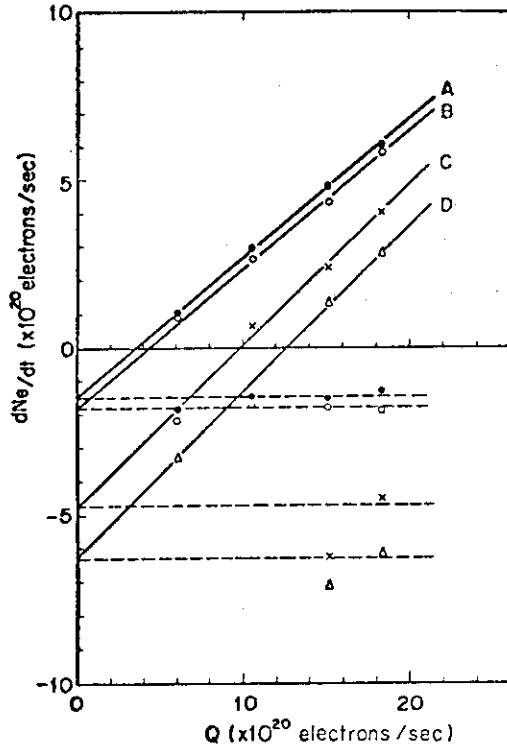


Fig. 2 Gradients of dN_e/dt in build up and decreasing phases of the electron densities.

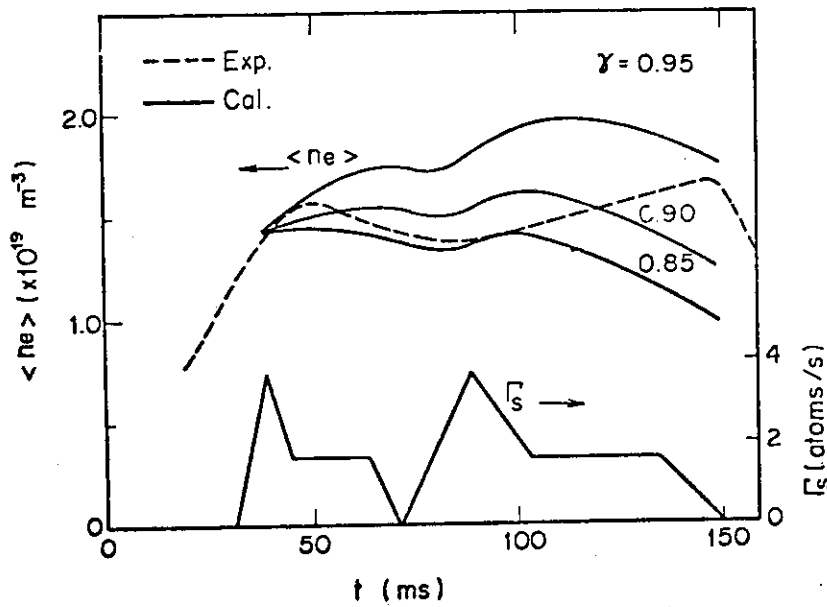


Fig. 3. Simulation results of the electron density evolution on the recycling ratios, 0.85, 0.9 and 0.95 with gas puffing. Time evolutions of line averaged electron densities during gas puffing in the JFT-2 plasma are simulated by one-dimensional tokamak code, where Γ_s is supplied particle flux and γ is the recycling ratio.

4. SPECIFIC MEANS FOR DECREASING PLASMA CONTAMINATION

4.1 Wall Conditioning to Reduce Sorbed Impurities

The methods to obtain a clean surface of a vacuum chamber are, Before assembly, surface treatment to remove absorbed impurities and oxide layer;

- { glow discharge cleaning
- { buffpolishing
- { electropolishing

After assembly, wall conditioning to remove adsorbed impurities;

- { baking
- { chemical treatment by gases
- { discharge cleaning
- { in-situ coating.

1) Surface treatment before assembly¹⁾²⁾

Before assembly, thick layers of several thousand angstroms on the first wall contaminated by oxidation and machining should be removed such by glow discharge cleaning, buffpolishing, and electropolishing, since such thick layers can not be removed by in-situ cleaning after assembly. Figures 1 and 2 show the effectiveness of these treatments and after once cleaning by such treatments the surface is contaminated no more than 200 Å in the depth, even when it is exposed to air for a month, as shown in Fig. 3.

2) Wall conditioning after assembly

(1) Baking

In order to attain a high vacuum, baking is necessary not only for the first wall but for surfaces not facing the plasma which can not be cleaned by in-situ method except baking. Following figures show the effect of baking on ontgassing rates of the wall materials such as;²⁾³⁾⁴⁾¹⁰⁾

304 stainless steel	Fig. 4	} Table 2
YUS - 170	Fig. 5	
Inconel 625	Fig. 6	
Hastelloy X	Fig. 7	
Molybdenum	Fig. 8	
Carbon and Silicon Carbide	Figs. 9, 10	

The outgassing rates of metallic materials are decreased to less than several $\times 10^{-13}$ Torr \cdot l/s \cdot cm² at room temperatures after baking for 100 - 200 hrs at 500 °C. Generally, the outgassing rates of fine grained graphite, silicon carbide coated on to molded graphite by chemical vapour deposition and molded graphite are several ten times as much as that of 304L stainless steel, while pyrolytic graphite is a potential material of low outgassing rate as much as the tested metallic materials.

(2) Chemical treatment by exposing the material to oxygen and hydrogen gases¹⁾²⁾³⁾⁴⁾

A necessary temperature for reducing oxides by hydrogen gas is more than 1000 °C for niobium, tungsten and tantalum which are potential materials for the first wall of future large tokamaks, while it is 500 °C for molybdenum⁵⁾. It is concluded that carbon and oxygen on the molybdenum surface can be reduced to 1/4 of the initial contamination by successive exposing to 0.1 Torr oxygen and 1 Torr hydrogen gases at 500 °C, while this treatment is effective within a few hundred angstroms in the depth (see Fig. 11). This is a simple method if the molybdenum first wall can be baked up to 500 °C, since this treatment requires only 10 ~ 20 hrs, but this effect is more powerful than high power discharge cleaning⁷⁾ by a factor of two.

(3) Discharge cleaning

Recently it has been shown that the discharge cleaning by a weekly-ionized hydrogen plasma with a low plasma current and a low plasma temperature is more powerful than the conventional discharge cleaning with high current⁶⁾. Table 3 shows the results of Low power Discharge Cleaning (LDC) and High current Discharge Cleaning (HDC) experiments in the JFT-2 tokamak⁷⁾. LDC can clean the first wall faster than HDC by a factor of ten. After LDC a plasma does not take a turn for the worse during about ten shots, though the surface is contaminated shot by shot as shown in Fig. 12.

The mechanism of LDC is supposed that water molecules are formed on the wall surfaces by chemical reaction of the adsorbed oxygen or the oxidized layer and protons or radical atomic hydrogens. After particle-induced desorption and/or thermal desorption, these molecules are evacuated through the vacuum system. Therefore, it is most important

that the molecules should not be dissociated and/or ionized in the plasma. Optimum plasma temperature in LDC should be in a region such as,

$$\begin{aligned} &[\text{Dissociation energy of H}_2] < T_e < [\text{Dissociation energy of H}_2\text{O}] \\ &\text{i.e.,} \quad 4.5 \text{ eV} < T_e < 9.6 \text{ eV.} \end{aligned}$$

The results shown in Fig. 13 support well the above condition.

(4) In-situ coating

Titanium coating onto the torus wall is regarded as a most powerful method to obtain plasmas free from the gaseous impurities. In JFT-2⁸⁾ and DIVA⁹⁾, oxygen impurities have been reduced down to 1 - 2 % of the electron density by titanium gettering onto the torus wall and the limiter, then radiation loss and effective ionic charge were decreased by a factor of about two, as shown in Table 4. As a result of reduced impurity influx, broader electron temperature profiles have been obtained, as shown in Fig. 14. The energy confinement time and the scaling factor of the plasma density (Fig. 15) were improved by a factor of 1.6. Moreover, low q discharges can be easily operated¹¹⁾.

References

- 1) Y. Gomay, T. Tazima, et al, JAERI-M 7405 (1977).
- 2) T. Tazima, JAERI-M 7717 (1978).
- 3) T. Tazima, Y. Gomay, Proc. Int. Symp. Plasma Wall Interaction, Culham, (1976) 559-571.
- 4) T. Tazima, The third Int. Conf. Plasma Surface Interactions in Controlled Fusion Devices, Culham, (1978); J. Nuclear Materials, 76 & 77 (1978) 594-599.
- 5) J.M. Mellow, A Comprehensive Treatise on Inorganic and Theoretical Chemistry, Longmans, Green and Co., London, XI, (1954) 540.
- 6) L. Oren, R.J. Taylor, Nuclear Fusion 17 (1977) 1143.
- 7) Y. Gomay, T. Tazima, N. Fujisawa, J. Vac. Sci. Tech. 15 (1978) 103.
- 8) S. Konoshima, N. Fujisawa, et al., The third Int. Conf. Plasma Surface Interactions in Controlled Fusion Devices, Culham, (1978); J. Nuclear Material, 76 & 77 (1978) 581-586.
- 9) H. Maeda, S. Sengoku, et al., 7th Int. Conf. on Plasma Physics and Cont. Nuclear Fusion Research, Innsbruck, (1978) T-3-1.

- 10) H. Yoshikawa, et al., Proc. 7th Int. Vac. Congr. & 3rd Int. Conf. Solid Surfaces (Vienna, 1977) 367.
- 11) DIVA Group, JAERI-M 8205 (1979).

SAMPLE	IMPURITY CONTENT (P.P.m.)			REFINING METHOD	MANUFACTURER
	CARBON	OXYGEN	NITROGEN		
A	35	70	20	P.M. #	SYLVANIA
B	30	3	2	A.M. #	AMAX
C	1300	40		A.M. ##	TOSHIBA
D	170	5		A.M. ##	TOSHIBA
E	15	17		E.B.M. ###	TOSHIBA
F	10	0.5	2	E.B.M.	DAIDO

Powder Metallurgy
 ## Arc Melt
 ### Electron Beam Melt

Table 1 Process and impurity contents in sample materials.

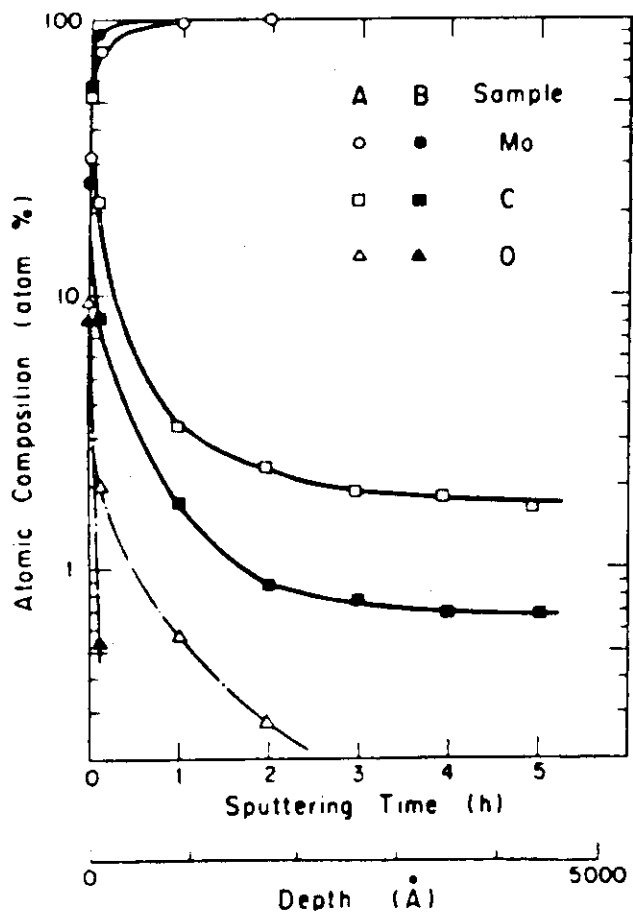


Fig. 1 Depth profiles of surface compositions in buff-polished samples.

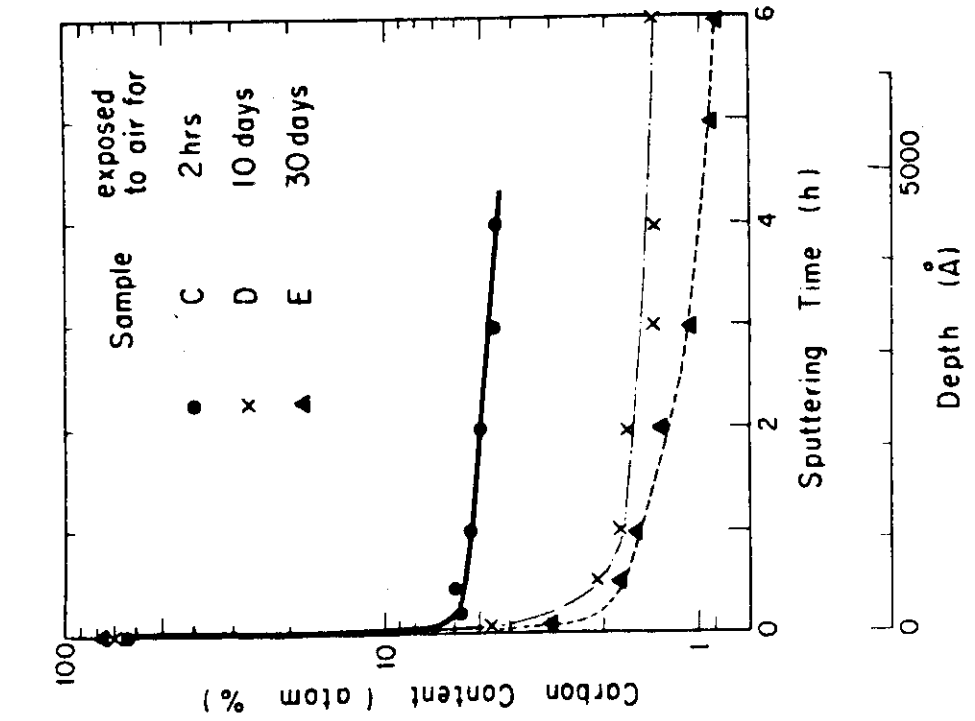


Fig. 3 Depth profiles of surface compositions in the respective samples exposed to air for 2 hours, 10 days and 30 days after cleaning by a ion etching.

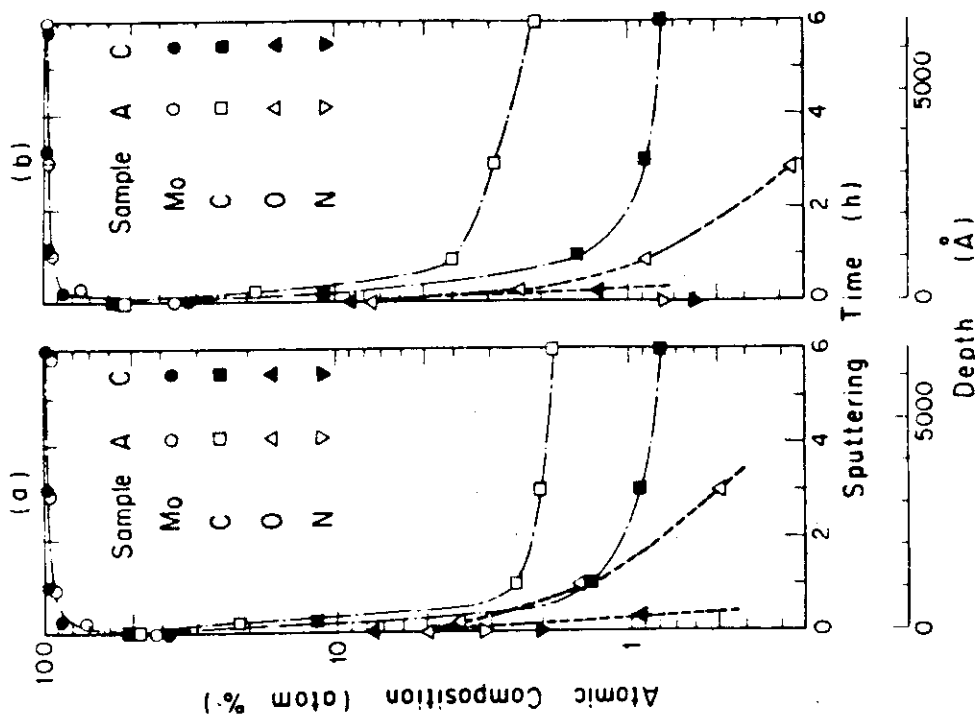


Fig. 2 Depth profiles of surface compositions. Left: exposed to air for 1 hour after glow discharge cleaning. Right: exposed to air for 2 days after electropolishing.

Table 2 Outgassing rates of SS-304L, YUS-170, Inconel-625, Hastelloy-X, Molybdenum, Pyrolytic graphite and SiC coated onto graphite. [Pa.l.s⁻¹.cm⁻²]

	Before bake-out						During bake-out						After bake-out					
	Time from starting pumping (hour)						Time after the temperature reaches 500°C (hour)						Time after the heater is turned off (hour)					
	1	5	10	20	50	20	1	5	10	50	20	1	5	10	20			
Stainless steel SS-304L	Total	2.9E-6*4	5.3E-7	2.7E-7	1.3E-7	1.3E-7	3.5E-5	7.6E-6	4.0E-6	2.3E-7	9.0E-9	2.5E-9	1.3E-9	6.7E-10	6.7E-10			
	m/e= 2(H ₂)	1.9E-7	5.6E-8	2.9E-8	1.7E-8	1.7E-8	2.5E-5	6.5E-6	2.7E-6	1.9E-7	8.5E-9	2.0E-9	9.3E-10	-	-			
	18(H ₂ O)	1.5E-6	2.4E-7	1.3E-7	7.8E-8	3.9E-7	3.9E-7	-	-	-	1.7E-10	-	-	-	-			
	28(CO)	1.5E-7	3.6E-8	1.5E-8	1.1E-8	8.2E-6	8.2E-6	7.3E-7	2.3E-7	3.9E-8	1.5E-10	3.4E-11	-	-	-			
Stainless steel YUS-170	Total	5.2E-7	3.1E-8	1.3E-8	4.1E-9	3.7E-7	3.7E-7	1.1E-7	5.7E-8	1.7E-8	3.4E-9*2	(4.0E-10)	(2.0E-10)	(8.8E-11)	-			
	m/e= 2(H ₂)	8.4E-8	3.2E-9	1.6E-9	3.8E-10	5.7E-8	5.7E-8	2.5E-8	2.3E-8	4.3E-9	3.1E-9*2	-	-	-	-			
	18(H ₂ O)	1.7E-8	1.3E-8	2.3E-9	2.0E-9	1.0E-8	1.0E-8	1.3E-9	-	-	-	-	-	-	-			
	28(CO)	2.7E-8	2.9E-9	1.3E-9	5.6E-10	2.3E-7	4.9E-8	2.7E-8	4.9E-9	4.9E-9	1.3E-11*2	-	-	-	-			
Inconel-625	Total	9.3E-6	1.3E-6	6.4E-7	2.6E-7	2.6E-7	-	-	5.2E-6	2.4E-7	3.3E-10	1.4E-10	1.1E-10	7.3E-11	-			
	m/e= 2(H ₂)	9.0E-7	1.7E-7	1.2E-7	9.0E-8	9.0E-8	-	-	4.1E-6	5.7E-8	1.7E-10	6.7E-11	6.9E-11	5.3E-11	-			
	18(H ₂ O)	2.1E-6	4.5E-7	2.2E-7	1.6E-7	1.6E-7	-	-	-	-	6.0E-12	4.1E-12	3.4E-12	2.9E-12	-			
	28(CO)	7.7E-7	2.1E-7	1.3E-7	1.0E-7	1.0E-7	-	-	8.3E-7	1.7E-7	-	-	-	-	-			
Hastelloy-X	Total	1.7E-6	1.3E-7	6.7E-8	3.3E-8	3.3E-8	-	1.6E-6	9.6E-7	2.0E-7	(3.7E-10)	(3.6E-11)	-	-	-			
	m/e= 2(H ₂)	2.8E-7	1.9E-8	1.0E-8	5.3E-9	5.3E-9	-	2.0E-7	6.9E-8	2.4E-8	(2.3E-10)	(1.1E-11)	-	-	-			
	16(CH ₄)	5.1E-8	5.1E-9	2.8E-9	1.3E-9	1.3E-9	-	-	-	-	(1.7E-11)	-	-	-	-			
	18(H ₂ O)	7.3E-7	5.3E-8	2.7E-8	1.1E-8	1.1E-8	-	3.6E-8	-	-	-	-	-	-	-			
Molybdenum	Total	8.0E-8	6.7E-9	3.7E-9	2.1E-9	2.1E-9	-	1.2E-6	6.0E-7	1.3E-7	(1.1E-11)	(6.7E-12)	-	-	-			
	m/e= 2(H ₂)	1.1E-5	1.6E-7	3.2E-8	4.7E-9	4.7E-9	2.5E-6	6.3E-7	4.0E-7	1.6E-7	1.7E-10	9.3E-11	6.9E-11	5.1E-11	-			
	18(H ₂ O)	4.0E-6	7.6E-8	1.3E-8	1.9E-9	1.9E-9	6.2E-7	1.6E-7	8.0E-8	2.0E-8	9.3E-11	4.4E-11	2.7E-11	1.5E-11	-			
	44(CO ₂)	8.0E-7	1.2E-8	3.1E-9	3.3E-10	3.3E-10	7.7E-7	1.7E-7	1.3E-7	7.3E-8	1.7E-12	9.3E-13	8.0E-13	8.0E-13	-			
Pyrolytic graphite	Total	3.6E-7	2.9E-9	6.7E-10	-	-	-	-	-	-	3.2E-11*3	2.7E-11*3	2.7E-11*3	2.7E-11*3	-			
	m/e= 2(H ₂)	1.1E-6	1.3E-7	5.3E-8	2.0E-8	2.0E-8	1.1E-5	4.7E-6	2.6E-6	1.0E-6	(1.2E-9)	(1.6E-10)	(1.3E-10)	(1.3E-10)	-			
	16(CH ₄)	2.4E-7	1.7E-8	7.3E-9	3.7E-9	3.7E-9	1.5E-6	1.8E-7	1.0E-7	4.0E-8	(8.6E-10)	(1.3E-10)	(1.0E-10)	(8.0E-11)	-			
	28(CO)	4.8E-7	6.4E-8	2.5E-8	9.3E-9	9.3E-9	6.9E-7	6.7E-8	-	-	(6.0E-11)	(4.7E-12)	(2.7E-12)	(2.0E-12)	-			
SiC coated onto graphite	Total	1.5E-5*1	3.6E-6	1.3E-6	4.8E-7	4.8E-7	2.4E-5	5.2E-6	3.5E-6	-	-	-	-	-	-			
	m/e= 2(H ₂)	4.8E-6*1	8.0E-7	4.0E-7	1.5E-7	1.5E-7	1.5E-5	4.8E-6	1.9E-6	-	-	-	-	-	-			
	16(CH ₄)	4.5E-7*1	6.7E-8	-	-	-	-	-	-	-	-	-	-	-	-			
	28(CO)	2.7E-6*1	4.0E-7	1.6E-7	3.7E-8	3.7E-8	2.8E-6	5.3E-7	1.5E-7	-	-	-	-	-	-			

*1: The outgassing rates at 2 hours from starting pumping.
 *2: The outgassing rates at 0.35 hours after the heater is turned off.
 *3: Nitrogen is a dominant gas in this stage.
 *4: The expression 2.9E-6 shows 2.9 x 10⁻⁶.

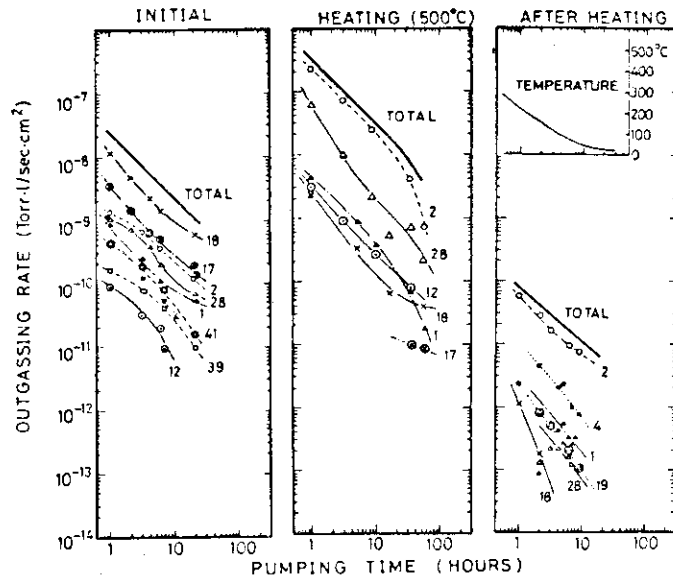


Fig. 4 Outgassing rates of SUS 304L. $M/e=16, 19, 39$ and 41 are systematic errors due to vacuum pumping system and ions produced by surface ionization at the ion source of the mass spectrometer. Some of these peaks should be subtracted from the graph, for evaluation of outgassing rates of substrate materials.

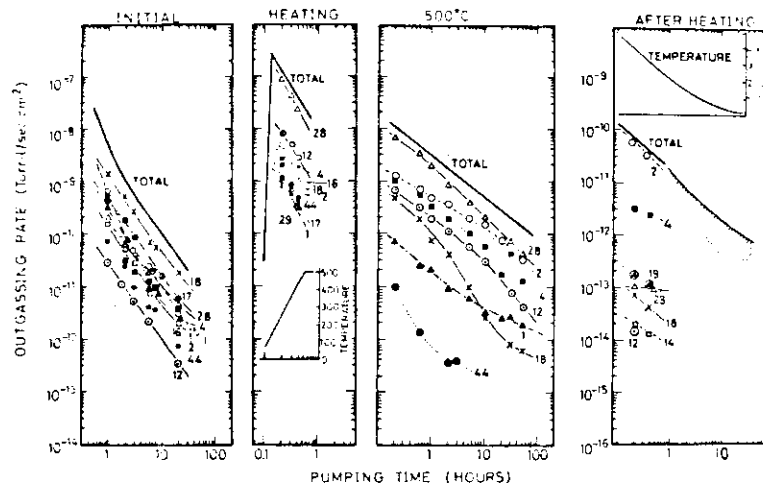


Fig. 5 Outgassing rates of YUS-170. Otherwise, similar to Fig. 4.

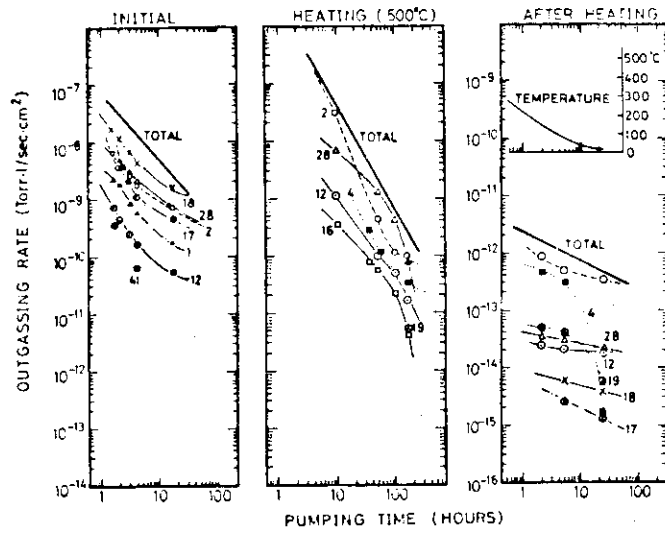


Fig. 6 Outgassing rates of Inconel-625. Otherwise, similar to Fig. 4.

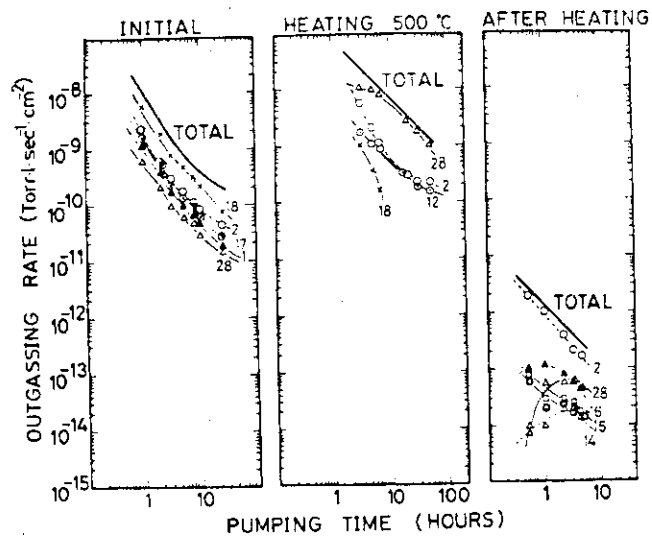


Fig. 7 Outgassing rates of Hastelloy-X. Otherwise, similar to Fig. 4.

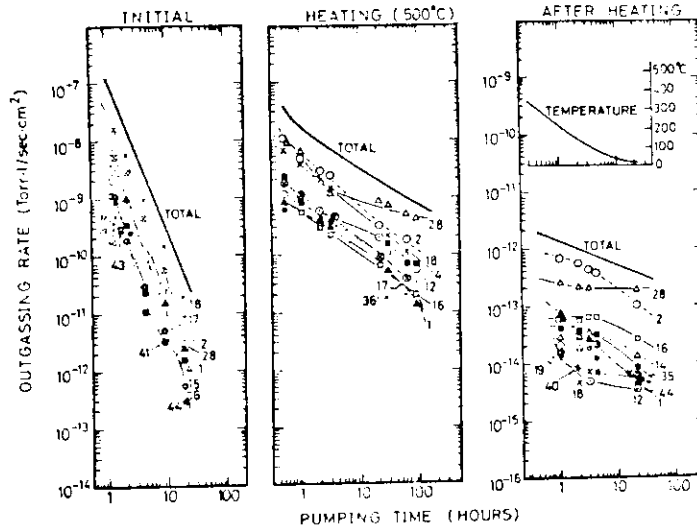


Fig. 8 Outgassing rates of Molybdenum. Otherwise, similar to Fig. 4.

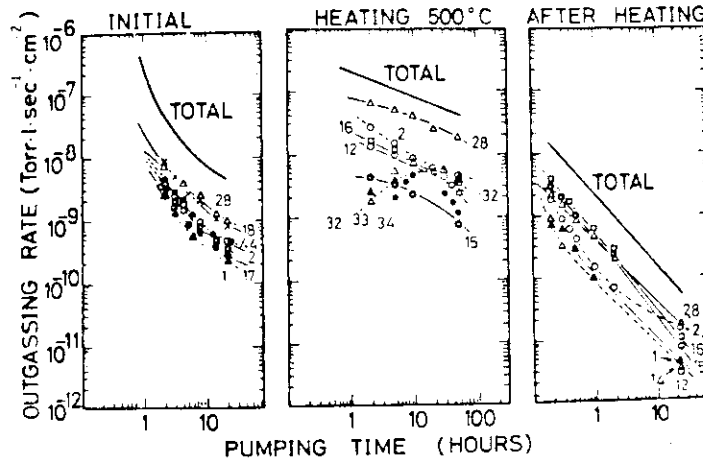


Fig. 9 Outgassing rates of SiC coated onto graphite. Otherwise, similar to Fig. 4.

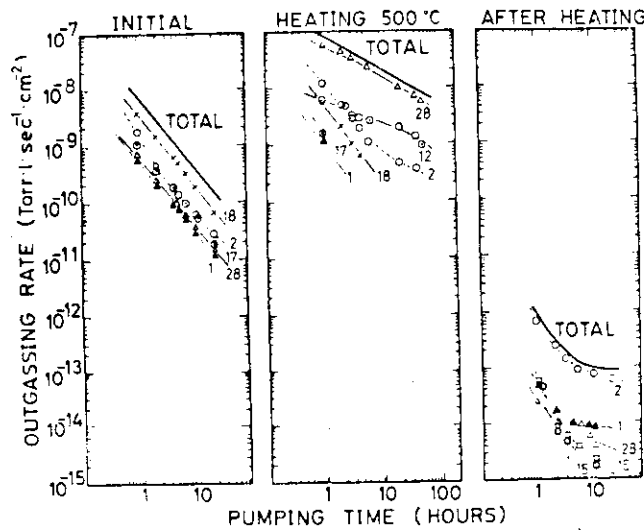
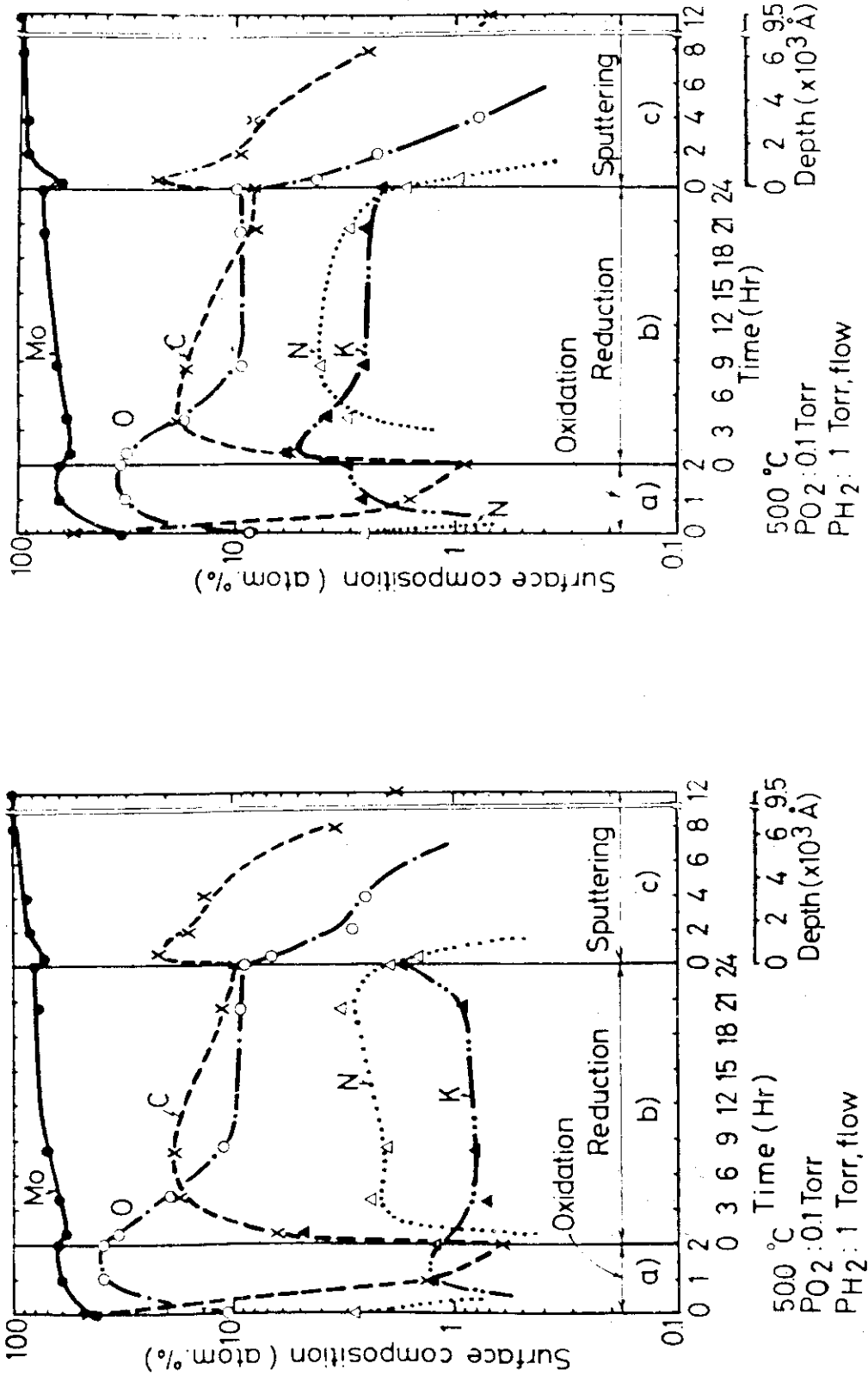


Fig. 10 Outgassing rates of Pyrolytic Graphite. Otherwise, similar to Fig. 4.



(a) (b)

Fig.11 Surface compositions of sample A (left) and B (right) during surface treatments at 500°C, and their depth profiles after treatments. Samples are exposed to air for 4 days after a glow discharge cleaning.

Table 3 Improved plasma parameters by LDC and HDC

	V_l (volt)	Z_{eff}	t (hrs.)
LDC	1.9	3.2 ~ 4.3	3 ~ 4
HDC	2.2 ~ 2.4	3.8 ~ 5.6	40 ~ 60

Notation t indicates required time to obtain steady, stable discharges by discharge cleaning, after the vacuum chamber was exposed to air.

V_l and Z_{eff} are one-turn voltage and mean ionic charge of the plasma.

Respective plasma parameters in LDC and HDC are :

LDC $I_p \sim 5kA$, $P_f \sim 2 \times 10^{-4}$ Torr, Rep. rate=1/0.7 PPS,
Duty cycle of discharges=1/28, $T_e \sim 5eV$;

HDC $I_p=50 \sim 100$ kA, $P_f \sim 2 \times 10^{-4}$ Torr, Rep. rate=1/60 PPS,
Duty cycle of discharges=1/1200, $T_e=200 \sim 300$ eV.

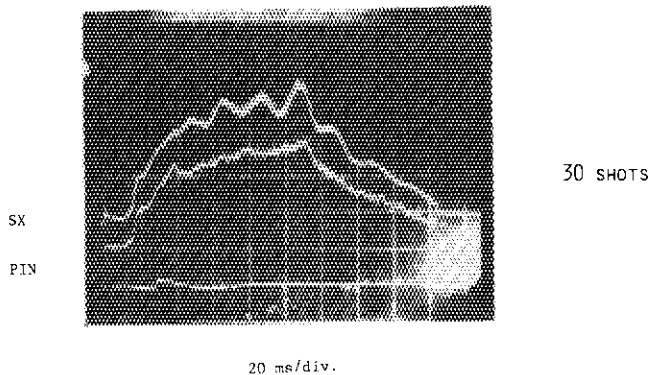
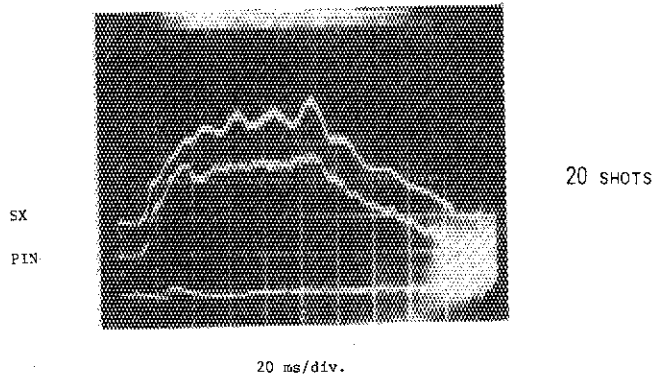
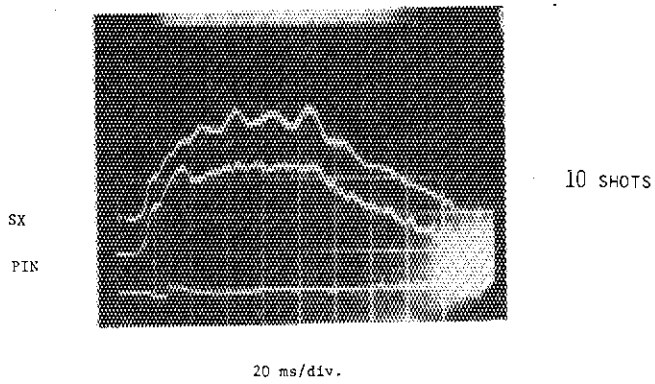


Fig. 12 Time behaviour of the signals from SX and PIN diode. These signals show that the clean surface is contaminated shot by shot.

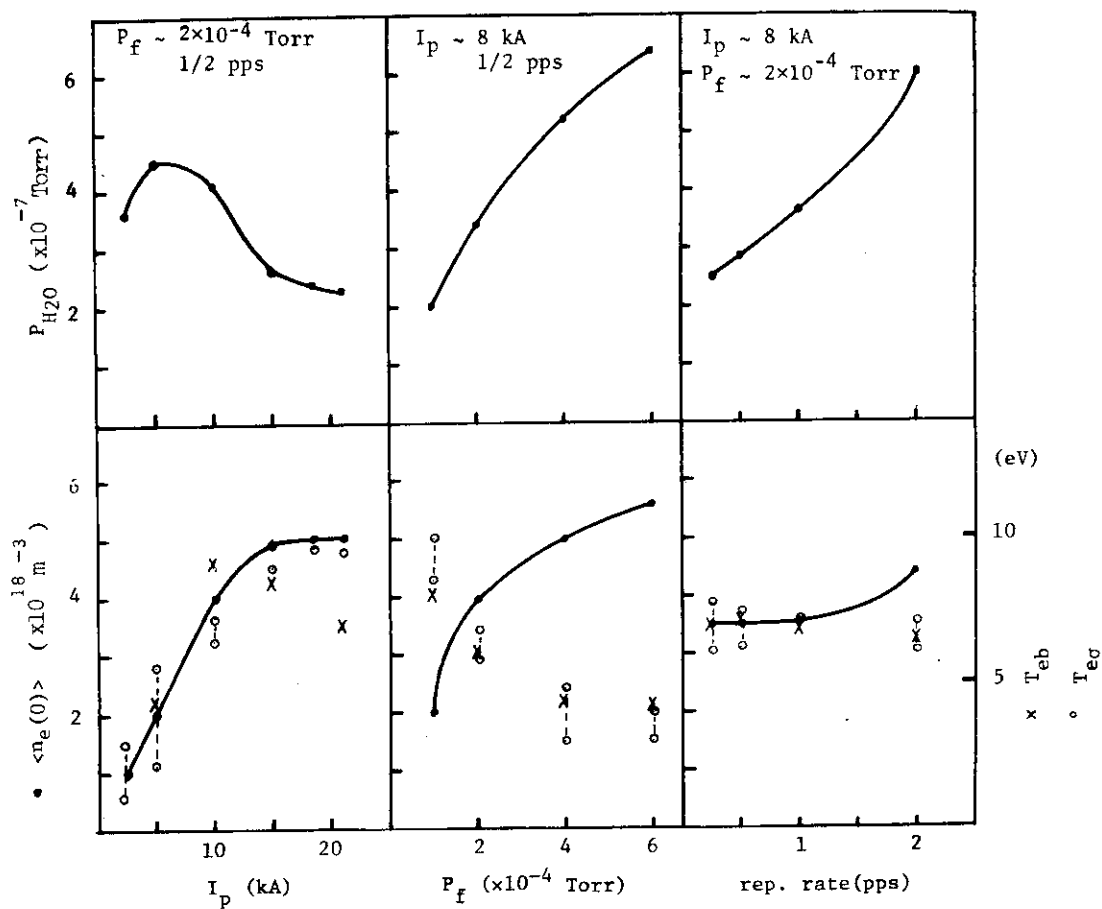


Fig. 13 Dependency of water molecule production on LDC parameters: plasma current (I_p), filling pressure (P_f) and repetition rate of discharge. $\langle n_e(0) \rangle$ is the electron density of central line average. T_{eb} is the boundary electron temperature measured by a double probe. $T_{e\sigma}$ is the conductivity temperature on the assumption that $Z_{eff} = 1$.

Table 4
Impurity contamination in cases with and without Ti-gettering

	Oxygen				Carbon C V (a.u.)	Iron Fe XV (a.u.)	Molybdenum Mo XIII (a.u.)	Bremsstrahlung radiation (a.u.)	Z_{eff}
	O VIII	O VII	O VI	O V					
Without Ti-coating	4.1 (1E12)	1.1 (5E11)	0.05 (3E10)	0.002 (2E9)	13	10	14	30	5.5
With Ti-coating	0.51 (2E11)	0.14 (9E10)	0.004 (3E9)	- (2E8)	1	1.3	1.3	5	2

\bar{n}_j = ground level population density [e.g. (2E10) should be read as $2 \times 10^{10}/\text{cm}^3$].

$Z_j = Z_f(Z_j - 1)\bar{n}_j/n_e$; $Z_j = j$ th ionization state.

$Z_{eff} \propto V_L/(I_P R) \int_0^a T_{e0}^{3/2}(r) r dr$.

Note: Discharge conditions are the same as in fig. 14.

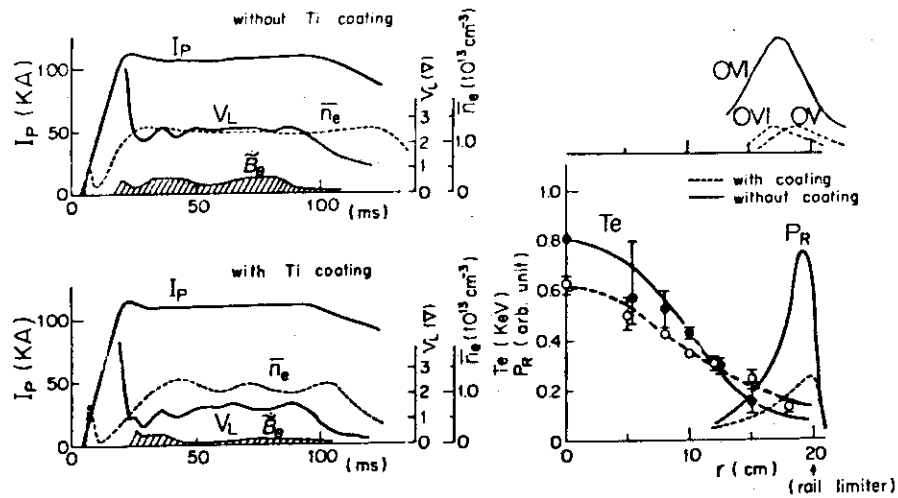


Fig. 14

Time evolution of plasma current I_P , loop voltage V_L , mean line of sight electron density \bar{n}_e , and relative amplitude on magnetic probe signal \bar{B}_θ , indicating the effect of Ti-gettering (left). Radial profiles of electron temperature (T_e) and radiation loss (P_R : Abel inverted) with and without gettering at $t = 70$ ms (right). Peak positions and relative intensities of O VI and O V line emission are also shown.

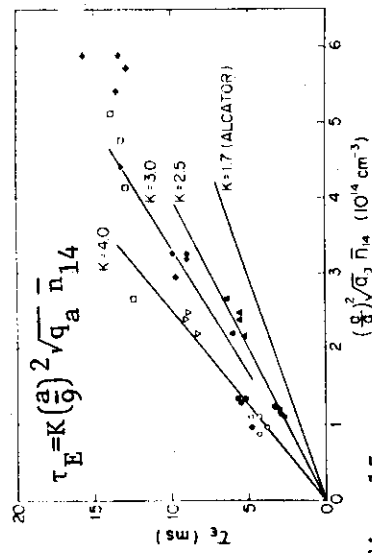


Fig. 15

Energy confinement time τ_E , as a function of "modified" ALCATOR scaling (see text). Discharge conditions are following: \square, ∇, \circ ; limiter radius $a = 20$ cm, $q_a = 4$, with Ti-gettering. $\blacktriangle, \bullet, \blacklozenge$; $a = 20$ cm, $q_a = 4$, without Ti-gettering. $\blacklozenge, \blackstar$; $a = 25$ cm, $q_a = 4$, without Ti-gettering.

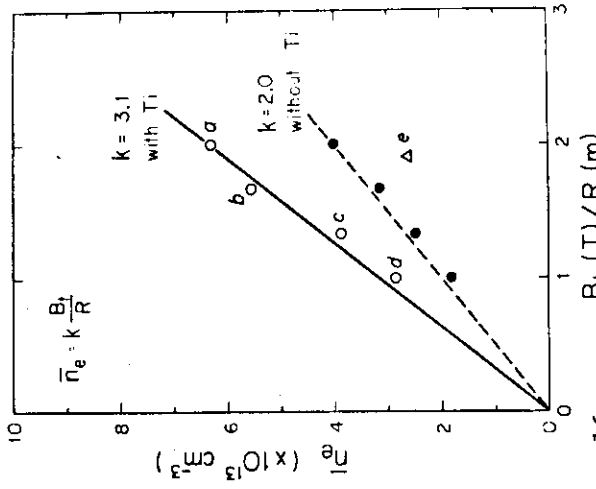


Fig. 16 Maximum mean electron density (\bar{n}_e) versus B_t/R with (open circles) and without (full circles) Ti-gettering. Power allocation at a time of \bar{n}_e peak for discharges marked a to e is listed below:

	a	b	c	d	e	
Joule input						
P_{IN} (kW)		270	220	130	120	160
Radiation power						
P_R (kW)		~ 210	~ 170	~ 80	~ 60	~ 30
$\Delta P = P_{IN} - P_R$ (kW)			~ 60			~ 130

(Discharge marked e corresponds to a relatively low density case, for comparison.)

4.2 Effect of Low Z Materials

The advantage of low Z materials is its large allowable concentration in the plasma. However, in application to the first wall of large tokamaks with higher temperatures and longer duration times, there are many problems as follows;

1) Poor thermal property

Surface temperature rise is proportional to the temperature rise parameter $(\lambda c \rho)^{-0.5}$, where λ ; thermal conductivity, c ; specific heat, ρ ; density. Since low Z materials have large temperature rise parameter, evaporation becomes more serious than refractory materials such as Mo. Low Z coating or cladding onto the metal substrate such as Mo, W is useless, since these thin layers will be soon consumed by sputtering, since sputtered materials will amount to the order of ton/year in INTOR. Pyrolytic graphite (PyG) is one of the potential materials because of its high heat conductivity along the deposition plane. However, it is under development as to a realistic structure of PyG limiters or divertor plates with cooling mechanisms as schematically shown in Fig. 1.

2) Thermal shock

In the runaway electron discharge, the heat flux to the limiter or divertor plate might be 10^4 w/cm² - 10^5 w/cm². Since low Z materials are generally brittle one, brittle failure seems to be probable under the runaway electron bombardment. Selection of material and structure which have large thermal shock resistance, or suppression of runaway electron discharge is necessary.

3) Micro-powder contamination

If micro-powders of low Z materials stick to the first wall surface, they will enter into the plasma during discharge. A few mg of micro-powders exceed the permissible level. Removal of micro-powders is necessary before the construction of the first wall, and/or removal of micro-powders by in-situ cleaning method such as discharge cleaning.

4) Chemical sputtering

Fundamental experiments show that low Z materials such as carbon and carbide have sputtering yield by nearly two orders of magnitude larger than those of metallic ones in the temperature range of 400 ~ 800 °C. Control of the first wall temperature, below 300 °C or around about 1000 °C, or suppression of chemical sputtering by plasma polymerization is necessary. However, large chemical sputtering has not been observed in actual devices as described below.

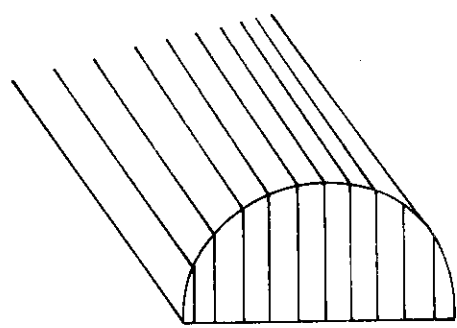
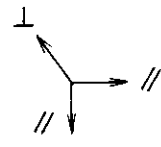
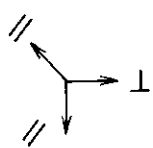
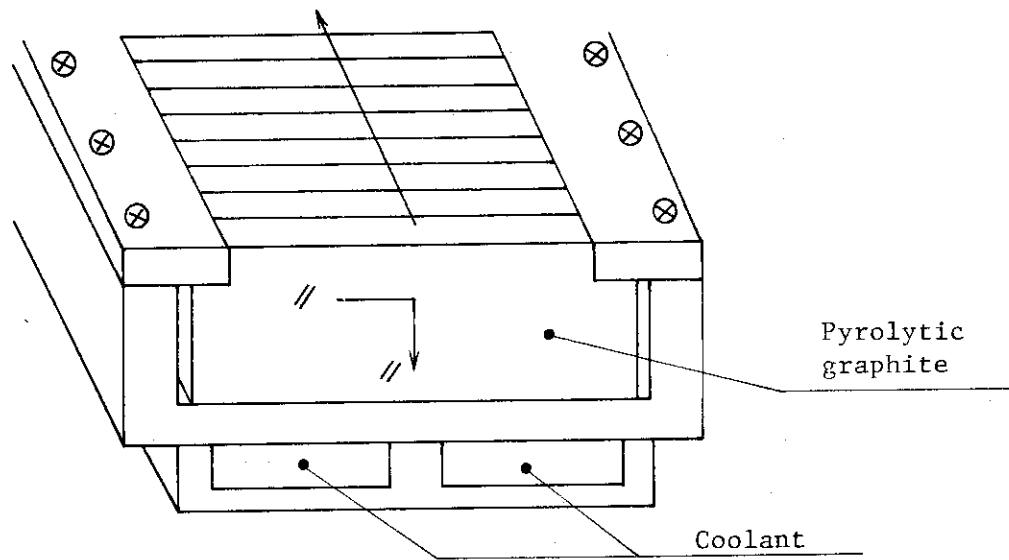
In the basic experiments in the absence of atomic hydrogen in the atmosphere, chemical sputtering yields of low Z materials strongly depend on material temperature and also incident energy as commonly observed (Figs. 2, 3)¹⁾.

However, in a basic experiment in the existence of atomic hydrogen, chemical sputtering yield is very small and strong dependence on material temperature has not been observed. One of the possible explanation is passivation on the surface layer by atomic hydrogen which suppresses the methane formation (Figs. 4, 5)²⁾.

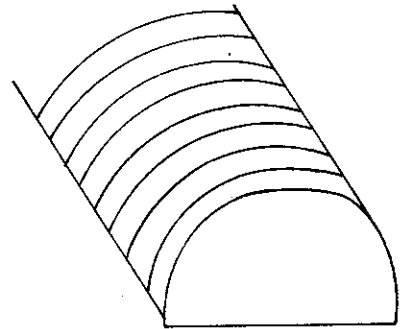
Similar results have been observed in JFT-2 and DIVA tokamak experiments.

References

- 1) R. Yamada, et al., to be published.
- 2) T. Abe, et al., to be submitted to J. Nucl. Mat.



Type A



Type B

Fig. 1 Examples of the divertor plate or the material limiter making use of good thermal property of PyG(//)

// ; high heat conduction direction
 ⊥ ; low heat conduction direction

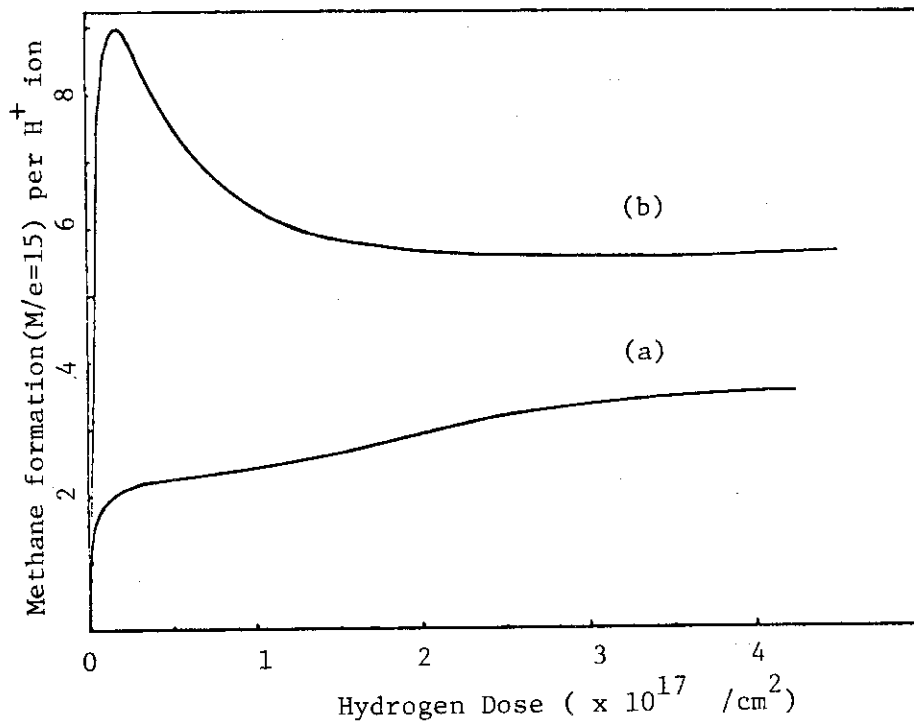


Fig. 2 Dose dependence of methane formation from a pyrolytic graphite bombarded with hydrogen ions. (a) 0.5 keV, 500°C; (b) 1 keV, 500°C.

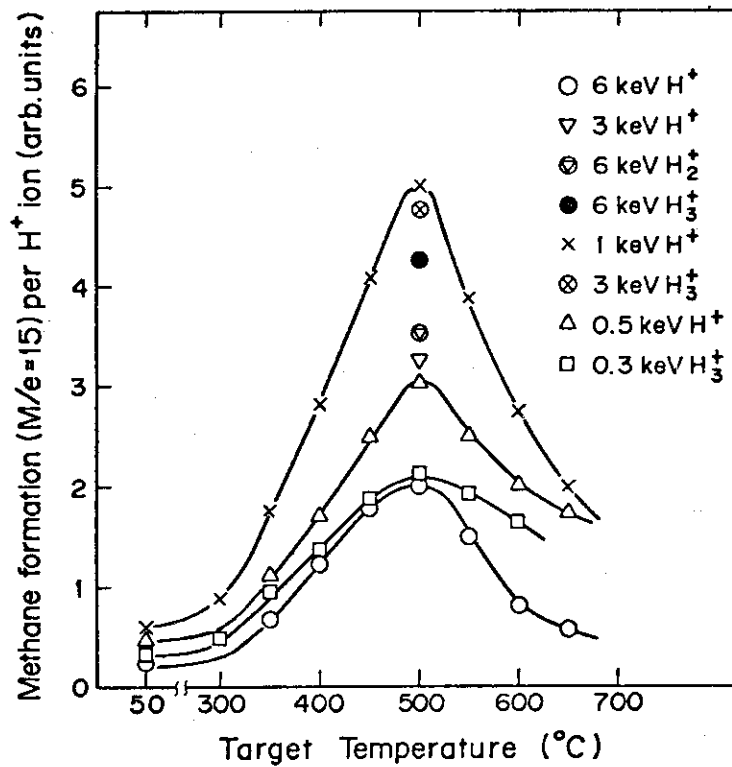


Fig. 3 Steady rate of methane formation from a pyrolytic graphite bombarded with hydrogen ions.

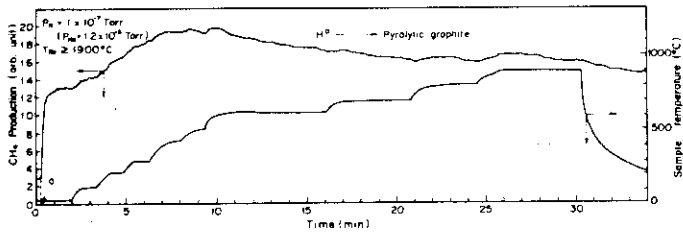


Fig. 4(a)

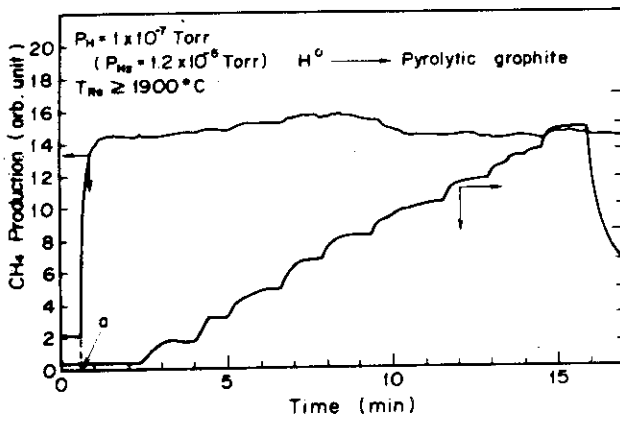


Fig. 4(b)

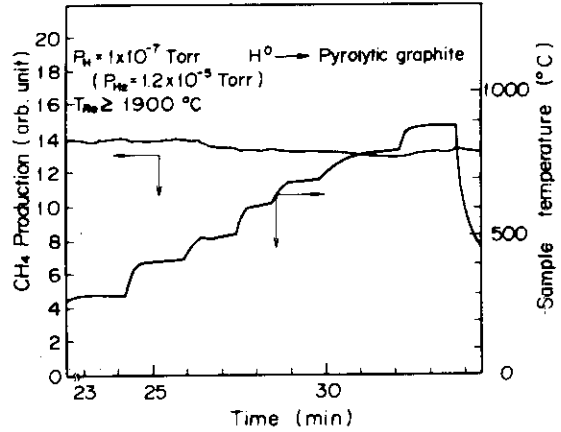


Fig. 4(c)

Fig. 4 Variation in methane production from pyrolytic graphite exposing to atomic hydrogen as a function of exposure time and sample temperature. First, second and third runs are 4(a), 4(b) and 4(c), respectively.

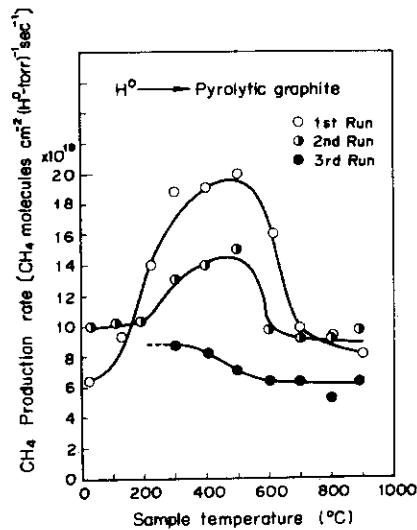


Fig. 5 Measured methane production rate from pyrolytic graphite as a function of sample temperature.

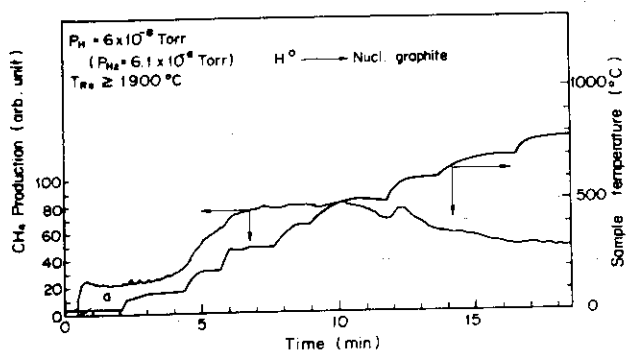


Fig. 6(a)

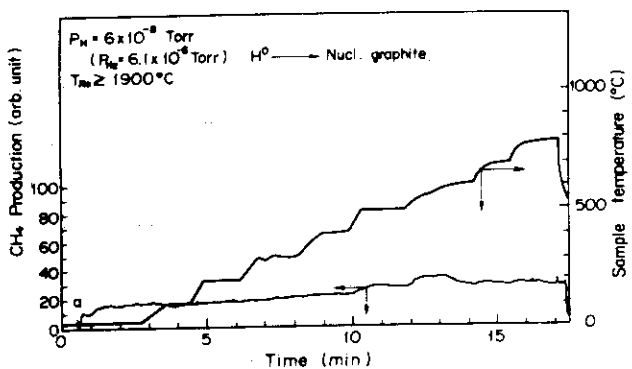


Fig. 6(b)

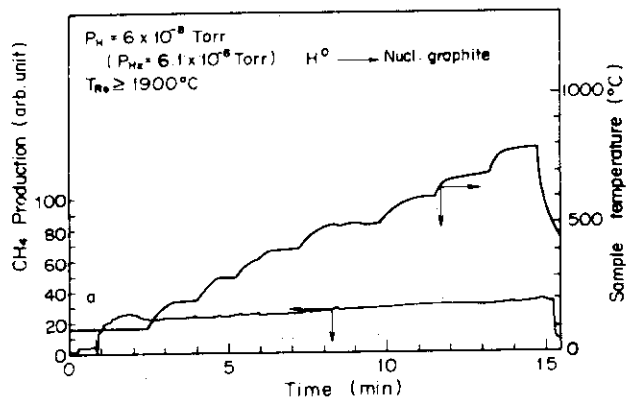


Fig. 6(c)

Fig.6 Variation in methane production from nuclear grade graphite exposing to atomic hydrogen as a function of exposure time and sample temperature. First, second and third runs are 6(a), 6(b) and 6(c), respectively.

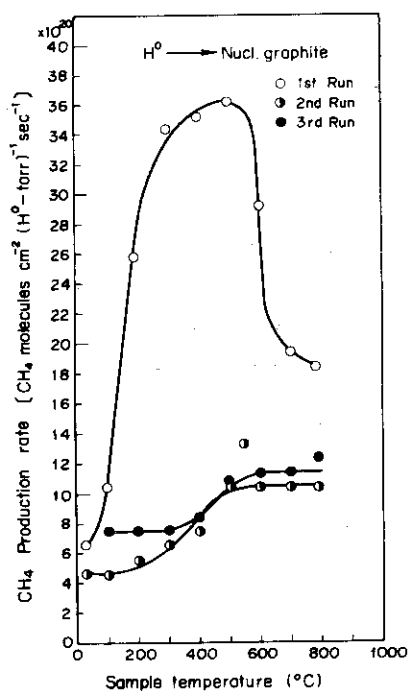


Fig.7 Measured methane production rate from nuclear grade graphite as a function of sample temperature.

5. DIVERTOR CASE FOR IMPURITY CONTROL & ASH EXHAUST

5.1 Results of Divertor Experiment in DIVA

1) Equilibrium

Stable configurations with a separatrix magnetic surface by using a divertor coil current I_D and a copper shell.¹⁾²⁾³⁾

$$\left\{ \begin{array}{ll} I_D/I_P < 0.7 & : \text{conventional discharge} \\ 0.7 < I_D/I_P < 2.0 & : \text{divertor discharge} \\ I_D/I_P > 2.0 & : \text{positionally unstable discharge} \end{array} \right.$$

Dynamic magnetic limiter operations are stable demonstrated. Configurations change with a time constant of the energy confinement time⁴⁾.

The non-axisymmetric perturbation deforms the old separatrix magnetic surface and there appears an ergodic region around the old separatrix. $\delta B/B = 0.1\%$ is expected in DIVA where δB and B are the perturbation field and the toroidal magnetic field. Average safety factor is around 10 and the width of the ergodic region is about 5 mm with $q_{ac} = 4$ where q_{ac} is the safety factor in a circular cross-sectional tokamak with the same major and minor radii. These expected values are consistent with experimental results (Figs. 1 and 2)⁵⁾.

2) Stability

The separatrix magnetic surface stabilizes the surface mode (Fig.3)⁶⁾⁷⁾. The separatrix magnetic surface does not affect the tearing mode triggering the major disruption³⁾⁶⁾⁷⁾. No major disruption is observed in impurity free plasmas with and without the divertor. And the major disruption is excited with both of the impurity injection and the internal disruption. The amount of injected impurities exciting the major disruption with the divertor is two times larger than without the divertor⁶⁾⁷⁾. No major disruption can be excited in the non-divertor and divertor discharges with $q_a < 2$ ⁶⁾⁷⁾ (Fig. 4).

3) Confinement

Impurity reduction by the divertor or by other methods increases the energy confinement by a factor of 2.5 by increasing the radius of the hot

column (Figs. 5 and 6⁷⁾⁸⁾⁹⁾¹⁰⁾). Impurity reduction by the divertor does not affect the particle confinement time. Impurity reduction of the divertor dose not affect the diffusion and thermal conduction coefficients¹⁰⁾¹¹⁾.

The average particle confinement time is almost equal to the energy confinement time with a low level of impurity radiation loss and is larger than the energy confinement time with a normal level of impurity radiation loss (Fig. 7)¹⁰⁾. A modified ALCATOR scaling can well describe the observed energy confinement time both with and without the divertor.

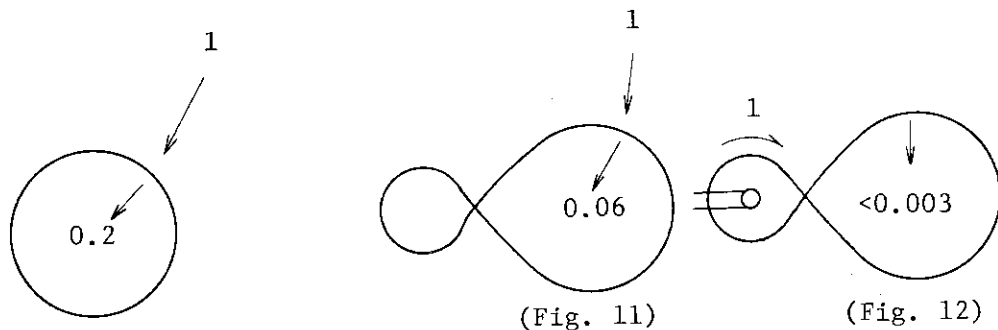
$$\tau_E = 1.8 \times 10^{-14} \sqrt{q_a} \bar{n}_e a_{\text{half}}^2 \text{ sec. (Fig. 8)}$$

Where q_a , \bar{n}_e and a_{half} are the safety factor, the mean electron density in cm^{-3} , and the half radius of the electron temperature profile in cm. The divertor increases a_{half} by reducing the impurity level⁷⁾.

4) Impurities¹²⁾¹³⁾¹⁴⁾¹⁵⁾¹⁶⁾¹⁷⁾¹⁸⁾

Transport in the main plasma is well described by combining the neoclassical and anomalous effects. The anomalous diffusion coefficient is equal to that of protons and is $4 \times 10^3 \text{ cm}^2/\text{sec}$ with $\bar{n}_e = 1 \times 10^{13} \text{ cm}^{-3}$. Transport in the scrape-off layer is well described by a Monte Carlo code (see subsection 5.4).

Impurity influxes to the hot column are shown in the following figure. (Figs. 9~12)



Divertor reduces the impurity radiation loss by a factor of 2-4. The effective reduction is observed in a high current discharge. The result is consistent with the result of 5).

5) Scrape-off plasma with and without the divertor

(1) Scaling laws¹⁰⁾¹¹⁾¹⁹⁾²⁰⁾

The energy and particle conservation laws give the following simple formulas for plasma parameters in the scrape-off layer, i.e. electron temperature T_{es} , width of the scrape-off layer d , the density n_{es} , the particle flux density f_p and the heat flux density q :

$$\bar{T}_{es} = \frac{3\bar{\tau}_p(P_{in} - P_{cx} - P_R)}{2\tau_E P_{in} \gamma} (\bar{T}_e + \bar{T}_i) \quad (1)$$

$$d = \sqrt{D_{\perp} L / v_f} \quad (2)$$

$$\bar{n}_{es} = \frac{L \bar{n}_e a}{2v_f \bar{\tau}_p d} \quad (3)$$

$$f_p = \bar{n}_{es} v_f \quad (4)$$

$$q = \gamma \bar{T}_{es} f_p \quad (5)$$

γ , D_{\perp} , v_f and L are the heat transport rate, the diffusion coefficient, the particle flow velocity, and the half length of the magnetic field line between the material surfaces in the scrape-off layer, respectively, and P_{in} , P_{cx} , P_R , $\bar{\tau}_p$, τ_E , T_e , T_i , n_e and a are input power, charge-exchange loss-power, radiation loss-power, particle confinement time, energy confinement time, electron temperature, ion temperature, density and minor radius in the main plasma column, respectively. \bar{T}_{es} , d , \bar{n}_{es} , f_p and q can be calculated from these equations if we know v_f , γ , D_{\perp} and the parameters of the main plasma. The space potential and the floating potential which are also important parameters can also be estimated from these values by assuming a certain magnetic configuration and secondary-electron effects. Therefore, the essential parameters in the scrape-off-layer plasma are v_f , γ and D_{\perp} .

The following results are obtained with $B_T = 0.8 - 2.0$ T, $\bar{n}_{es} = (1.5 - 5.0) \times 10^{12} \text{ cm}^{-3}$, $\bar{T}_{es} = 20 - 100$ eV and $\bar{T}_{is} = 20 - 80$ eV.

$$\begin{cases} v_f \sim 0.3 C_s \\ D_{\perp} \sim 0.1 D_B \text{ (Fig. 13)} \\ \gamma \geq 100 \text{ in runaway discharges} \\ \gamma \sim (8-15) \text{ in normal discharges (Fig. 14)} \end{cases}$$

Where C_S and D_B are sound velocity and the Bohm diffusion coefficient. The observed γ in normal discharges are well described by the sheath model including the effects of secondary electrons and epithermal electrons.

The scrape-off-layer plasma and the relation between the particle confinement time and the energy confinement time were investigated; the following results were obtained: $v_f \sim 0.3 C_S$, $\bar{\tau}_p/\tau_E \sim 1$, $D \sim 0.1 D_B$ and $\gamma \sim 7$. Thus, Eq. (1) is simplified as follows:

$$\bar{T}_{es} \sim 0.2 \frac{(P_{in} - P_{cx} - P_R)}{P_{in}} (\bar{T}_e + \bar{T}_i) \quad (6)$$

This equation shows that temperature at the edge is extremely high in a high-temperature tokamak with $P_{in} \gg P_{cx} + P_R$, and it is expected that the surface erosion and the impurity production become serious. Thus, some method of cooling the plasma edge down to a sufficient low temperature, typically several tens of electron-volts, is required in conventional devices as discussed in subsection 5.4.

(2) Shielding and back flow¹⁴⁾¹⁵⁾

It is rather easy to shield the impurity influx (Fig. 11). Neutral particles can penetrate into the main plasma because the charge-exchange process is dominant and the wall-reflection gives a high energy to the influx particles. Impurities do not flow back into the main plasma column from the burial chamber (Fig. 12). No artificial pump for metallic impurities is necessary in the burial chamber and gas impurities are easily controlled by cleaning the vacuum vessel. Therefore, there is no difference between the magnetic limiter (e.g. that of JT-60) and the divertor concerning the impurity control.

References

- 1) M. Yoshikawa, T. Tazima, Y. Shimomura, A. Kitsunezaki, H. Maeda, et al., Plasma Physics and Controlled Nuclear Fusion Research 1 (Tokyo, 1974) 17.
- 2) Y. Shimomura, Proc. 7th Europ. Conf. on Controlled Fusion and Plasma Physics 1 (Lausanne, 1975) 81.
- 3) Y. Shimomura, H. Maeda, H. Ohtsuka, A. Kitsunezaki, T. Nagashima, et al., Phys. of Fluids 16 (1976) 1935.

- 4) Y. Shimomura, H. Ohtsuka, H. Maeda, S. Yamamoto, H. Kimura, et al., Nuclear Fusion 16 (1976) 584.
- 5) S. Yamamoto, S. Sengoku, H. Kimura, et al., Nuclear Fusion 18 (1978) 205.
- 6) K. Odajima, M. Nagami, S. Yamamoto, et al., Symposium on Current Disruption in Toroidal Devices, Garching (1979).
- 7) DIVA Group, JAERI-M 8205 (1979).
- 8) S. Yamamoto, H. Maeda, Y. Shimomura, K. Odajima, et al., Proc. 8th Europ. Conf. on Controlled Fusion and Plasma Physics (Prague) 1, 33 and 2, 123 (1977).
- 9) H. Maeda, S. Sengoku, K. Kimura, H. Ohtsuka, et al., Plasma Physics and Controlled Nuclear Fusion Research (Innsbruck) T-3-1 (1978).
- 10) DIVA Group, Nuclear Fusion, 18 (1978) 12.
- 11) Y. Shimomura and H. Maeda, J. Nuclear Materials 76 & 77 (1978) 45.
- 12) H. Maeda, N. Fujisawa, Y. Shimomura, A. Funahashi, H. Ohtsuka, et al., Plasma Physics and Controlled Nuclear Fusion Research 2 (Berchtesgaden, 1976) 289.
- 13) H. Maeda, H. Ohtsuka, Y. Shimomura, S. Yamamoto, M. Nagami, et al., Plasma Wall Interaction (Julich, 1976) p. 537.
- 14) M. Nagami, H. Maeda, S. Kasai, Y. Yamauchi, et al., J. Nuclear Materials 76 & 77 (1978) 521.
- 15) S. Sengoku, M. Nagami, H. Maeda, et al., Journal of Physical Society of Japan, 45 (1978) 1385.
- 16) M. Nagami, Y. Shimomura, H. Maeda, S. Kasai, T. Yamauchi, et al., Nuclear Fusion, 18 (1978) 1347.
- 17) M. Nagami, H. Maeda, T. Sugie, et al., 18 (1978) 1217
- 18) M. Nagami, JAERI-M 8215 (1979).
- 19) Y. Shimomura, Nuclear Fusion 17 (1978) 1217.
- 20) H. Kimura, H. Maeda, H. Ueda, M. Seki, et al., Nuclear Fusion, 18 (1978) 1217.

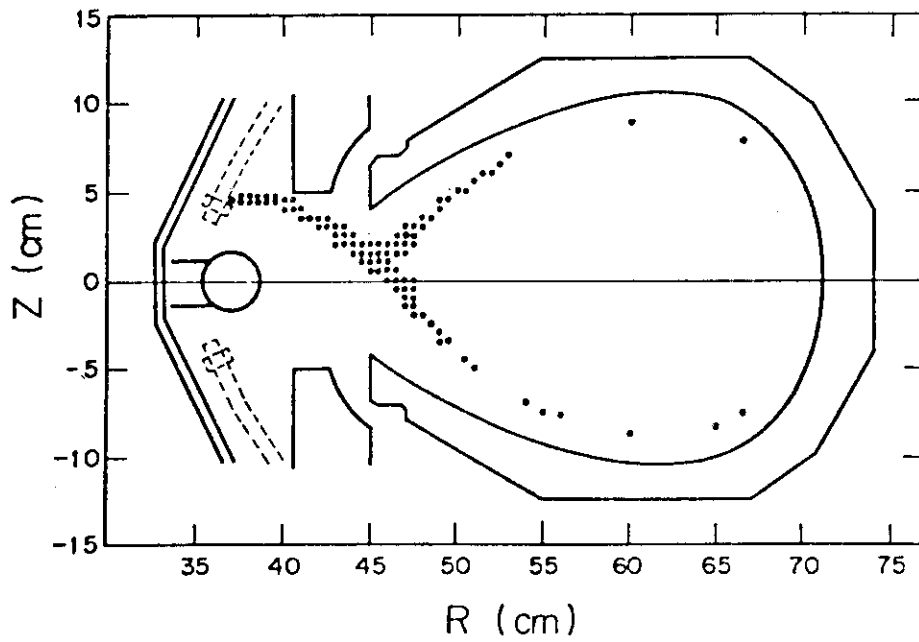


Fig. 1 Path of high-energy electrons (10keV - 100keV)at 20ms.

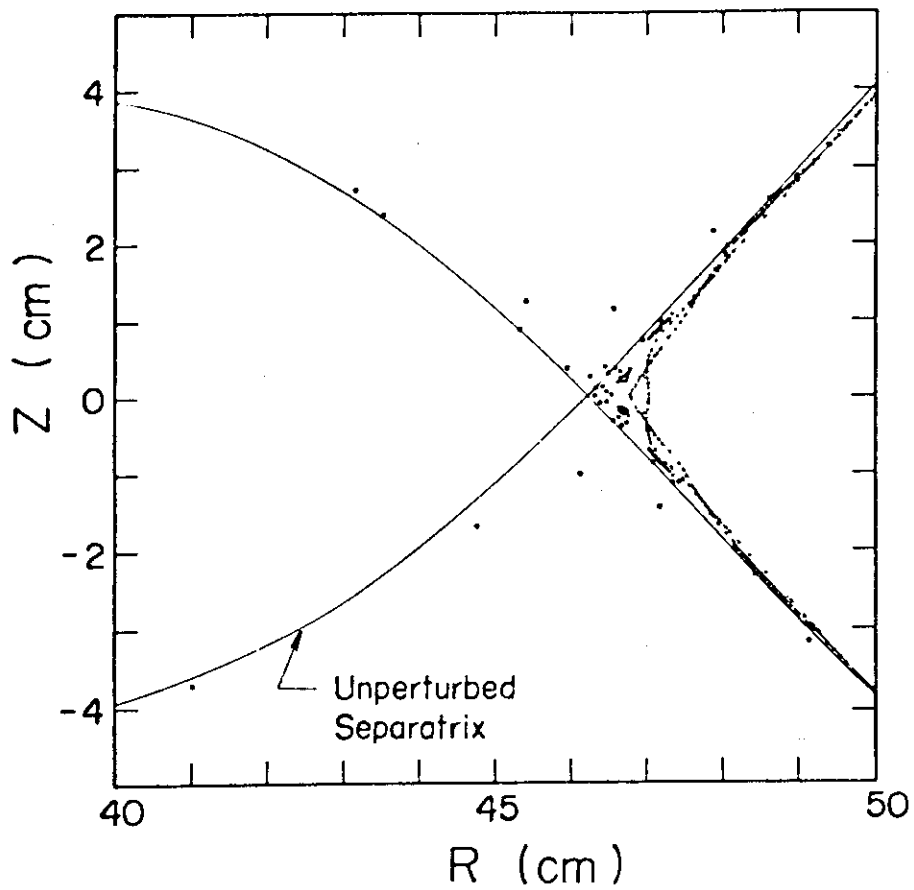


Fig. 2 The solid line shows the old separatrix. Island structures are observed on the old $q = 10$ and $q = 11$ rational surfaces.

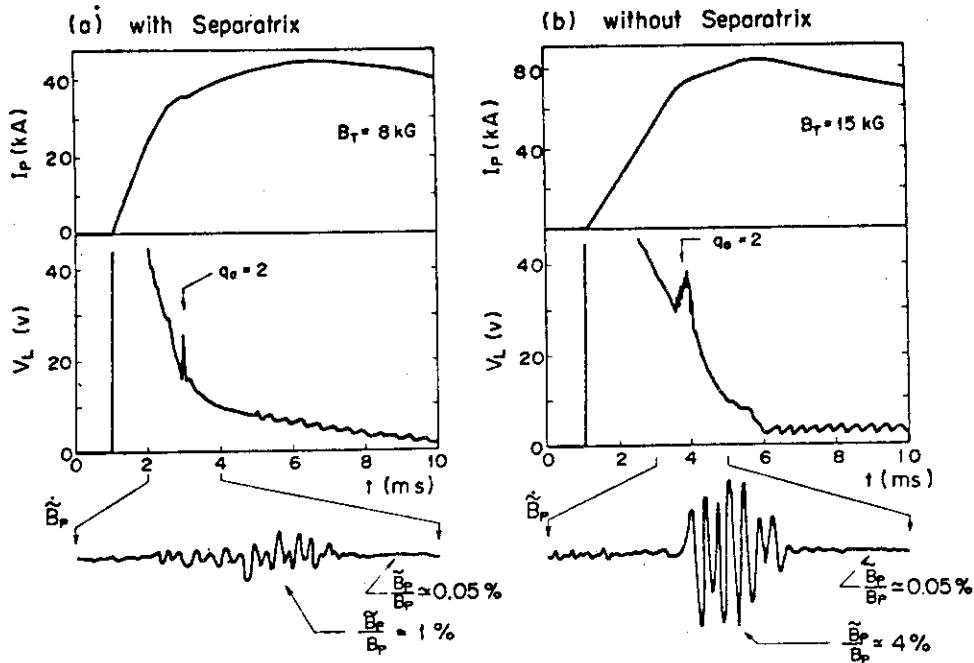


Fig. 3 Oscillogram of plasma current I_p and loop voltage V_L , with scanning time of 2 ms, and oscillogram of mhd activity with scanning time of 200 μ s, during the current rise phase for two discharges with and without separatrix. These figures show separatrix has a stabilizing effects on the surface mode.

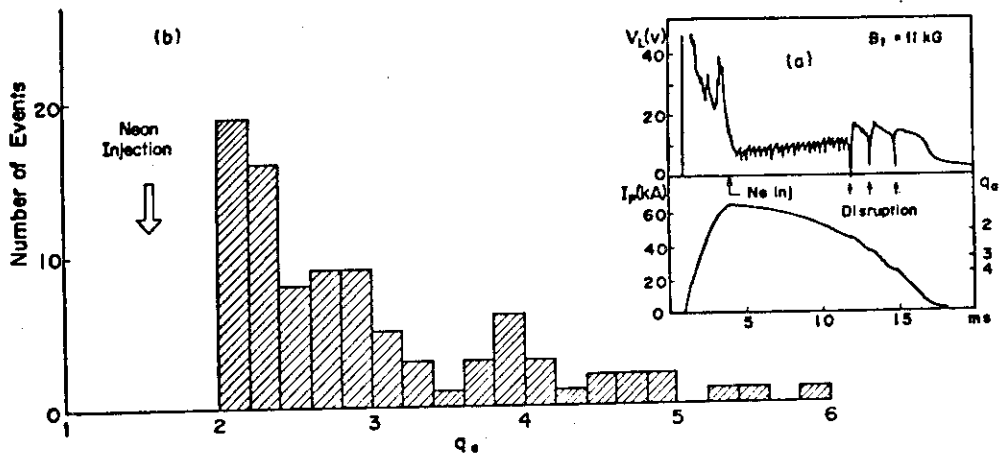


Fig. 4 Typical plasma parameters and number of occurrence of observed disruptions at different q_a when neon is injected into the stable $q_a = 1.6$ discharge. Major disruptions do not occur when the safety factor q is less than 2.

(a) Time behavior of the loop voltage and the plasma current with neon injection at 4 ms into the stable $q_a = 1.6$ discharge. The loop voltage increases at increasing radiation loss, and the plasma current decreases due to increasing resistivity. After the safety factor q_a becomes larger than two, the first major disruption occurs, and a series of voltage spikes appears on the loop voltage.

(b) The number of occurrence of observed disruption at different q_a . Disruptions are frequently observed near $q_a = 2$

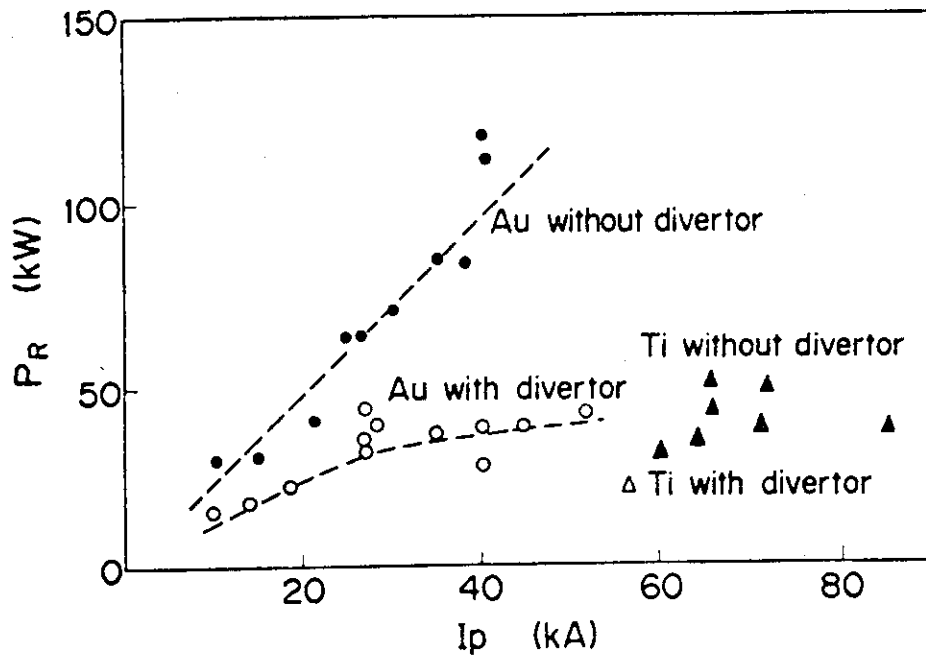


Fig. 5 Radiation loss power v.s. plasma current (Δ) and (\blacktriangle) show the present data.

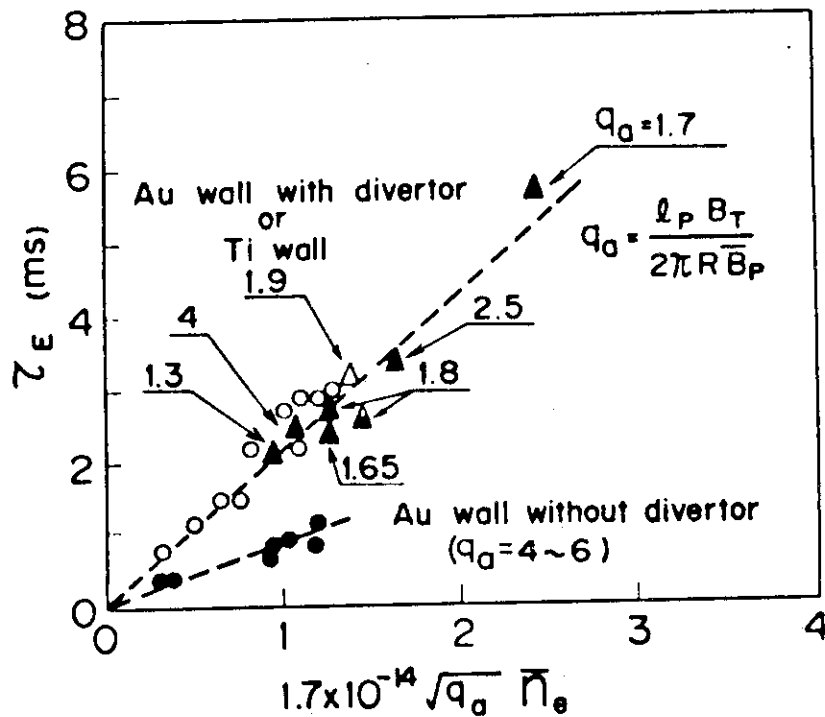


Fig. 6 Energy confinement time v.s. $q_a^{1/2} \bar{n}_e$ where \bar{n}_e is mean electron density in cm⁻³.

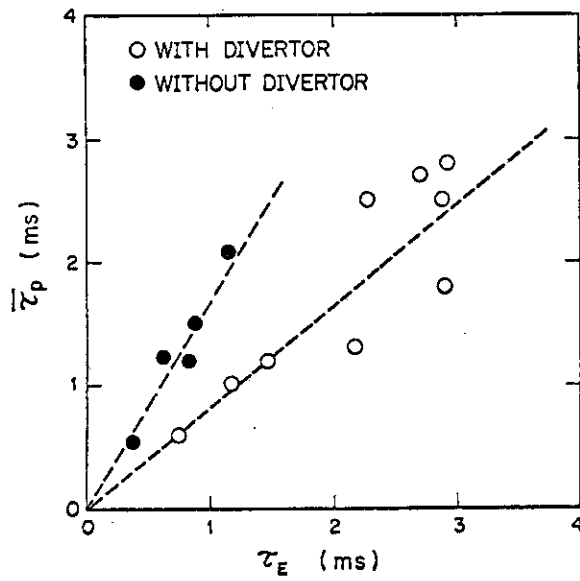


Fig. 7 Relation between the average particle confinement time $\bar{\tau}_p$ and the energy confinement time τ_E with and without the divertor. $B_T = 0.8 - 2.0$ T, $I_p = 10 - 53$ kA, $q_a = 2.6 - 5.9$, $\bar{n}_e = (1.5 - 5.0) \times 10^{13} \text{ cm}^{-3}$, $T_{i0} = 80 - 300$ eV and $T_{e0} = 200 - 700$ eV.

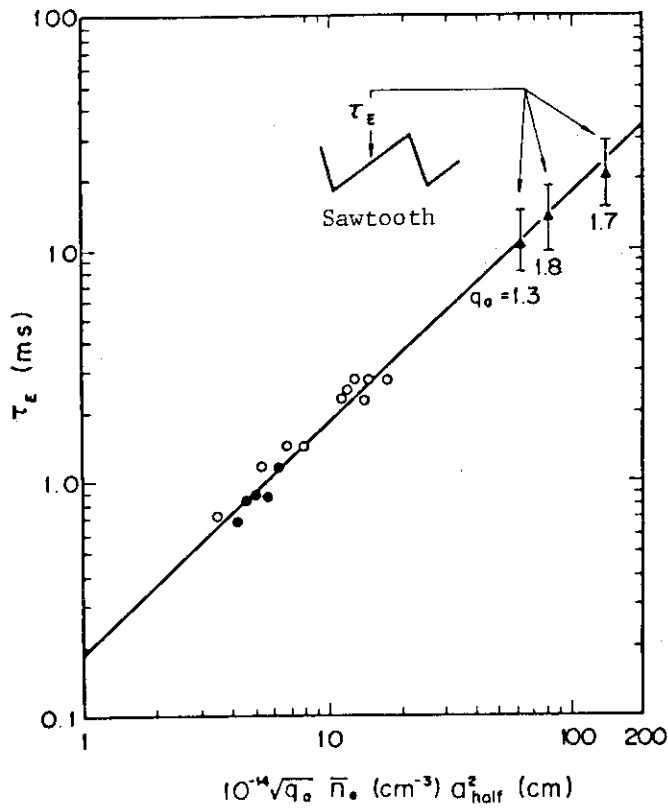


Fig. 8 Energy confinement time v.s. $q_a^{1/2} \bar{n}_e a_{\text{half}}^2$ where a_{half} is a half radius of an electron temperature profile. Discharge conditions are shown in Fig. 5.

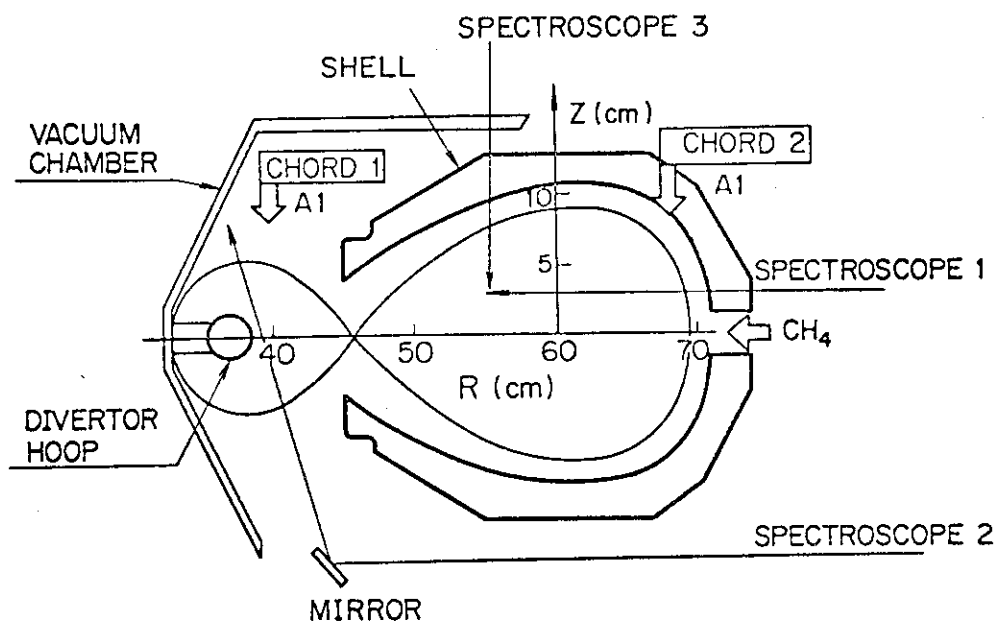


Fig. 9 Cross sectional view of DIVA tokamak and experimental arrangement showing the position of methane and aluminum injections, and sight-paths of four monochromators.

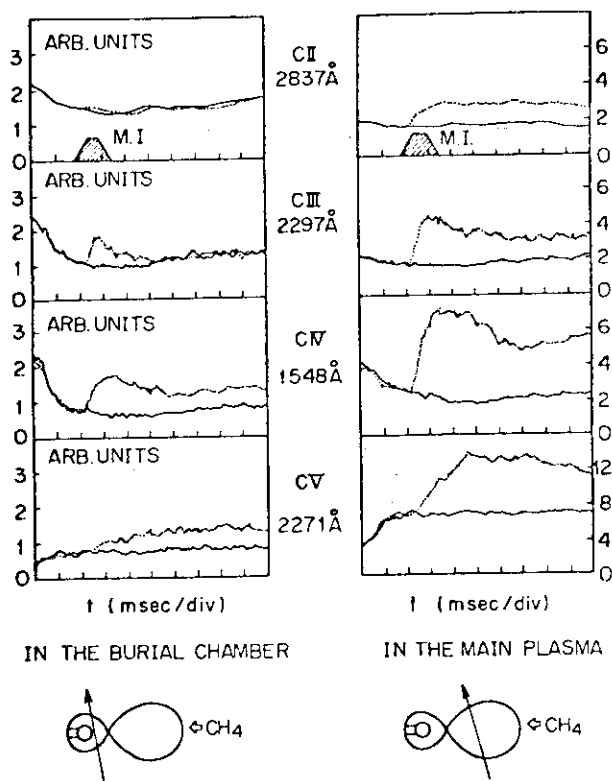


Fig. 10 Time development of the increase of line intensity from respective ionization states of carbon ions in the burial chamber and in the main plasma with the methane injection (M.I.) in diverted discharge. —: without injection,: with injection.

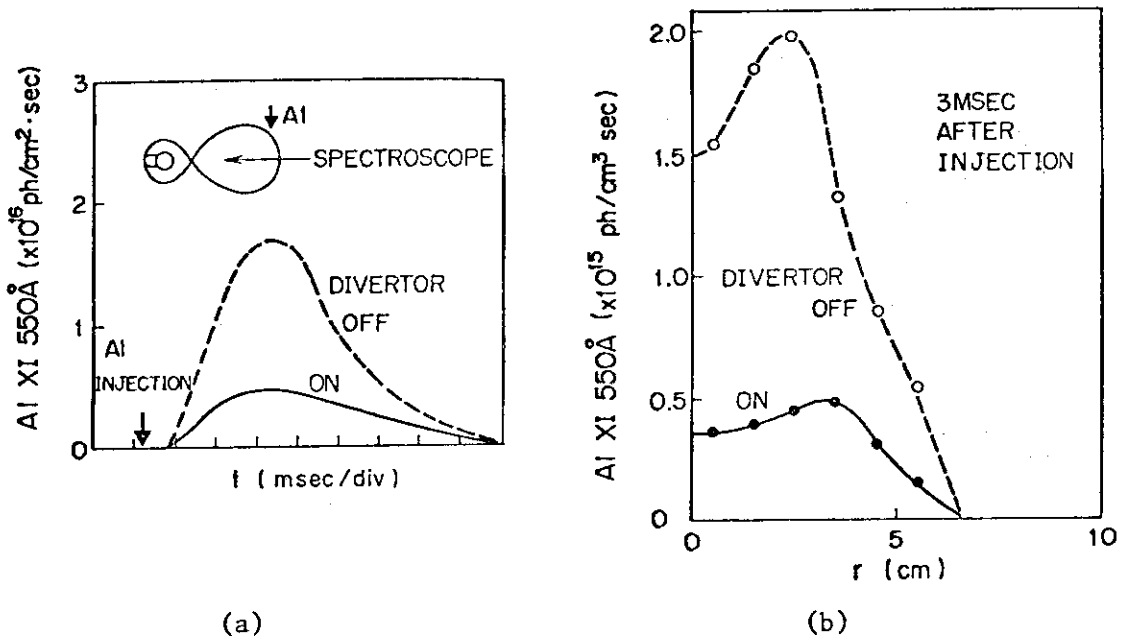


Fig. 11 (a) Time development of the line integrated emissivity of ALXI 550Å with the aluminum injection.
 (b) Abel-inverted volume emission of ALXI 550Å after 3 msec from the injection. Accumulation of the injected aluminum ions in the central region of the plasma is reduced by a factor of 3-4 by the divertor action.

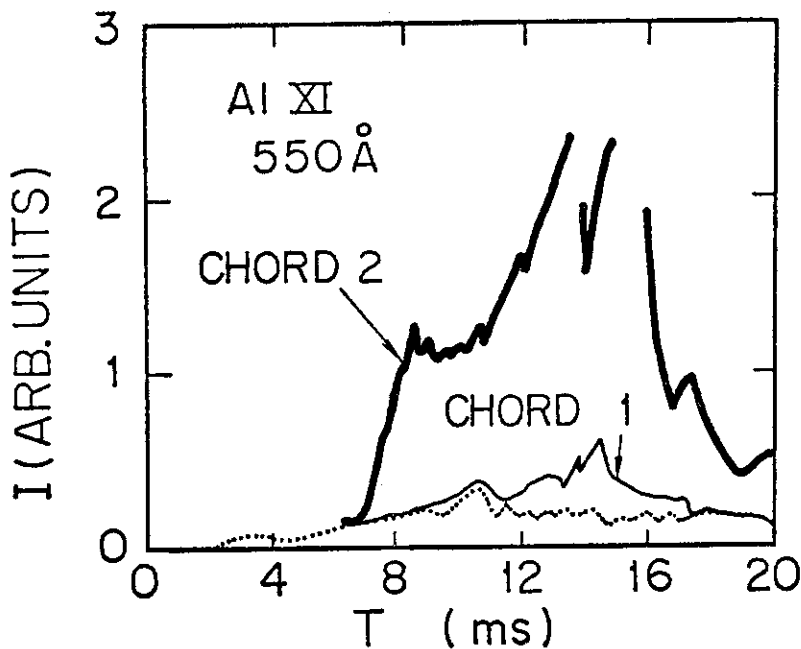


Fig. 12 Demonstration of the back flow of the aluminum ions from the burial chamber into the main plasma: solid lines indicate with the injections along the chords 1 and 2 indicated in Fig. 9. The dotted line indicates the background level of the ALXI 550 Å line emission.

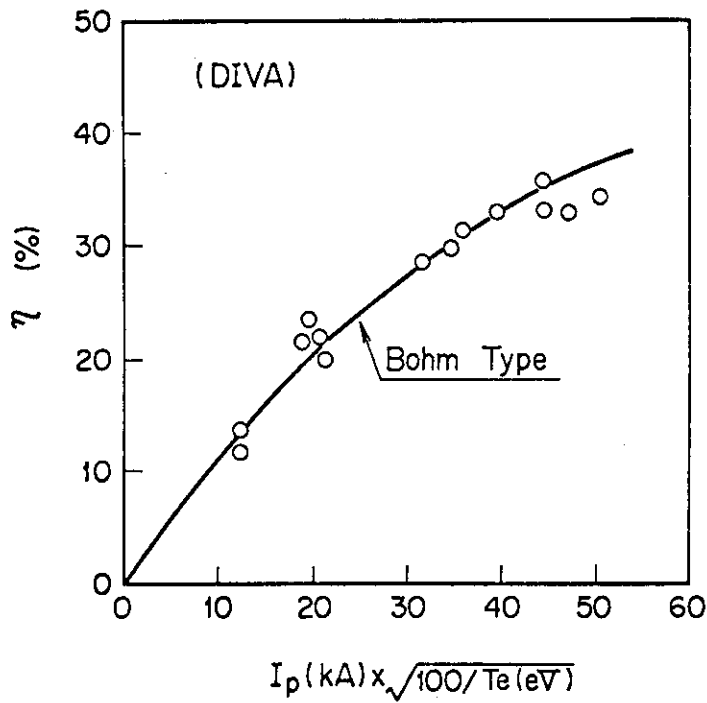


Fig. 13 Particle divertor efficiency η_p . $B_T = 0.8T - 2.0T$, $n_{es} = (1.5 - 5.0) \times 10^{12} \text{cm}^{-3}$ and $T_{es} = 20 - 100 \text{eV}$. The heat divertor efficiency is two times larger than the particle divertor efficiency.

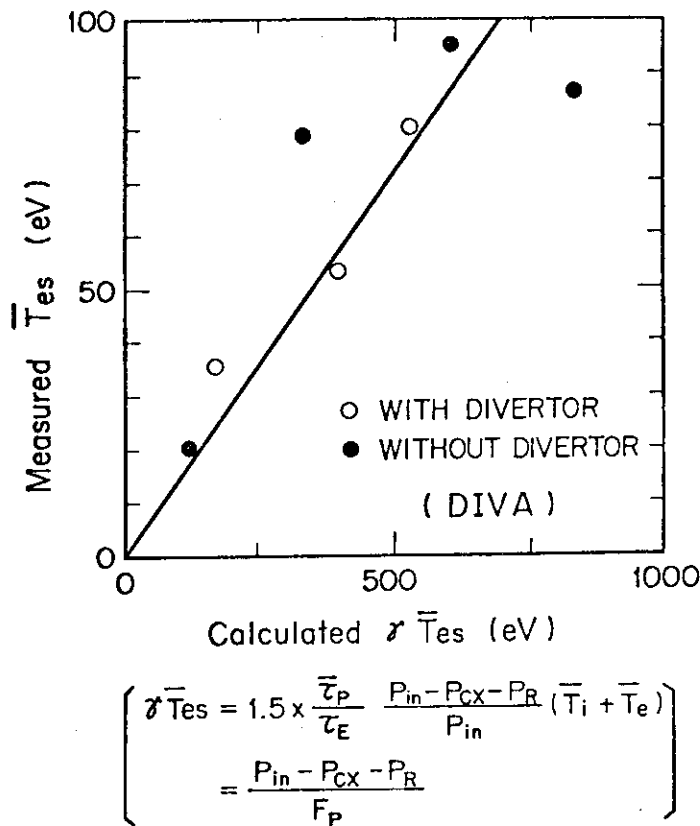


Fig. 14 Measured electron temperature \bar{T}_{es} in scrape-off-layer plasmas and calculated $\gamma \bar{T}_{es}$ from Eq.(1).

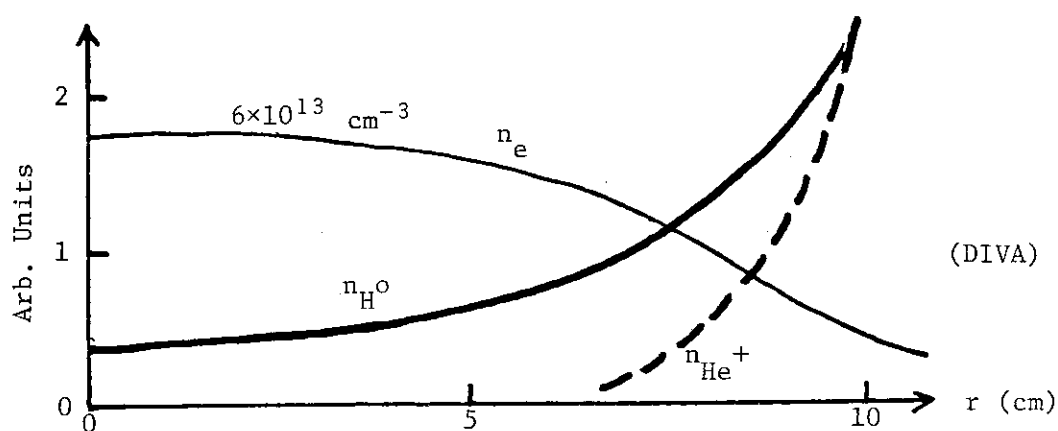
5.2 A Simple Poloidal Divertor with Exterior Coils¹⁾

Poloidal divertor whose coils and pumps are installed inside the vacuum chamber seems unrealistic for its serious technological difficulties. However, this problem can be overcome as follows (Fig. 1). Divertor coils can be located outside the toroidal coils, since we employ D-shape and the additional current of poloidal coils for poloidal divertor is very small.

Heat load to the neutralizer plate can be reduced down to 50 - 100 W/cm² by adding following methods. A small non-axisymmetric magnetic field (e.g. 0.2 % of the toroidal field) forms the ergodic region near the old separatrix and consequently spread the scrape-off layer by 10 - 20 cm, and moreover mirror effect may increase the width. However, it is necessary to swing the flux line by 10 cm as employed in JT-60 to unify peaked heat fluxes in this layer. And the neutralizer plate can be put almost parallel to the scrape-off layer.

Sputtered impurities from the neutralizer plate flow hardly into the bulk plasma and some of sputtered impurities directly thrust out the scrape-off layer and stick to the wall surface of the pumping chamber. Therefore, an artificial pumping system is not necessary for impurities in gas impurity free plasma. The pumping system is necessary only for the ash exhaust. Almost all the reflected helium atoms are ionized and flow back to the neutralizer plate by sheath potential, or freely into the pumping region. The thermal helium is easily ionized and flow hardly into the main chamber. The fuel particles, however, can easily flow into the main chamber because the charge exchange process is dominant except the case we employ the slits at divertor throats. Therefore, ashes can be enriched in the pumping region and exhausted by pumps located outside toroidal coils with pumping speed smaller than 10⁶ l/s. We can mitigate the required pumping speed when we employ slits at divertor throats to reduce the throat conductance.

It has been pointed out that this simple divertor has "ash enrichment action". This action is due to the characteristics of a rather thin scrape-off layer. This action is suggested from the simple poloidal divertor experiment but also from a conventional tokamak experiment as shown below.



Behavior of ash- and fuel-particles in the divertor region are numerically simulated by a Monte-Carlo method. (This model explained well impurity behavior in DIVA). The detailed result is shown in Sec. 5-3²). A typical result is shown below and Fig. 2. This result demonstrates the ash enrichment action and the realistic ash-pumping system in INTOR.

Back flow rate from the divertor to the main chamber

Throat length	Width	Back flow rate		Throat conductance for ash back flow	
		ash	fuel	Classical	With plasma
50 cm	30 cm	0.2	0.5	3000 m ³ /s	300 m ³ /s
	60 cm	0.5	0.8	10000 m ³ /s	1200 m ³ /s

References

- 1) Y. Shimomura, et al., JAERI-M 8294 (1979).
- 2) Y. Seki, et al., to be submitted to Nuclear Fusion (1980).

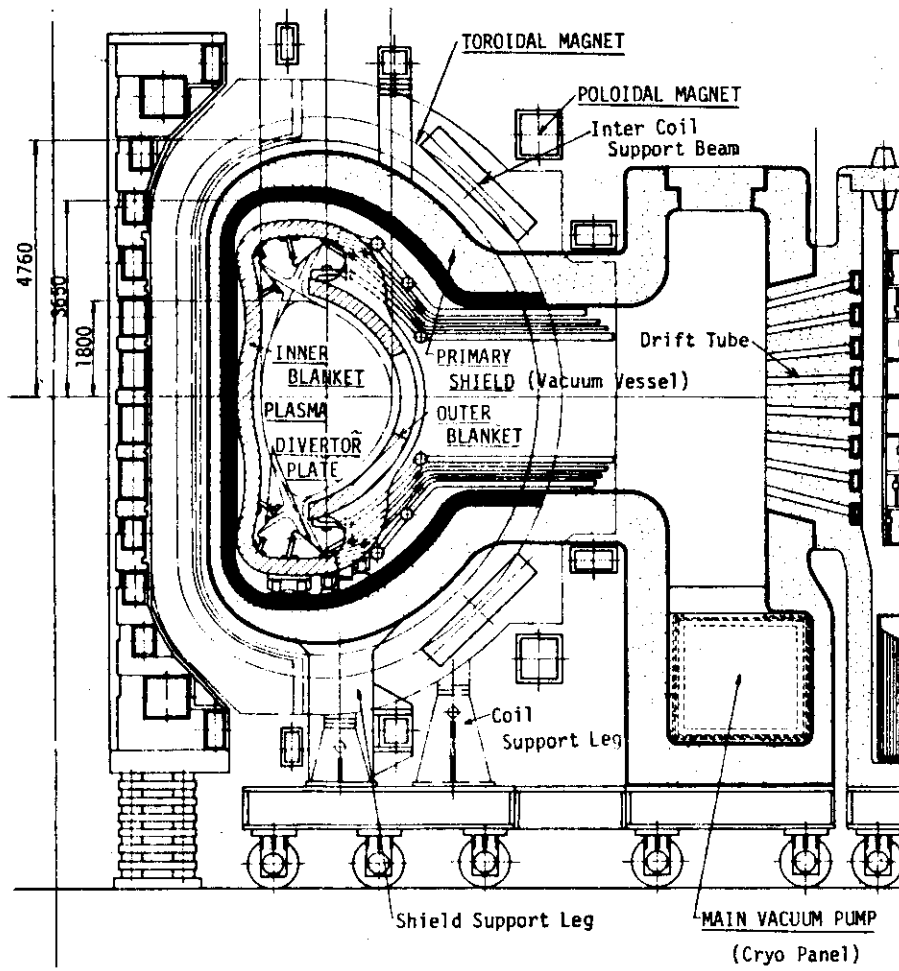


Fig. 1(a) A design example of a poloidal divertor with exterior coils.

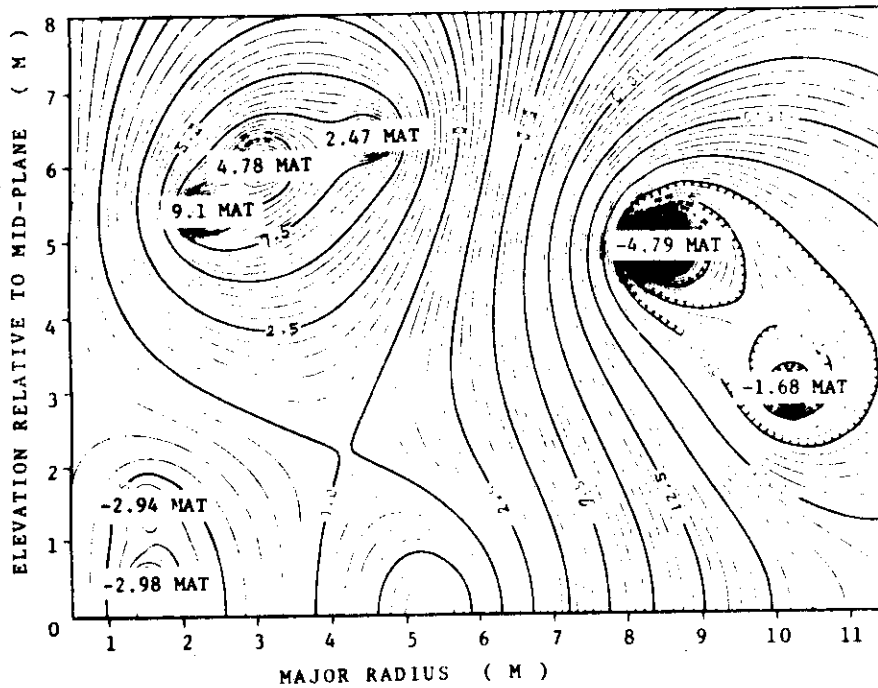


Fig. 1(b) A computed result of free boundary equilibrium of a poloidal divertor.

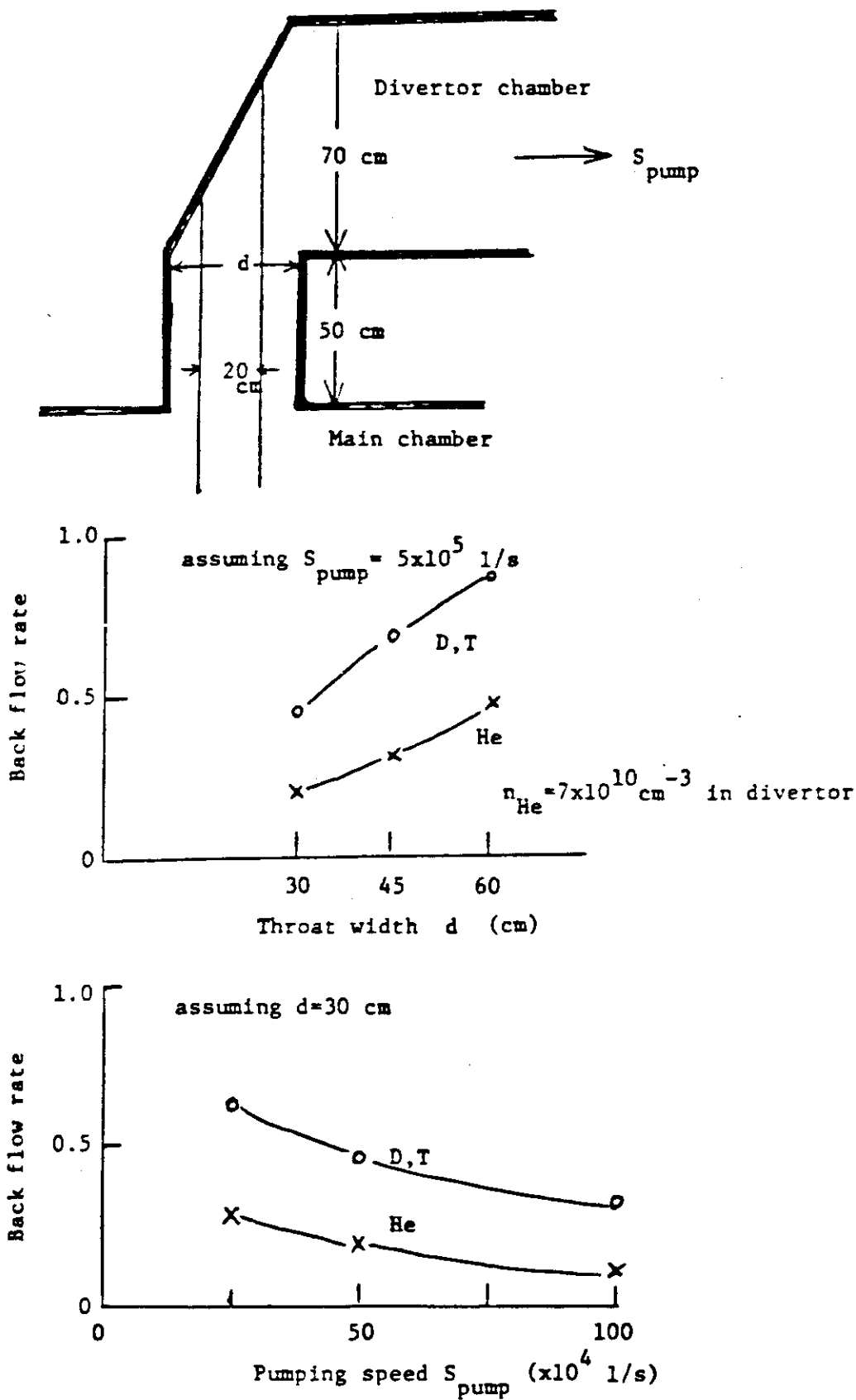


Fig. 2

5.3 Numerical Calculations of Helium Ash Enrichment and Exhaust by a Simple Poloidal Divertor¹⁾

1) Computational model

The motions of DT fuel and He ash particles in a simple poloidal divertor¹⁾³⁾ were simulated using a Monte Carlo method. The method and model employed for this calculation were developed on the basis of the impurity recycle calculation code made by M. Azumi and S. Sengoku, et al.⁴⁾ Cross sectional view of the reference reactor and an enlarged view of the divertor portion are shown in Figs 1a and 1b, respectively. Main parameters of the reference reactor are summarized in Table 1. The particles re-injected from the divertor neutralizer plate directly facing the pumping duct (the outer neutralizer plate) were followed. Figure 2 shows a simplified partial model, including only the outer neutralizer plate, employed for the calculation.

An orthogonal X-Y-Z coordinate system was used. The abscissa Z was taken in the direction of the divertor channel (throat) and the ordinate X in the divertor width direction as shown in Fig. 2. The toroidal component of the magnetic field is in the direction of Y-axis which is perpendicular to the page surface ($Y = 0$) of Fig. 2. The angle ω between the magnetic field line and the Z-axis changes from 90° at the null point ($Z = 0$) to 87.5° at the midpoint of the neutralizer plate ($Z = 85$ cm). Neglecting the effect of toroidal curvature, the cross section shown in Fig. 2 and the environmental conditions are assumed to be the same all along the Y-axis. The forces exercised on the charged particles and the velocity of the particles are considered in three dimensional space. However, the resulting particle motion is always projected on the $Y = 0$ surface.

As shown in Fig. 2, the model consists of a scrape-off layer, voids and a pumping duct which are surrounded by a neutralizer plate, walls, a duct exit (BB') and an interface (AA') with the main plasma.

The parameters of the scrape-off layer are given by the empirical scaling laws which were obtained in DIVA⁵⁾, i.e. $\bar{T}_b = 0.15 \bar{T} \left(\frac{P_\alpha - P_{cx} - P_R}{P_\alpha} \right) \left(\frac{\bar{\tau}_p}{\bar{\tau}_E} \right)$, $D_\perp = 0.1 D_B$ and $v_f = 0.3 C_s$.

The parameters for the standard case are summarized in Table 2. In the scrape-off layer there exists a particle flow with velocity v_f , as well as a pre-sheath field in the direction of the neutralizer plates. The Z component of the pre-sheath field E_z were taken from empirical

result as follows;

$$E_Z = \frac{C_E T_{eb}}{\ell_t} \cos\omega \quad (1)$$

where T_{eb} : electron temperature in the scrape-off layer,
 ℓ_t : length of the scrape-off layer,
 ω : angle between the magnetic field line and the Z axis in
the scrape-off layer,
 C_E : factor for pre-sheath field chosen as 0.5.

The void and the pumping duct regions were assumed to be filled with only neutral particles. Since no interaction between the neutral particles were assumed, these regions are essentially considered to be void where neutral particles move with a constant speed.

The neutralizer plate is made of copper and its temperature is assumed to be 500 °C. The wall is made of stainless steel with temperature 200 °C everywhere.

In order to make the conductance of the pumping duct more or less equivalent to the real configuration, at first its length was made long and its exit width narrow (see Fig. 2). After several trial calculations, however, it was found that most of the computation time was spent in calculating the motion of particles in the pumping duct. Therefore the length of the duct is shortened to 1 cm as shown as CC' in Fig. 2. To compensate for the shortened length, only a fraction $(1 - f_{\text{pump}})$ of the particles colliding the exit was allowed to go out. The rest, f_{pump} was made to be reflected at the collision point with thermal energy of the wall in the direction of cosine distribution. The value of f_{pump} should be determined from the magnitude of the pumping speed of the plasma column and the duct conductance and the pumping capability. The value of f_{pump} was calculated to be 0.9 based on a rough estimate assuming the pumping speed of 5×10^5 l/S.

2) Monte Carlo simulations

The following general scenario was assumed for each particle;

- (i) An ion of DT or He in the particle flow in the scrape-off layer is accelerated by the sheath potential and collide with the neutralizer plate.

- (ii) Neutralized particles are re-injected from the neutralizer plate into the scrape-off layer after backscattering or adsorption-desorption processes. Re-injected neutral particles move freely until they ionize, charge exchange, or collide with the walls.
- (iii) They may be ionized in the scrape-off layer. Ionized DT or He particles experience the acceleration due to the pre-sheath field and Coulomb scattering. They also diffuse perpendicular to field lines. The history of the ions which flow back onto the neutralizer plate is terminated and counted. The ions reaching the walls are neutralized and re-injected. When a neutral DT particle charge exchanges with another DT ion in the scrape-off layer, the movement of the newly created neutral DT particle is followed instead of the ionized one.
- (iv) When neutral particles collide with the walls or the neutralizer plate, they are backscattered or desorbed after adsorption. As described in (iii), the history of ions is terminated when they hit the neutralizer plate. Ions are neutralized and re-injected when they collide with the walls.
- (v) The movement of ions or neutral particles are followed until they go out of the calculational model via the exits in the main plasma interface or the pumping duct whereby they are counted. The history of particles are also terminated if they remain in the calculational system even after a specified number of time steps.

A history of a particle begins from the step (ii) described above. The steps (ii) - (v) will be described in detail in the following.

(1) Neutral particle emission

Re-injected neutral particles were emitted uniformly from the part of the neutralizer plate in contact with the scrape-off layer. The emission energy and angle were determined by considering the particle and energy reflection coefficients $R_N(E)$ and $R_E(E)$, respectively⁶⁾.

$$R_N(E_0) = -0.237 \log_{10} \left(\frac{E_0}{E_L} \right) + 0.19, \quad (2)$$

$$R_E(E_0) = -0.22 \log_{10} \left(\frac{E_0}{E_L} \right) + 0.06, \quad (3)$$

where E_0 is the incident DT or He ion energy in keV and E_L for DT and He atoms incident on copper is 2.99 keV and 6.29 keV, respectively. As for E_0 , the ions were assumed to be accelerated by the sheath potential and have the energy equal to the electron temperature of the scrape-off layer T_b . Owing to the sheath potential, the normal incidence of the ions onto the neutralizer plate was assumed. Hence the fraction $R_N(E_0)$ of the re-injected neutral particles was assumed to be backscattered immediately with energy,

$$E_i = \frac{R_E(E_0)}{R_N(E_0)} \times E_0 \quad (4)$$

in the direction of cosine distribution. The rest of the re-injected neutrals (i.e. $1 - R_N(E_0)$ by the fraction) comes out after an adsorption-desorption process with the thermal energy of the neutralizer plate ~ 0.1 eV and the angular distribution also of cosine form. The DT particles are assumed to be re-injected with 0.1 eV in molecular state which dissociate immediately. Thus the neutral DT particles were assumed to possess 3 eV initially. Re-injected neutral particles move freely until they ionize, charge exchange, collide wall or go out of the calculational system through exits.

(2) Ionization and charge exchange

Ionization rate coefficients for DT particles were obtained from the formulation of R. L. Freeman and E. M. Jones⁷⁾ and those for He particles from W. Lotz⁸⁾. Charge exchange rate coefficients for DT particles formulated by A. C. Riviere⁹⁾ were used.

A neutral He particle ionizes in the scrape-off layer plasma if the ionization time τ_i is less than the given time interval, Δt , of the time step for the Monte Carlo calculation, and simultaneously, the value Δt is set equal to τ_i . If $\Delta t < \tau_i$, the value of Δt remains unchanged. The ionization time τ_i was randomly selected by an ionization probability function using uniform random numbers.

In the case of a neutral DT particle, it has the chance to charge exchange as well as ionize. Therefore it reacts with the scrape-off layer plasma if the collision time τ_c is less than Δt . Whether the reaction is charge exchange or ionization is determined according to the magnitudes of their reaction rate coefficients.

During the defined time interval of each step, the motion of ions is calculated in the background of free motion. The velocity of ions is changed by adding the acceleration term due to the pre-sheath field in the scrape-off layer. The momentum change due to random Coulomb scattering was calculated by generating normal random numbers. Ions diffuse with an anomalous type diffusion coefficients drawn by normal random numbers.

When a neutral DT particle charge exchanges, the motion of the newly created neutral particle is followed instead of the ionized particle which had been tracked previously. The newly created neutral particle is assumed to be generated from the point of charge exchange reaction with energy of the mean ion temperature in the scrape-off layer and the direction of motion was assumed to be random within the $Y = 0$ surface.

(3) Collision with the neutralizer plate and walls

A neutral particle collides with a wall and is reflected by one of the three assumed mechanisms.

When the angle of incidence θ (the angle between the direction of the particle before collision and the surface) is nearly 90° (i.e. $70^\circ \leq \theta \leq 90^\circ$), it is backscattered or desorbed after adsorption in the same manner as the initial emission described in (1). However, in this case, the value of E_L used in the particle and energy reflection coefficients of Eqs. (2) and (3) takes 2.61 keV and 5.51 keV for DT and He particles incident upon iron, respectively. A particle gone through trapping will be desorbed with energy 0.05 eV.

When $\theta < 70^\circ$, it is backscattered with energy two thirds of the incident energy. It is reflected specularly when θ is nearly 0 and as θ becomes larger the direction of re-emission becomes more of cosine distribution.

The collision of neutral particle with the neutralizer plate is also treated in the same manner as described above except for the changes in the values of E_L and the desorbed particle energy which is equal to the plate temperature.

When an ion reaches the wall it is neutralized. Besides losing electric charge, the re-emission mechanism is not different from the case of neutral particle collision. The history of an ion reaching the neutralizer plate is terminated and its score is kept.

(4) Particle history termination and accounting

Besides reaching the neutralizer plate in an ionized state, there are three other ways for a particle history to be terminated. The history of particles is terminated when they go out of the calculational model through either the exit in the main plasma interface or the pumping duct whereby they are counted. If a particle remains in the calculational volume even after a specified number of time steps, its history is terminated and counted.

3) Results and discussions

All the results of 20 cases are summarized in Table 3 together with the varied parameters. The calculated results are given in the last seven columns. The fractions of the particles which went out of the calculational model to the main plasma $f(\text{MP})$, to the pump $f(\text{pump})$, which returned to the neutralizer plate in ionized state $f(\text{NP})$, and which remained in the system $f(\text{float})$ after 2000 time steps (which corresponds to ~ 1 ms) are given separately. Numbers of ionization (R_{ion}) and charge exchange (R_{CX}) reactions per particle history are also given.

Assuming that the ionized particles returning to the neutralizer plate will be again re-injected in the same manner as it was originally generated, the ratio $f(\text{MP})/f(\text{pump})$ of the fraction of particles going back to the main plasma and that of going out to the pump will remain unchanged even if the history of those particles returning to the neutralizer plate in ionized state are followed until they eventually go out of the system. The ratio $f(\text{MP})/f(\text{pump})$ is given in the last column of Table 3. The fraction $f(\text{float})$ of particles which remain in the system after 2000 time steps is small enough to be neglected. The number of particle histories followed for each case is 10000 for most of the cases, the least being 5700. Therefore the statistical error is $\pm(0.01 \sim 0.013)$, although the fractions are given up to three digits below the decimal points.

The first two cases in Table 3 named STANDARD-DT and -He are the results for the DT and He particle simulations for the standard case. All the parameters are listed for the standard cases and only varied ones are given for the other cases. Initial energy E_0 in the standard case is 3.0 eV for the neutral particles generated after adsorption-desorption process and E_1 , determined by Eq. (4), for those being backscattered. In

the standard case, about 45 % of the DT goes back to the main plasma while 55 % are pumped out. Four times more He particles are pumped out than those He going back to the plasma. This means considerable He ash enrichment and hence exhaust may be achieved in this standard case.

When the average particle confinement time $\bar{\tau}_p$ is changed from 0.5 s to 0.15 s, and to 1.5 s, the temperature T_b and the mean density \bar{n}_b in the scrape-off layer change accordingly. As $\bar{\tau}_p$ is increased from 0.15 s to 1.5 s, the ratio $f(\text{MP})/f(\text{pump})$ for DT decreases slowly from 1.4 to 0.8 while that for He decreases drastically from 14 to 0.11. This means that the longer $\bar{\tau}_p$, resulting in lower \bar{n}_b is more favorable for ash He exhaust. This result is contrary to what had been expected and is now under investigation.

Increasing the divertor throat width d_t from 30 cm to 45 cm and then to 60 cm simply results in increase of $f(\text{MP})/f(\text{pump})$ from 0.83 to 4.3 for DT and 0.25 to 1.2 for He. Even with $d_t = 60$ cm, nearly half of He is exhausted while only 1/5 of DT is pumped out.

Pumping speed of 5×10^5 ℓ/s is assumed. The pumping speed is inversely proportional to $f(\text{MP})/f(\text{pump})$ for both DT and He.

Reducing the sheath-potential to 3/5 of the previous value results in more particles going back to the main plasma. The ratio $f(\text{MP})/f(\text{pump})$ increases only 15 % for DT but that for He becomes 3.5 times larger.

By generating all the particle with monoenergy (i.e. 250 eV, 3 eV and 0.1 eV), it is confirmed that most of the particles are re-injected after adsorption-desorption process in the neutralizer plate.

The density change of the neutral DT and He particles in the Z direction of the divertor channel for the standard case is shown in Fig. 3. Neutral He density decreases rapidly with the distance from the neutralizer plate due to the strong ionization. On the other hand the neutral DT decreases far less owing to the existence of charge exchange reactions.

Trajectories of some DT and He particles are plotted in Figs. 4 and 5. The charge exchange reactions are shown by changes of free motion direction in Fig. 4. Figure 5 shows that most of the generated He particles quickly ionizes and flows back to the neutralizer plate.

References

- 1) Y. Seki, et al., to be submitted to Nuclear Fusion (1980).
- 2) Y. Shimomura, K. Sako and K. Shinya, JAERI-M 8294 (1979).
- 3) H. Maeda and M. Okabayashi, Proc. Am. Phys. Soc. (1979).
- 4) S. Sengoku, M. Azumi, Y. Matsumoto, H. Maeda and Y. Shimomura, JAERI-M 7918 (1978).
- 5) DIVA Group, Nuclear Fusion, 18 (1978) 1619
- 6) K. Sone, private communication.
- 7) R. L. Freeman and E. M. Jones, CLM-R 137 (1974).
- 8) W. Lotz, Zeitschrift für Physik, 216 (1968) 241.
- 9) A. C. Riviere, Nucl. Fusion, 11 (1971) 363.

Table 1 Parameters of a reference reactor

Major radius	R	5	m
Minor radius	a/b	1.2/1.8	m
Plasma volume	V	200	m ³
Plasma surface area	S	300	m ²
Toroidal field	B _t	5	T
Plasma current	I _p	4.75	MA
Thermal out put	P _{th}	450	MW
α-particle out put	P _α	90	MW
Mean temperature	\bar{T}	10	keV
Mean fuel density	\bar{n}_f	1.2×10 ²⁰	m ⁻³
Mean ash density	\bar{n}_α	1.2×10 ¹⁹	m ⁻³
Energy confinement time	τ _E	1.5	s
Average particle confinement time	$\bar{\tau}_p$	0.5	s
Total particle loss flux	F _p	5.4×10 ²²	s ⁻¹
Ash flux to pump	F _{αo}	1.6×10 ²⁰	s ⁻¹
Burning duration	τ _B	200	s

Table 2 Parameters of scrape-off plasma in the divertor*

Scrape-off width	d	20 cm
Throat width	d _t	30 cm
Throat length	l _t	50 cm
Divertor efficiency	η _h , η _p	80 %
Plasma line density	n _b d	3×10 ¹³ cm ⁻²
Temperature	\bar{T}_b	250 eV
Area of neutralizer plates	S _n	90 m ²
Mean heat flux density to neutralizer plate	f _{qn}	40 W/cm ²
Maximum f _{qn}	f _{qnmax}	<120 W/cm ²
Vibration width of magnetic surface in divertor	d _v	10 cm

* Assuming $P_R + P_{cx} = 0.5 P_\alpha$

Table 3 Results of divertor parametric survey

Case name	Varied parameters							Fractional particle fate after 2000 times steps				Reaction per particle history		
	τ_p (s)	T_b (eV)	\bar{n}_b (cm^{-3})	d_z (cm)	f_{pump}	C_E	E_0 (eV)	Back to main plasma $f(NP)$	Exit to pump $f(pump)$	Ionized flow to n. plate $f(NP)$	Still floating $f(float)$	Ionization R_{ion}	Charge exchange R_{CX}	$\frac{f(NP)}{f(pump)}$
STANDARD-DT	0.5	250	1.7×10^{12}	30	0.9	0.5	$3.0, E_1$	0.201	0.242	0.557	0.0	0.603	0.523	0.83
STANDARD-He	0.5	250	1.7×10^{12}	30	0.9	0.5	$0.1, E_1$	0.008	0.032	0.961	0.0	0.973	-	0.25
TAU1-DT	0.15	115	8×10^{12}					0.319	0.229	0.452	0.0	0.615	0.462	1.4
TAU1-He	0.15	115	8×10^{12}					0.114	0.008	0.878	0.0	0.994	-	14.3
TAU2-DT	1.5	750	0.3×10^{12}					0.207	0.259	0.520	0.013	0.534	0.591	0.80
TAU2-He	1.5	750	0.3×10^{12}					0.011	0.101	0.886	0.002	0.897	-	0.11
WIDTH1-DT				45				0.383	0.165	0.448	0.004	0.499	0.480	2.3
WIDTH1-He				45				0.011	0.023	0.966	0.0	0.978	-	0.45
WIDTH2-DT				60				0.533	0.123	0.337	0.007	0.391	0.415	4.3
WIDTH2-He				60				0.021	0.018	0.961	0.0	0.978	-	1.2
PCMP1-DT					0.8			0.177	0.387	0.436	0.0	0.474	0.455	0.46
PCMP1-He					0.8			0.007	0.057	0.936	0.0	0.954	-	0.12
PCMP2-DT					0.95			0.223	0.142	0.635	0.001	0.684	0.556	1.6
PCMP2-He					0.95			0.007	0.017	0.976	0.0	0.985	-	0.4
EFIELD-DT						0.3		0.233	0.245	0.522	0.001	0.571	0.491	0.95
EFIELD-He						0.3		0.025	0.029	0.945	0.0	0.977	-	0.86
EIN1-DT							250	0.226	0.240	0.523	0.01	0.567	0.495	0.94
EIN1-He							250	0.075	0.058	0.867	0.0	0.922	-	1.3
EIN2-DT							3.0	0.209	0.234	0.556	0.001	0.605	0.520	0.89
EIN2-He							0.1	0.006	0.030	0.964	0.0	0.976	-	0.2

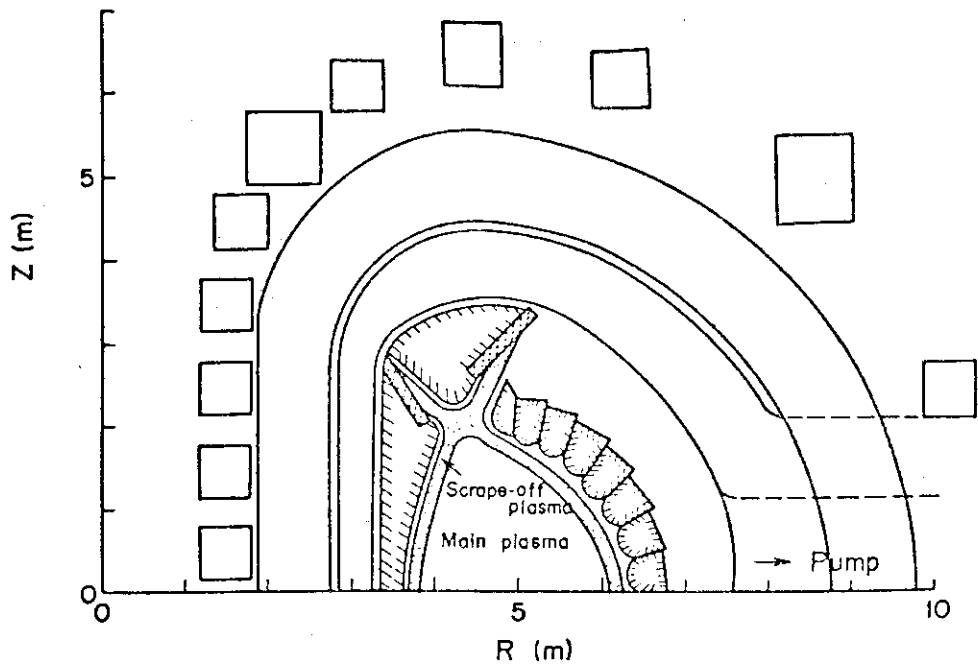


Fig. 1a Cross-sectional view of the reference reactor

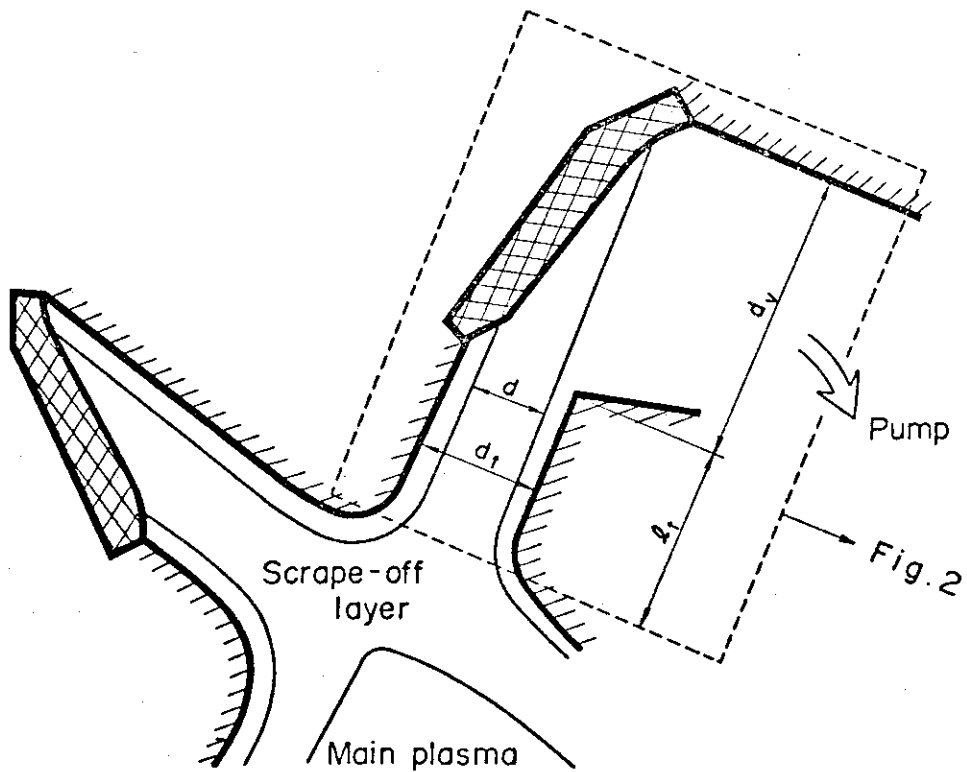


Fig. 1b A schematic drawing of a simple divertor, (the portions surrounded by the dashed lines correspond to Fig. 2.)

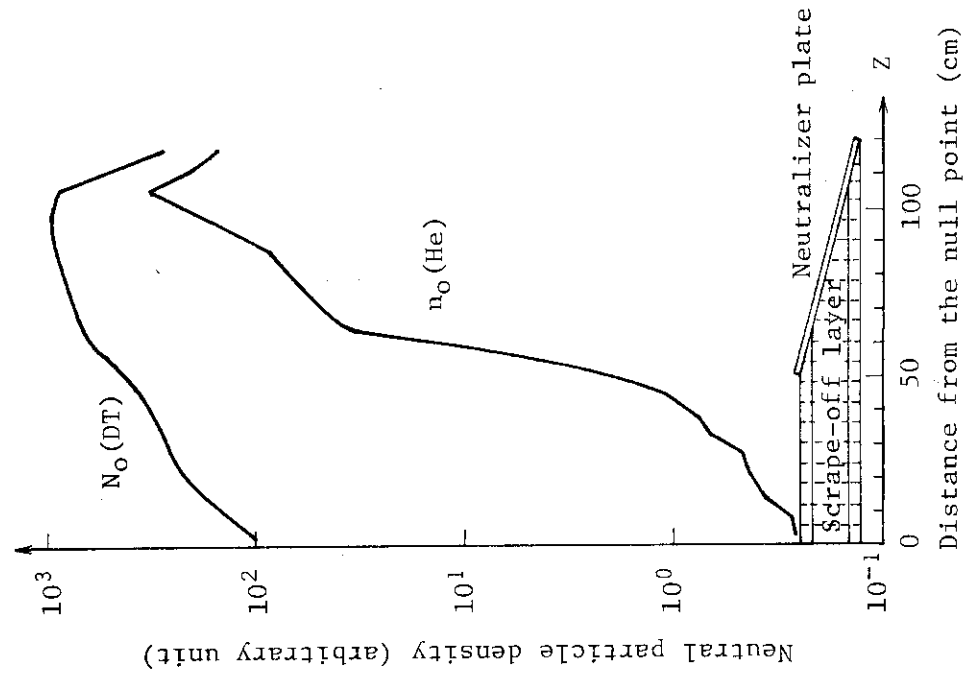


Fig. 3 Neutral particle density distribution along the divertor channel in the Z direction

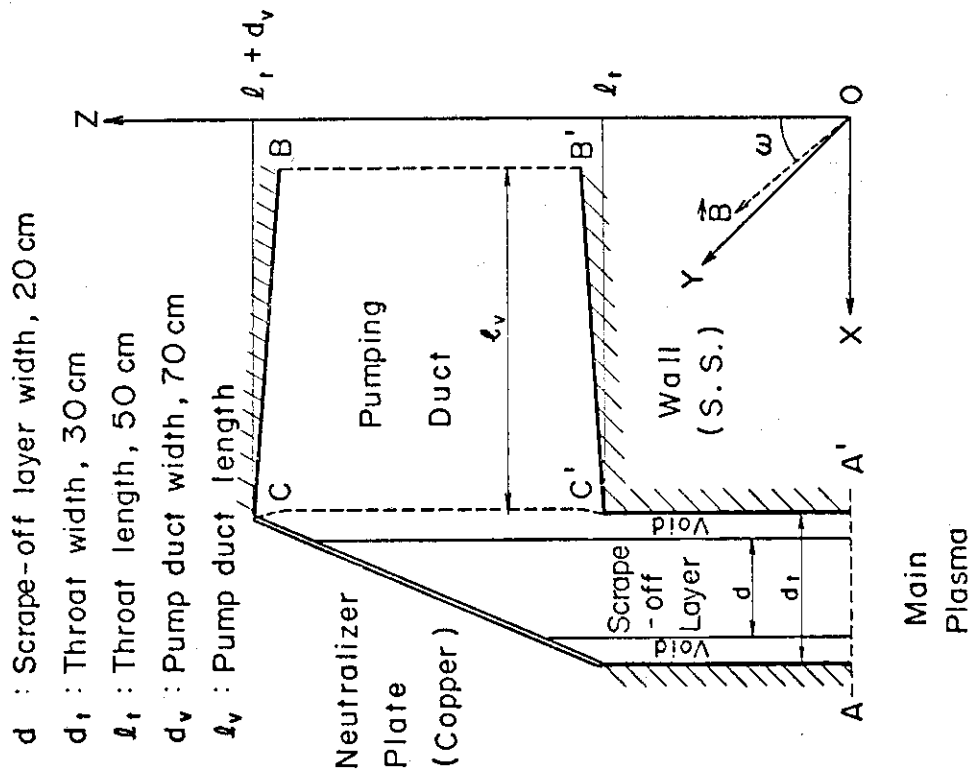


Fig. 2 Standard calculational model of the divertor

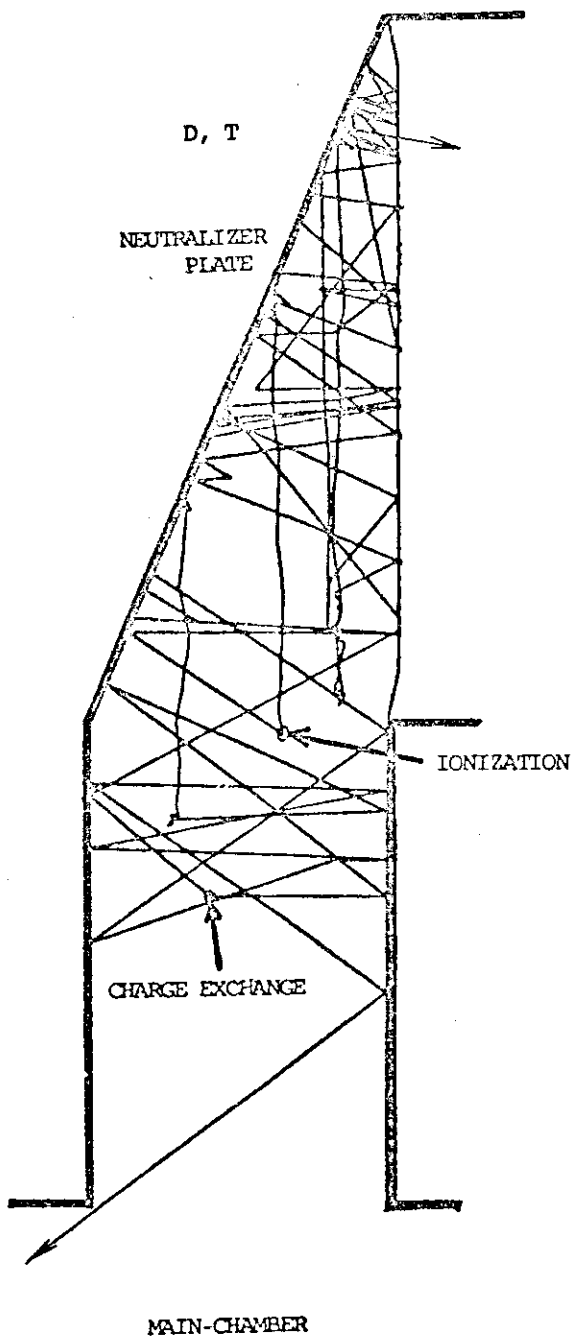


Fig. 4 Trajectories of DT particles in the standard case

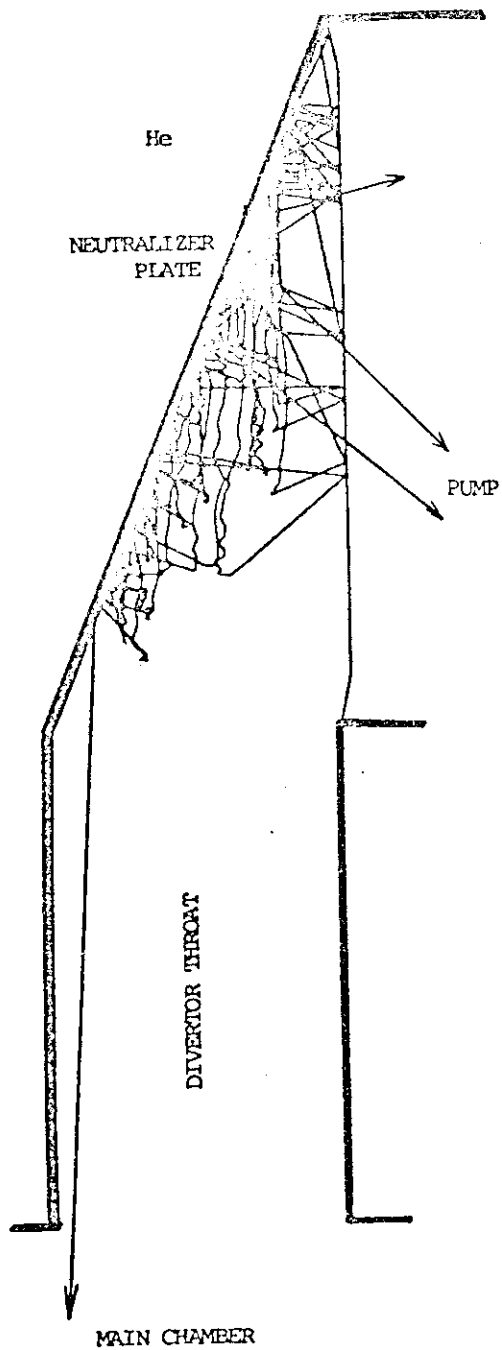


Fig. 5 Trajectories of He particles in the standard case

5.4 Impurity Production and Recycling in the Scrape-off Plasma of a Large Tokamak¹⁾

The process of heavy impurity recycling due to self sputtering including ionization, coulomb scattering and diffusion in a given plasma with and without a divertor is numerically investigated using a Monte-Carlo method. The permissible value for the boundary temperature in a future tokamak, e.g. JT-60 with a axisymmetric divertor and Mo first wall, is discussed.

1) Numerical model

- (i) Plasma parameters and configurations are shown in Figs. 1, 2 and Table 1.
- (ii) The velocity of ionized particles was rewritten by adding acceleration term due to the pre-sheath field in the scrape-off layer.
- (iii) The momentum change due to random coulomb scattering was calculated by generating a normal random number.
- (iv) Impurity ions diffuse with an anomalous type diffusion coefficient drawn by a normal random number.
- (v) When ions arrive at a limiter or a neutralizer plate, they sputter out neutral impurities of these materials. This is an impurity source for the next generation. The probability distribution for the sputtering event was normalized to the total sputtering yield S_0 .
- (vi) charged particles recombine when they reach the burial chambers or the wall, where they are assumed to be captured. Only sputtering produces impurities, i.e. no particle reflection at material surfaces was considered.
- (vii) We take

$$v_f = 0.3 C_s \text{ at } Z = \pm(\frac{1}{2} L_1 + L_2), \quad v_f = 0 \text{ at } Z = 0 \quad (1)$$

$$E = 0.5 T_{eb} / (\frac{1}{2} L_1 + L_2), \quad (2)$$

$$D_{\perp} = \frac{1}{2} D_{Bohm}, \quad (3)$$

where C_s is the sound velocity, D_{Bohm} the Bohm diffusion coefficient and T_{eb} the electron temperature of boundary plasma respectively.

(viii) In the calculation, average flow velocity, i.e. $\bar{v}_f = 0.15 C_s$, was employed. We set ion temperature and density to be equal to those of the electrons, respectively.

(ix) The thickness of the scrape-off layer $d = \sqrt{\tau_{//} D_{\perp}}$, where

$$\tau_{//} = \frac{\frac{1}{2} (L_1 + 2L_2)}{\bar{v}_f} = \frac{L_1 + 2L_2}{v_f} \quad (5)$$

(x) The plasma density in the scrape-off layer, \bar{n}_{eb} , is given from particle conservation: $\bar{n}_{eb} = \frac{1}{2} \frac{a}{d} \frac{\tau_{//}}{\tau_p} n_{e0}$, where τ_p , n_{e0} and a are the particle confinement time, the mean plasma density, the minor radius of the main plasma, respectively. Then the values d and \bar{n}_{eb} are given by a function of the temperature of the scrape-off plasma T_{eb} .

(xi) Sputtering yields were given by P. Sigmund²⁾. The values, however, are several times higher than experimental data on other heavy ions³⁾⁴⁾. Therefore, we divide Sigmund's sputtering yields S_0 by two for these calculations.

(xii) The incident energy of the sputtering impurity ions, E_I , is given as follows taking the sheath potential into account.

$$E_I = T_I + \alpha T_{eb} Z, \quad (6)$$

where T_I and Z are the temperature and the charge state of the impurity ions. The value α was taken to be 3.5 when the effect of the secondary electron emission was neglected and 0.99 when the emission was saturated, from sheath theory

$$\alpha = -\ln \left\{ \frac{\xi \sqrt{m/M}}{1 - \delta(T_e)} \right\}, \quad (7)$$

where ξ is the correction factor for the ratio of electron to ion saturation current, 1.5 - 3 for actual tokamaks, M and m the proton and electron mass, $\delta(T_e)$ the secondary electron emission coefficient.

(xiii) Ionization rate coefficient was calculated from E. Hinnov's simple representation⁵⁾.

(xiv) For the Monte-Carlo calculation presented here, the number of incident particle histories processed was sufficient at each energy to yield at least 10,000 sputtered atoms.

2) Computed results

Calculations show that the charge states increase continuously as the temperature of the scrape-off plasma increases when the divertor is off. However, when the divertor is on, the average charge state of molybdenum atoms is lowered due to a decrease of the number of impurity ions going to the hot plasma region, because the neutralizer plates are removed from the main plasma. By the same reason, impurity ions flow back to the neutralizer plate in a short time due to the particle flow and the pre-sheath field. This effect is enhanced when the boundary temperature increases. Therefore, the average charge states saturate at around five when divertor is on. Hence, a divertor lowers the incident energy E_I because of the relation given by Eq. (6), as shown in Fig. 3, and thus the number of sputtered atoms decreases. Because the neutralizer plates are well separated from the main plasma, the number of impurity ions N_Z which arrive at the neutralizer plates decreases, i.e., more impurity ions are captured in the burial chamber.

Decreasing E_I and N_Z leads to a lower impurity growth rate, as shown in Fig. 4 as compared with the case of divertor off. In the case with divertor, owing to the increase in the flow velocity and the diffusion coefficient, the number of impurity ions that annihilate at the burial chamber increases when the temperature increases. In addition to this, the sputtering yield saturates at energies above $E_I \sim 1$ keV, i.e. $T_{eb} \sim 60$ eV. Therefore, the growth rate decreases at temperatures above $T_{eb} = 60$ eV and is always less than unity, as shown in Fig. 4. The result shows that the maximum temperature is very low, 45 eV without the divertor, but is infinite with a divertor.

In this calculation, only self-sputtering was assumed and the effect of secondary electron emission was neglected. However, sputtering by protons and modifying the sheath potential cannot be neglected in a high temperature boundary plasma. To investigate these effects, calculation was repeated with the addition of proton-sputtering and the effect of secondary electron emission. The growth rate, including proton- and self-sputtering, $\gamma(\text{Mo}^+, \text{H}^+)$, is then given analytically as follows.

$$\gamma(\text{Mo}^+, \text{H}^+) = \left\{ 1 + \frac{1}{f} \frac{S_0(\text{H}^+)}{S_0(\text{Mo}^+)} \right\} \gamma(\text{Mo}^+), \quad (8)$$

where $f (= N_{\text{Mo}^+}/N_{\text{H}^+})$ is the fraction of molybdenum ions, $S_0(\text{H}^+)$ is the

proton sputtering yield extrapolated from Ref. 5) and taking into account of Eq. (7) in the calculation of $\gamma(\text{Mo}^+)$. This calculation gives a maximum in the temperature of the scrape-off plasma, without the divertor, of $80 \sim 140$ eV with $f = 0.1\%$ (allowable concentration for molybdenum in the main plasma). And $\gamma(\text{Mo}^+, \text{H}^+)$ is always less than 0.5 with the divertor.

Therefore, most of the energy loss from the main plasma must be converted into radiation or charge exchange losses to maintain equilibrium of the hot core and the cold boundary. If this conversion results in large adverse effects on the main plasma, the permissible maximum boundary temperature could be increased by some method, such as employing a material of low self-sputtering yield or a divertor.

References

- 1) S. Sengoku, et al., Nucl. Fusion, 19 (1979) 1327.
- 2) P. Sigmund, Phys. Review, 184 (1969) 383.
- 3) B.M.U. Schezer, R. Behrisch and J. Roth, Plasma Wall Interaction (Proc. Int. Symposium, Julich, 1976) Pergamon Press Oxford (1977) 353.
- 4) C.F. Barnet, J.A. Ray, E. Ricci, M.I. Wilker, E.W. McDaniel, E.W. Thomas and H.B. Gilbody, "Atomic Data for Controlled Fusion Research", Oak Ridge National Lab. Report, ORNL-5207, (1977) D.1.30.
- 5) E. Hinov, "Multiple Ionization in High Temperature Plasmas", Princeton Univ. Plasma Physics Lab. Report, MATT-777, (1970).

Table 1 Plasma parameters in JT-60

Main plasma		
Major radius	R	3 m
Minor radius	a	0.95 m
Length of the plasma sheet	L_{\perp}	30 m
Toroidal magnetic field	B_T	5 T
Plasma density	$n_{e0} = n_{i0}$	$7 \times 10^{13} \text{ cm}^{-3}$
Plasma temperature	$T_{e0} = T_{i0}$	7 keV
Effective ion charge	Z_{eff}	2.55
Scrape-off plasma assuming $T_{\text{eb}} = 50 \text{ eV}$ without a divertor		
Average plasma density	\bar{n}_{eb}	$3.19 \times 10^{12} \text{ cm}^{-3}$
Thickness of scrape-off layer	d	2.1 cm
Flow velocity	v_f	$2.13 \times 10^6 \text{ cm/sec}$
Perpendicular diffusion constant	D_{\perp}	$3.13 \times 10^3 \text{ cm}^2/\text{sec}$
Electric field	E	$1.67 \times 10^{-2} \text{ volts/cm}$

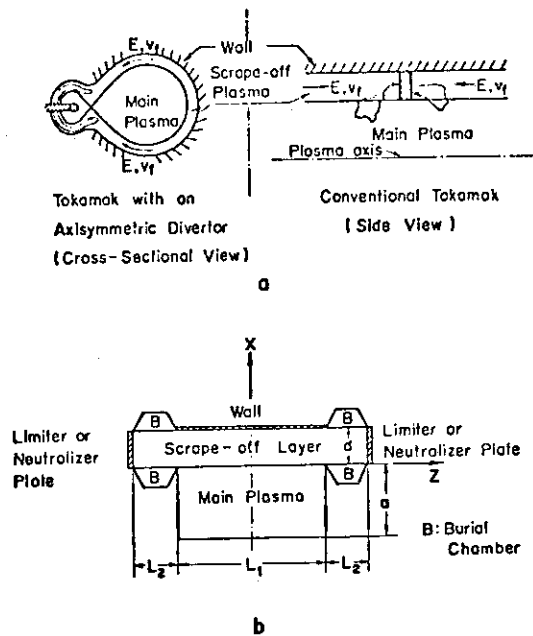


Fig. 1 Sheet model of a tokamak plasma with a divertor. Ordinate is taken in the direction of the thickness of the sheet and abscissa in the direction of magnetic field lines. The thickness of scrape-off plasma is denoted by d and main plasma by a , respectively. The length along the field line of the scrape-off plasma is $L=L_1+2L_2$ and of main plasma is L_1 , $L_2=0.001$ m and 5 m, when divertor is off and on, respectively.

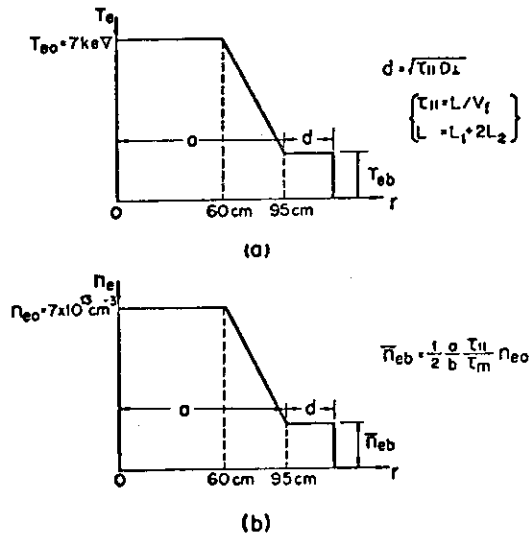


Fig. 2 Assumed profile of a) electron temperature and b) density. The electron temperature T_{e0} and density n_{e0} of main plasma and electron temperature of scrape-off plasma T_{eb} are given parameters. Both thickness d and electron density \bar{n}_{eb} of the scrape-off plasma are calculated from the above parameters.

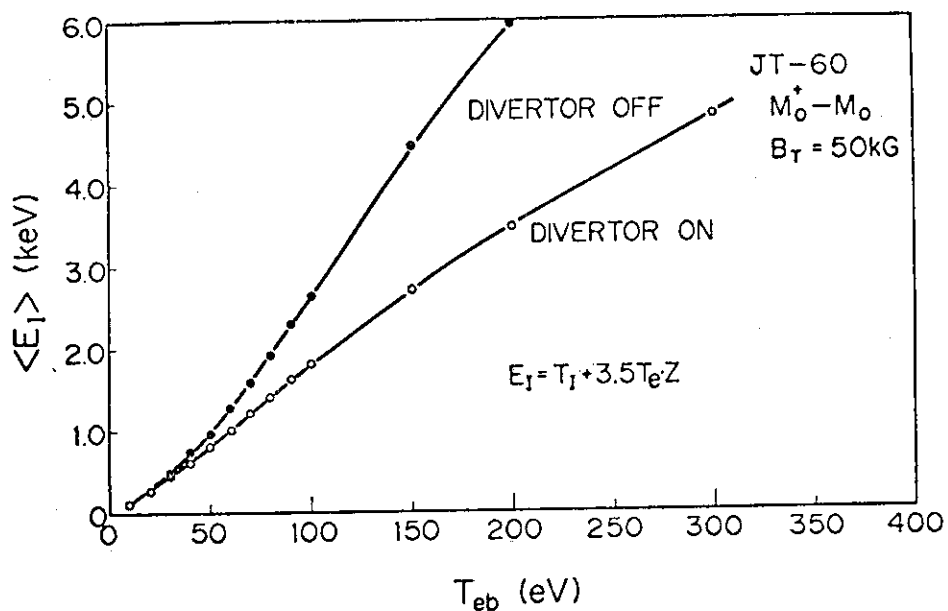


Fig. 3 Average sputtering energy $\langle E_I \rangle$ as a function of electron temperature of boundary plasma T_{eb} . Incident energy of sputtering is given by $E_I = T_I + 3.5 T_{eb} Z$, where T_I and Z are temperature and charge state of impurity ion, respectively. For instance, $\langle E_I \rangle = 824$ eV and $\langle Z \rangle = 4.4$ when $T_{eb} = 50$ eV without divertor.

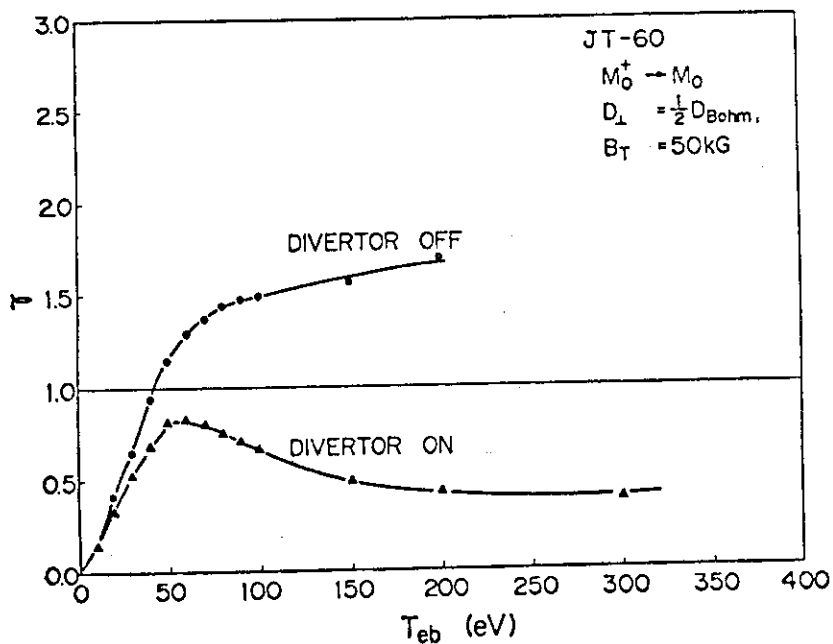


Fig. 4 Impurity growth rate γ v.s. electron temperature of boundary plasma with and without the divertor. The corresponding temperature of $\gamma = 1$ gives an equilibrium state.

6. NON-DIVERTOR CASE FOR IMPURITY CONTROL & ASH EXHAUST

6.1 "Wall Lapping Plasma" with Rotating Resonant Helical Islands and Mechanical Valves for Ash Exhaust

At present, we have no perfectly reliable method from both physical and technological viewpoints for impurity control and ash exhaust even in a machine with the divertor. We propose an alternative of the divertor called "Wall Lapping Plasma" which requires simple technology.

1) Resonant helical divertor

When we add a helical field (whose curve $nz - mr\theta = \text{const}$, with m, n integers and r, θ, z the usual cylindrical coordinates) by external helical coils, resonant islands are formed at the rational surface $q = m/n$. The above helical field is very small (e.g. 1 - 2% of the poloidal field) and a required current of helical coils is about 50 kAT at most. When we chose $q = 3$ ($m = 3, n = 1$) as the resonant surface, q at the plasma boundary will be about 2.5. The helical field reduces by $r^{m-1} = r^2$ to the plasma center and may not deteriorate hot core plasma.

Above configuration is used for a divertor called "Resonant Helical Divertor" proposed by F. Karger and K. Lackner³⁾. Helical divertor plates and helical shielding plates are installed inside the islands in this divertor. However, it seems complicated structure to install these helical plates inside the vacuum chamber, and it also seems dangerous that the heat load to the edge of the shielding plates will amount to over several kW/cm² which may cause severe evaporation, since besides the primary islands, islands of higher mode numbers are formed on the corresponding surfaces owing to the toroidal curvature and setting errors of poloidal and toroidal coils, so that these islands may overlap and the field lines are ergodized⁴⁾. More simple structure avoiding extremely large heat deposition can be imagined as follows.

2) "Wall Lapping Plasma" with rotating resonant helical islands

(1) Rotating resonant helical islands

In order to rotate these islands, two sets of helical coils are located and each current is changed alternately at 1 ~ 10 Hz. Consequently, the plasma surface contacting with the wall rotates along the

whole wall surface. Therefore, we can avoid the evaporation of the first wall by local heat deposition. Ergodization of the field lines can help above effect, since high heat conduction flows along the primary islands will be decreased.

(2) Ash exhaust by simple valves

In INTOR plasma, ash flow Γ_{α}^{+} to the wall is 8 - 16 times larger than that of ash source S_{α} when we assume $\tau_{\alpha} \sim \tau_p \sim \tau_E = 1 - 2$ s and allow 10 % ash accumulation of the plasma density. In this case, $\Gamma_{\alpha}^{+} = N_{\alpha}/\tau_{\alpha} = 1.2 - 2.4 \times 10^{21}$ particles/s and $S_{\alpha} = 1.5 \times 10^{20}$ particles/s, then $\Gamma_{\alpha}^{+}/S_{\alpha} = 8 - 16$. Where τ_{α} and N_{α} are particle confinement time and total number of α particles. Therefore, it is sufficient to exhaust 5 ~ 10 % of the recycling helium through the exhausting ports. By simple opening ports, of which area is 5 ~ 10 % of total area of vacuum vessel, we cannot expect to exhaust the same percents of recycling particles, since only small portion of recycling particles, which enter into the openings by chance, is exhausted. Therefore, we must install a sort of valve in front of the opening ports to guide 5 ~ 10 % of recycling particles into the ports.

This valve must meet the following requirements;

Collect 5 ~ 10 % of recycling particles, bear large heat load and easy to maintain or repair.

Similar valve for impurity control has been proposed by J.F. Shivell⁵⁾. However, the valve of Ref. 5) cannot bear high heat load in reactor-grade tokamaks. An example of the valve, which can meet these requirements, is shown in Fig. 2.

- (i) The valves stick out into the plasma to guide the recycling particles into the exhausting ports. Since B_r is much smaller than B_z , the shadow area of the valve is B_z/B_r times larger than that of the valve itself. For INTOR plasma, $B_z/B_r \sim 500$ and A_w (first wall surface area) ~ 300 m². Thus, about 20 valves, of which opening height is about 1 cm and opening area is 0.5 m², are shown to be sufficient to collect 5 ~ 10 % of recycling particles.
- (ii) Since the plasma contacts with whole wall surface almost uniformly by means of rotating the helical resonant islands, heat load of

the first wall can be suppressed well below to bearable level for evaporation (at most 30 W/cm² for INTOR plasma). However, when the valves are put perpendicularly to magnetic field lines, the heat load on the front edges is expected to be quite large.

In wall lapping plasma, the magnetic field line intersects with the first wall by radial component of the field line B_r . Thus, when the total heat flowing from the main plasma P_α is sustained uniformly by all of the first wall with the area A_W ,

$$w A_W \frac{B_r}{B_z} = P_\alpha \quad ,$$

For INTOR plasma, $B_r/B_z \sim 1/500$, $A_W \sim 300 \text{ m}^2$ and $P_\alpha \sim 90 \text{ MW}$ so that $w \sim 15 \text{ kW/cm}^2$. The edge of the valve perpendicular to the field line will suffer this heat load, which will cause serious evaporation. In order to mitigate the heat load to the edge, the valve is bent down slightly as shown in Fig. 2. As a result, the front edge does not suffer heat load directly. The heat load on the front surfaces of the valves is naturally equal to that on the first wall, i.e. under 30 W/cm², while that on the inner back surfaces, onto which guided particles flow and are neutralized, is under 150 - 300 W/cm². The heat load on the side edges of the valves w_v is most serious. This is given as $w_v \sim w\theta$ where the intersect angle of the valves with magnetic force lines $\theta = \theta_1 - \theta_2$, $\theta_1 \sim (B_\theta/B_z)$, and $\theta_2 \leq \frac{2}{3} \theta_1$ since setting accuracy of the valves is the order of θ_1 . Therefore w_v is several 100 W/cm² and it will give rapid damage of the valve edges. However, these valves are easily repaired owing to their structural simplicity, and this is one of the major advantages of these valves comparing with the divertor plates of the poloidal divertor.

Most of helium particles flow in the boundary layer along the toroidal field lines with the width H , which is given by

$$\frac{N_{\text{He}}}{\text{He}} = 2\pi\sqrt{abH}(n_{\text{He}})bv_s = A(n_{\text{He}})v_s \frac{B_r}{B_z} \quad .$$

Therefore the necessary valve height h is given by

$$h = \frac{H}{10} \frac{2\pi\sqrt{ab}}{abvN} = \frac{2\pi R}{10} \frac{B_r}{B_z} \frac{\pi\sqrt{ab}}{bvN} \sim 10^{-2} \text{ m} \quad .$$

Where we assume $\frac{B_r}{B_z} \sim \frac{1}{500}$, valve width $b_v = 0.1$ (m) and valve number $N = 20$. The total opening area of the valves $A_v = 2\ell_v hN = 0.5 \text{ m}^2$ where the valve length $\ell_v = 1.2$ m.

Plasma particles and helium are not ionized in the plasma flowing into the backsides of the valves. Therefore we can simply calculate the neutral flows such as direct leakage flows Γ_ℓ through the valve opening and pumped flows Γ_v through the ports.

$$\Gamma_\ell = \frac{1}{4} n_0 v_0 A_v ,$$

$$\Gamma_v = n_0 S_p \sim \frac{1}{10} \frac{N_p}{\tau_p} = 2.5 \times 10^{21} \text{ (p/s)}$$

where we assume $n_0 = n_D^0 + n_T^0 + n_{He}^0$, $n_{He}^0 / (n_D^0 + n_T^0) \sim 0.1$, the particle confinement time $\tau_p = 1\text{S}$, $v_0 \sim 10^3/\text{S}$ and S_p is the pumping speed at the port inlet (the pumping speed at the outlet should be larger than S_p by several factor). Therefore $\Gamma_v \geq \Gamma_\ell$ when $S_p \geq 10^2 \text{ m}^3/\text{S}$. We employ $S_p = 5 \times 10^2 \text{ m}^3/\text{S}$ and neutral density in the port $n_0 \sim 5 \times 10^{18} \text{ p/m}^3$. Neutral backflow does not prevent the inflow of the plasma particles, since

$$\Gamma_\ell \ll n_b v_s A_v \text{ where the boundary density } n_b = \frac{2\bar{n}}{\tau_p} \frac{1}{v_s} \frac{B_z}{B_r} = 3 \sim 5 \times 10^{18} \text{ (p/m}^3\text{) assuming the boundary temperature } T_b = 10^2 \sim 10^3 \text{ eV.}$$

The test of this concept is left open to a future experiment.

References

- 1) T. Tazima, M. Sugihara, JAERI-M 8390 (1979).
- 2) F. Karger, et al., Plasma Physics and Controlled Nuclear Fusion Research, Proc. 5th Int. Conf., Tokyo (1974), IAEA, Vienna (1975) 207.
- 3) F. Karger, K. Lackner, Phys. Letters 13 (1977) 385.
- 4) W. Feneberg, Proc. 8th Europ. Conf. on Controlled Fusion and Plasma Physics, Prague, 1 (1977) 4.
- 5) J.F. Shivell, PPPL-1342 (1977).

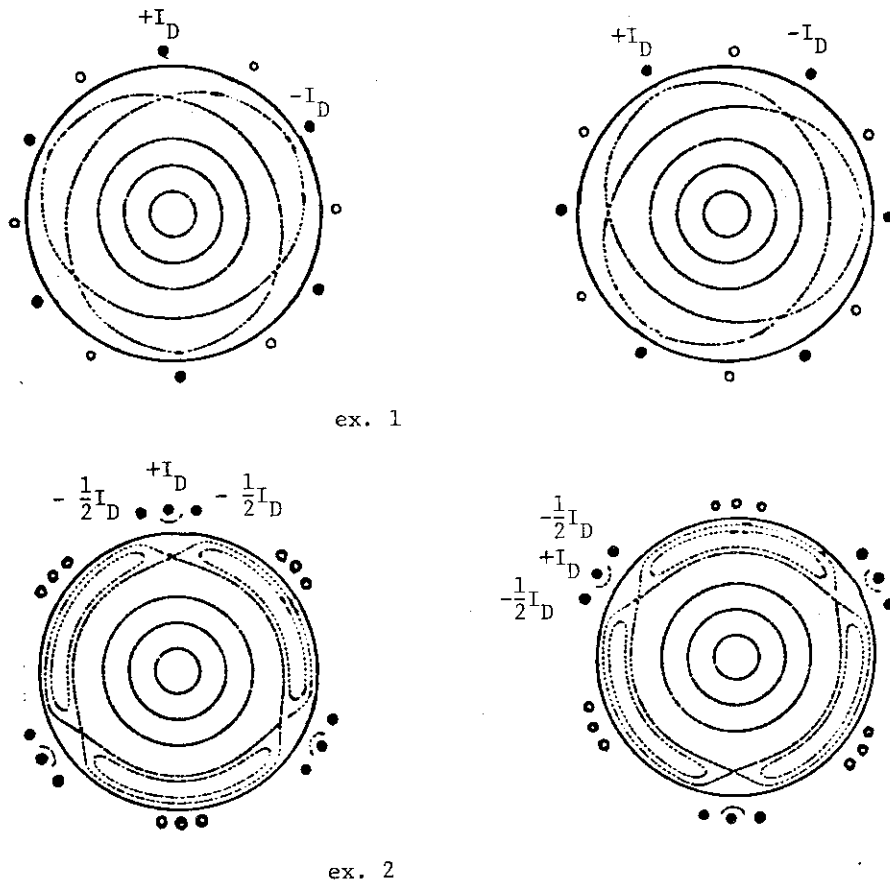


Fig. 1 Schematic pictures of the crosssection of a helical island with resonance at $q=3^3$. Two sets of helical coil currents I_D are quickly changed alternately.

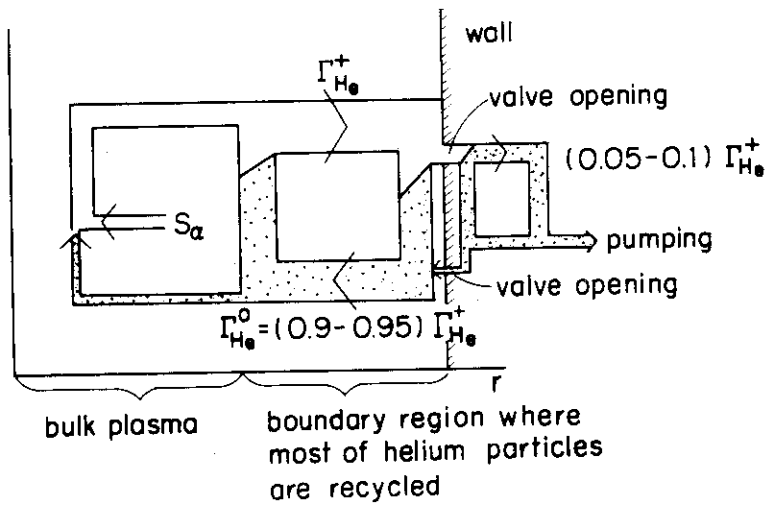


Fig. 2 (a) Schematic picture of a particle recycling and exhaust

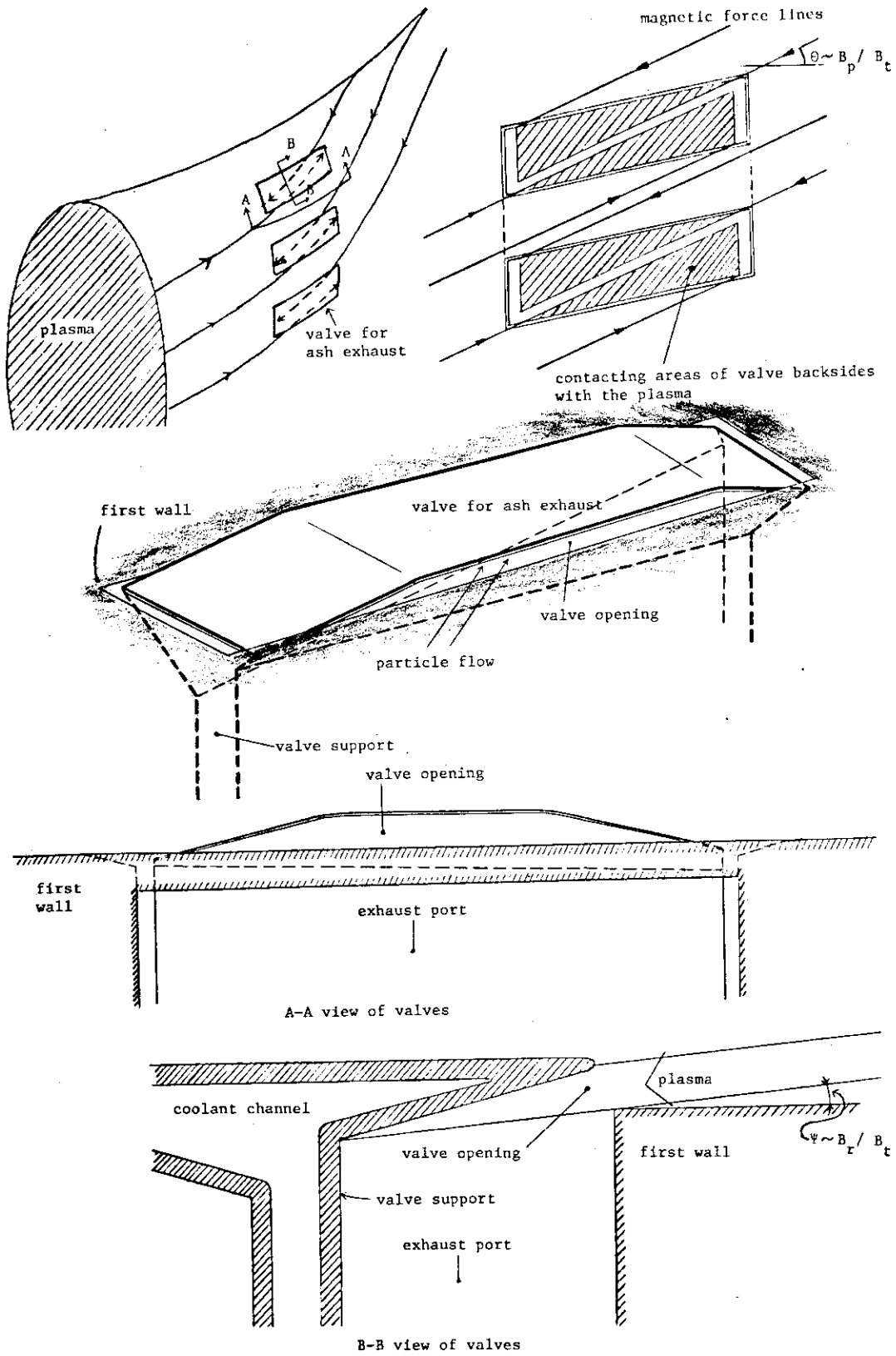


Fig. 2 (b) Schematic picture of valve for ash exhaust

7. FUELING

Fueling with a controllable mixture of deuterium and tritium will be needed in the density-rise phase of the startup. Refueling with an equal mixture of deuterium and tritium will be needed to replenish the ions consumed by the fusion reactions, and also to replace fuel exhausted through the divertor.

Gas puffing is the simplest method of fueling and refueling. However, there are uncertainties whether it will work satisfactorily for rapid fueling in the density-rise phase in a divertor case, because of the shielding action of the scrape-off layer and the pumping action of the divertor. Pellet injection will provide superior flexibility over the deposition profile. In particular, pellet injection might also help to obtain an adequate target density for neutral beam injection or certain types of RF heating in the joule heating phase, where the present empirical scaling laws for the mean achievable density¹⁾²⁾ in joule-heated plasma with gas puffing predicts a mean attainable density of $\bar{n} \sim (1\sim 3) \times 10^{19}/\text{m}^3$ in INTOR (Fig. 1).

Following problems are predicted;

- (i) How should fuel be supplied during additional heating phase to attain a required density?
- (ii) Can fuel be supplied to the inner hot core without strong skin distribution of the density in the cases of divertor and non-divertor?
- (iii) Will sputtering of first wall by charge exchange neutrals during fueling cause serious plasma contamination or not?

7.1 Gas Puffing

Figure 2 shows an example computed by one dimensional simulation code where tritium is supplied by gas puffing for 5s. Puffing rate of tritium is nearly equal to that of deuterium supplied by NBI. Deuterium is well distributed because of sufficient supply by NBI in the central region. On the other hand, tritium distribution is strong skin one, since the most of tritium neutrals is ionized in the boundary region and charge exchange neutrals can not penetrate deeply into the inner hot core because of large plasma radius. Such strong skin distribution maintains for several seconds even after gas puffing and causes the skin heating of

NBI, and small tritium density in the hot core decreases fusion power production. Above results strongly depends on diffusion model of the plasma. We employ in the calculation $D = \chi_e/30$ and $\chi_e = 5 \times 10^{19}/n_e$, since guiding model such as $D = \chi_e/4$ gives extremely short particle confinement time τ_p (e.g. $\tau_p \leq 0.1\tau_E$). Since recent experiments show that $\tau_p \sim \tau_E$ is most likely, we employ above a set of transport coefficients. However, this model cannot suppress such skin distributions because of long τ_p above 1s.

In any case guiding diffusion model gives a very flat distribution of the density. However, experimental density distributions are peaked ones both in small and medium size tokamaks. Guiding model seems hardly to explain such peaked distributions. Other diffusion models such as strong inward flow (e.g. Ware pinch velocity) or large anomalous diffusion near the boundary region may be necessary to be investigated.

7.2 Pellet Injection

1) Concept of model

Parks et al.³⁾ proposed to following model in good agreement with the ORMAK⁴⁾, ISX-A⁵⁾ pellet injection experiment. Plasma electrons reach the pellet surface, therefore, the relatively cold and dense hydrogen gas (neutral) formed there forms the cloud of hydrogen molecules around the pellet, it expands toward the near-vacuum conditions of the background plasma, so, this cloud slows down plasma electrons and reduces energy flux to pellet and therefore lifetime of pellet becomes long. Energy of plasma electrons are given to ablation cloud as thermal energy, the part becomes the kinetic energy of ablation cloud and the rest becomes the source of cloud temperature.

2) Pellet velocity scaling law

The ablation process is dominated by the rate at which energy is delivered to the pellet surface by incident plasma electrons. We do not consider the attenuation of the beam intensity by elastic scattering, but there includes the degradation of the thermal energy. Following Parks et al.³⁾, the evaporation process is regulated by a set of conservation equations, one of which is the equation that the flow of material crossing the pellet surface is balanced by the efflux of gas away from the interface.

To complete the physical description of the ablation process, two additional relationships are required: (1) an energy balance at the solid interface which equates the incoming heat flux to the energy requirement for the solid-to-gaseous phase change and (2) a relationship between the plasma heat flux (electrons) external to the gas cloud and the degraded heat flux at the pellet surface. Following Milora et al.⁶⁾, the simple velocity scaling law is given by

$$U \sim 1.87 \times 10^{-13} \frac{a}{M^{1/3} r_p^{5/3}} \bar{n}_e^{1/3} \bar{T}_e^{1.7} \left(\frac{\ell}{a}\right)^3$$

where, a , M , r_p , n_e , T_e and ℓ represent plasma minor radius in m, molecular weight of the fuel in a.m.u., initial pellet radius in m, plasma density in m^{-3} , plasma temperature in eV and radial position at which the pellet vanishes, respectively. From this formula, the calculated penetration depth of pellet in INTOR is shown in Fig. 3.

Since a technologically reachable velocity of pellets might be slower than 5×10^3 m/s, we can only expect shallow injection. Therefore there is no large difference between gas puffing and pellet injection for fueling. In any case, tokamak plasmas can not be free from neutrals which will inevitably lead to an outflux of charge-exchange neutrals. These neutrals will bombard and sputter the first wall.

References

- 1) S. Konoshima, et al., *J. Nuclear Materials* 76 & 77 (1979) 581.
- 2) L.A. Berry, et al., *Proc. 6th Int. Conf. Plasma Physics and Controlled Nuclear Fusion Research, Berchtesgaden* (1976) 1, IAEA, Vienna (1977) 49.
- 3) P.B. Parks, et al., *Nuclear Fusion* 17 (1977) 539.
- 4) C.A. Foster, et al., *Nuclear Fusion* 17 (1977) 1067.
- 5) S.L. Milora, et al., *Phys. Rev. Letters* 42 (1979) 97.
- 6) S.L. Milora, et al., *IEEE Trans. on Plasma Sci.* PS-6 (1978) 578.

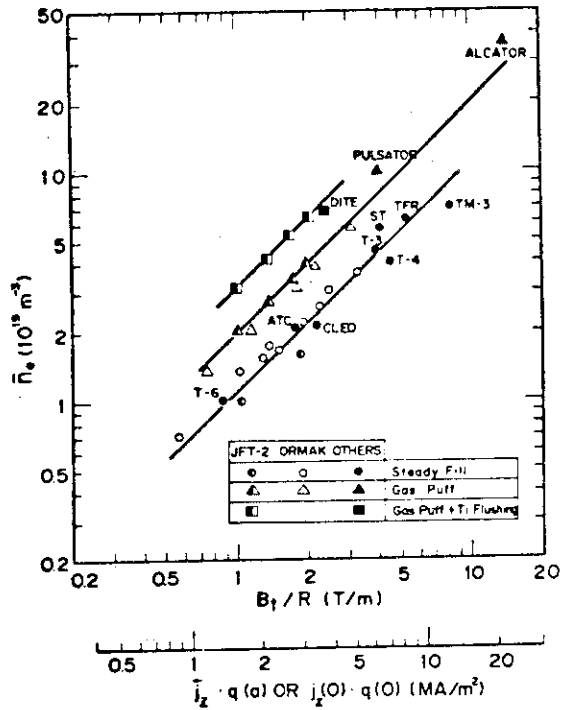


Fig. 1

Scaling law of mean electron densities. B_t : toroidal magnetic field, R : major radius, j_z : toroidal plasma current density, q : safety factor.

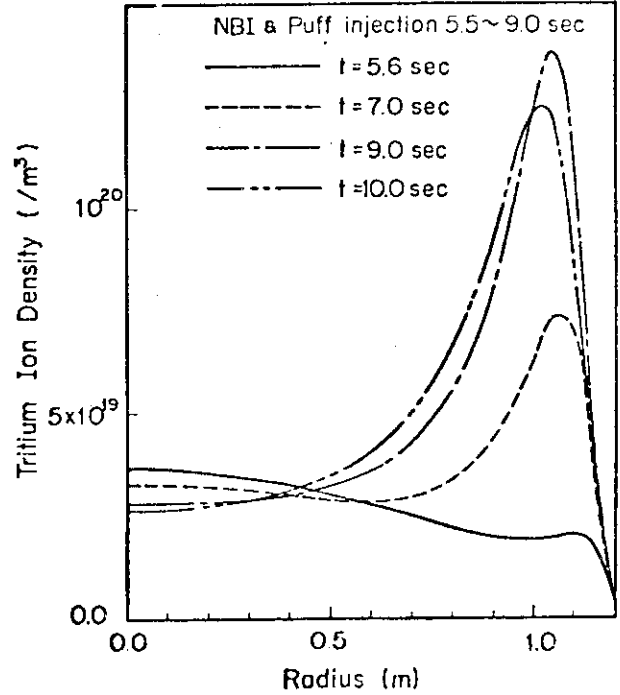
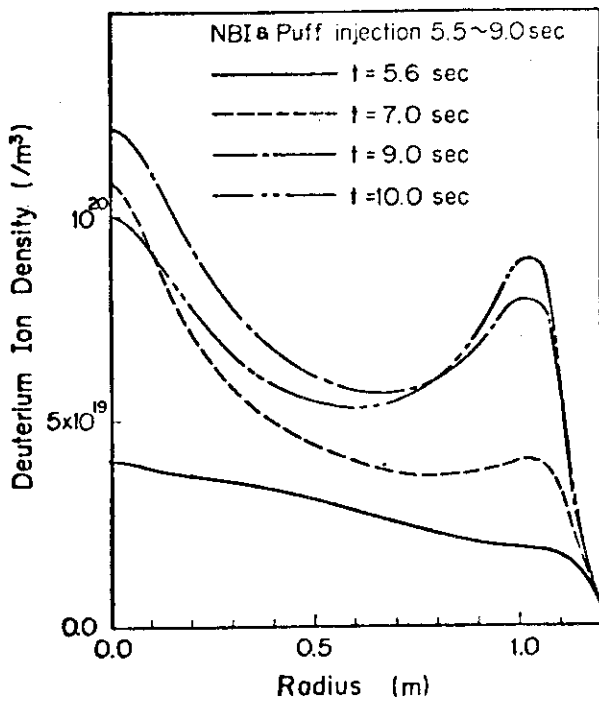


Fig. 2 (a) Time evolution of deuterium density of Case II with 70 MW injection.

Fig. 2 (b) Time evolution of tritium density of Case II with 70 MW injection.

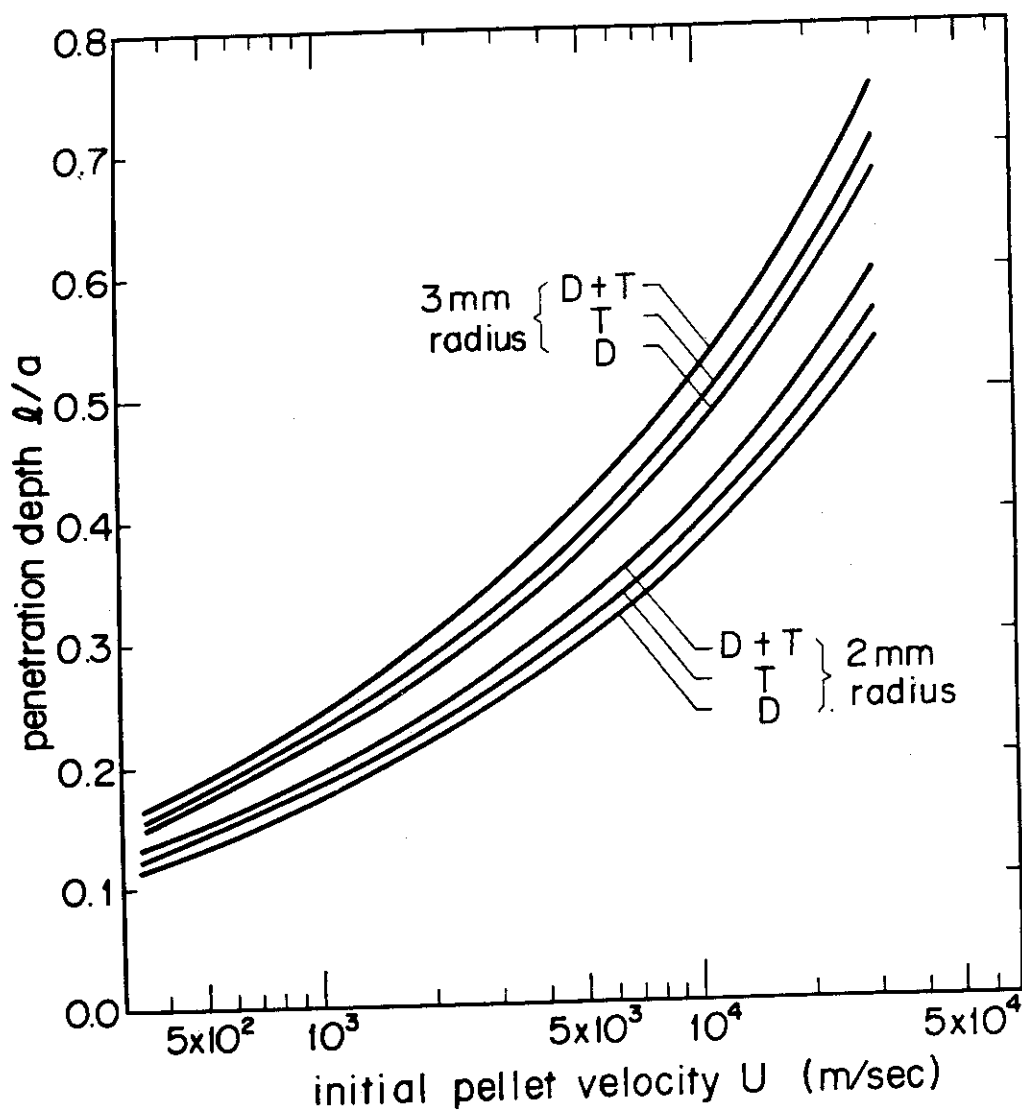


Fig. 3 Penetration depth of pellet injection in a case of mean density: $1.2 \times 10^{20}/\text{m}^3$, mean temperature: 10 keV and plasma radius: 1.2 m assuming parabolic distributions of the density and temperature.

8. DATA BASE ON SURFACE EFFECTS

8.1 Surface Effects Related to Impurity Production

1) General descriptions

- (i) impurity production from first wall material
 - Sputtering by plasma particles (H, D, T, He, etc) including physical and chemical sputtering.
 - Sputtering by light impurities (O, C, etc).
 - Self-sputtering.
 - Blistering including grain ejection and anomalous erosion.
 - Evaporation by unipolar arcs, etc.
- (ii) impurity production by desorption of adsorbed impurities on the first wall
 - Thermal desorption.
 - Ion induced desorption.
 - Electron impact desorption.
 - Photon induced desorption
- (iii) important parameters affecting the impurity production processes
 - Incident energy.
 - Angle of incidence.
 - Total fluence.
 - Incident flux.
 - Surface structure.
 - Surface cleanliness.

2) Data base

- For 1) (i), self-sputtering is under investigation in JAERI. There are no data for self-sputtering and evaporation by unipolar arcs.
 - For 1) (ii), these data are obtained in connection with surface cleaning except photon induced desorption. They are not compiled here.
 - Hereafter, we compile only the data base on sputtering and blistering.
- (i) sputtering
- Sputtering yield is defined as the number of the removed atoms (or molecules) per incident particle.

- Sputtering process is divided into two kinds: physical sputtering is caused by an atomic collision cascade, and chemical sputtering is due to chemical reactions between incident particles and wall material.
- Physical sputtering does not depend on wall temperature, but chemical sputtering strongly depends on it.
- Physical sputtering has a strong dependence on the angle of incidence with respect to the surface normal of the wall. Generally, it is minimized for the normal incidence, and it increases with increasing angle of incidence.
- Angular distribution of sputtered atoms is strongly dependent on energy, angle of incidence and wall microstructure (e.g. grain size). The more forward emission occurs for the lower energy, the larger angle of incidence and the smaller grain size.
- Physical sputtering yield is reduced by a factor of 20 to 30 by the use of honeycomb walls.
- Chemical sputtering yield data have been obtained for low Z materials as pyrolytic graphite and SiC. Chemical sputtering for other low Z materials as B₄C, TiB₂, TiN, Si₃N₄, etc is under investigation at JAERI.

(ii) blistering

- Compilation on blistering is made in the separate page.

8.2 Surface Effects Related to Particle Recycling

1) General descriptions

The following phenomena are involved.

- Reflection/backscattering.
- Re-emission including ion induced desorption, thermal desorption and chemical sputtering.
- Trapping.

Important parameters affecting the effects are the same as those in 1).

2) Data base

- A very few data have been produced in Japan.
- For reflection/backscattering from wall materials, we compile only energy reflection coefficient by hydrogens in the energy range of 10 - 30 keV in connection with neutral beam injection (NBI).

- For re-emission, it is under investigation at JAERI in the hydrogen energy range of 0.1 to 6 keV. Ion induced desorption in connection with NBI is also under investigation at JAERI. We compile only the data on the fluence dependence during bombardment of Mo with 100 keV He⁺ and pyrolytic graphite with 200 keV H₂⁺.
- For trapping, we compile only the data on the depth profile of 12 keV H₃⁺ implanted into Mo, and 2 keV He⁺ implanted into Mo.

References

- 1) H. Ohtsuka, et al., J. Nucl. Mater., 76 & 77 (1978) 188.
- 2) M. Mohri, et al., Proc. Fusion Reactor Materials Conf., Miami, 1979 (to be published).
- 3) T. Abe, et al., J. Nucl. Sci. Technol., 15 (1978) 471.
- 4) R. Yamada, et al., J. Nucl. Mater. (in press).
- 5) K. Sone, et al., Proc. Intern. Symp. Plasma Wall Interaction, Julich 1976 (Pergamon Press, 1977) p.323.
- 6) M. Mohri, et al., J. Nucl. Mater., 75 (1978) 309.
- 7) T. Yamashina, et al., J. Nucl. Mater., 76 & 77 (1978) 202.
- 8) R. Yamada, et al., J. Nucl. Mater. (in press).
- 9) S. Tanaka, et al., Japan. J. Appl. Phys., 17 (1978) 183.
- 10) K. Sone, et al., J. Nucl. Mater., 76 & 77 (1978) 240.
- 11) K. Sone, et al., (to be published).
- 12) S. Okuda, et al., Japan. J. Appl. Phys., 18 (1979) 465.

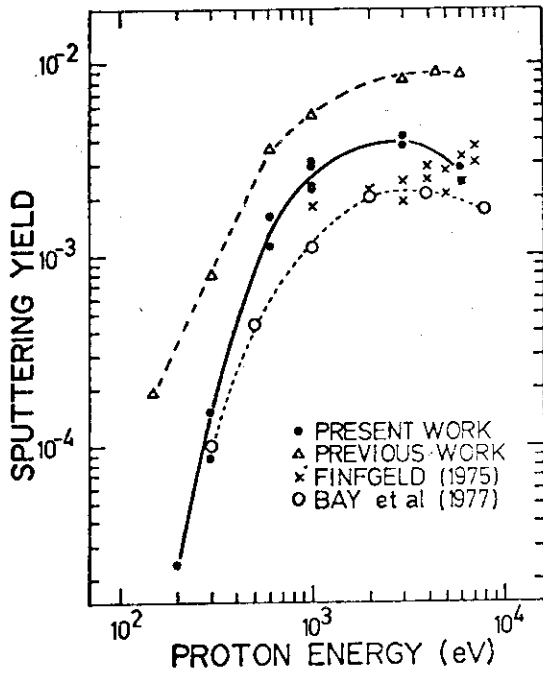
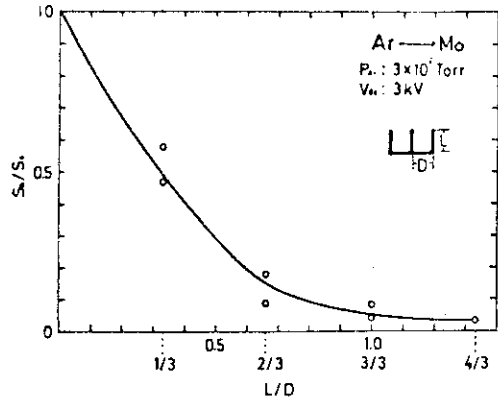
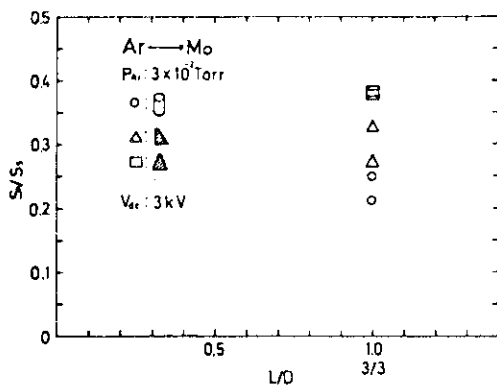


Fig. 1 Sputtering yield of molybdenum by protons as a function of energy.¹⁾



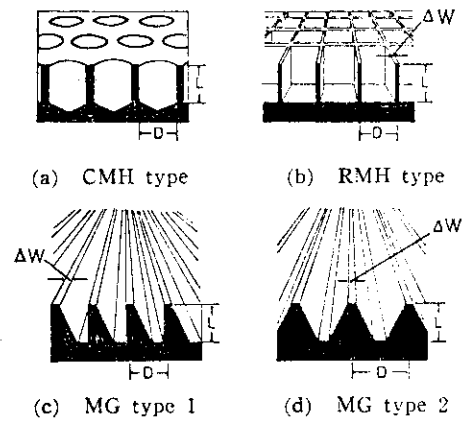
Argon discharge pressure and applied d.c. voltage are 3×10^{-2} Torr and 3 kV, respectively.

Fig. 2 Effective sputtering ratio S_h/S_s by Ar ion bombardment for RMH type structure as a function of L/D ³⁾



Argon discharge pressure and applied d.c. voltage are 3×10^{-2} Torr and 3 kV, respectively.

Fig. 3 Effective sputtering ratio S_h/S_s by Ar ion bombardment for CMH and MG type structures at $L/D=3/3$ ³⁾



Schematic representation of surface of various honeycomb structures

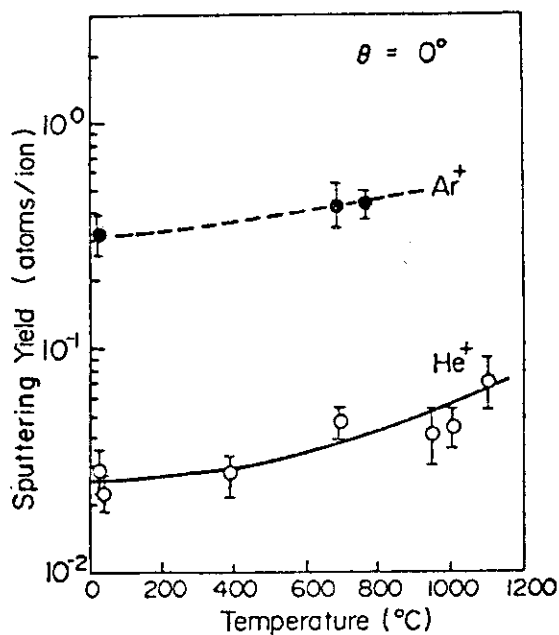
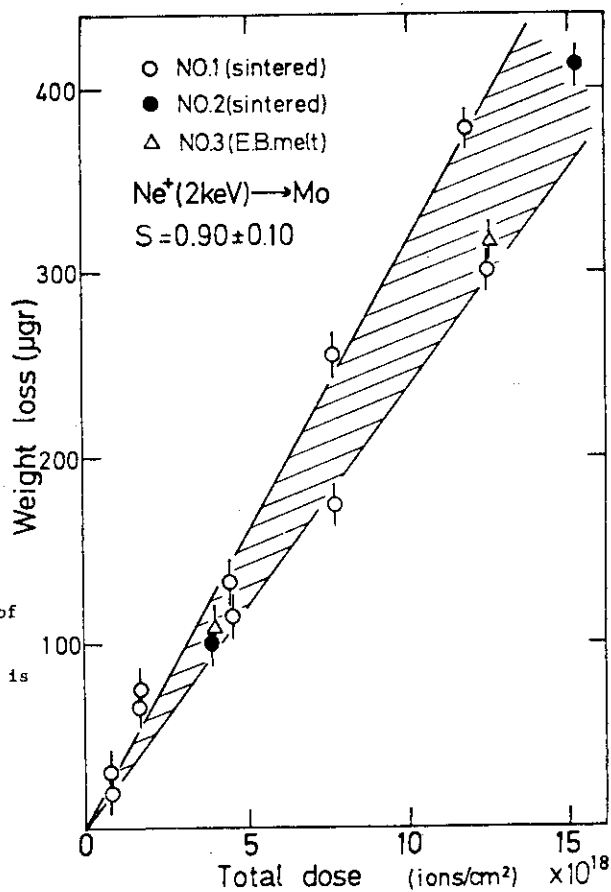


Fig.4 Variation of sputtering yield with target temperature for 10 keV helium and argon ions on silicon carbide. θ is the angle of incidence.²⁾

	No.1	No.2	No.3
	sintered	sintered	E.B.melt
	rolled	rolled	rolled
	1000°C 10min annealed	as received	as received
Mo	99.96 %	99.96 %	99.96 %
W	200 ppm	200 ppm	150 ppm
Fe	50	40	2
Al	10	6	2
Si	5	15	88
C	15	7	40
N	5	5	12
O	20	17	8

Fig.5 Measured weight loss by sputtering as a function of total dose of 2 keV Ne^+ ions incident on Mo samples. Characterization of three different samples No.1 to No.3 is tabulated above. Microstructural effect and dose effect are not observed within an accuracy of 10 %.⁴⁾



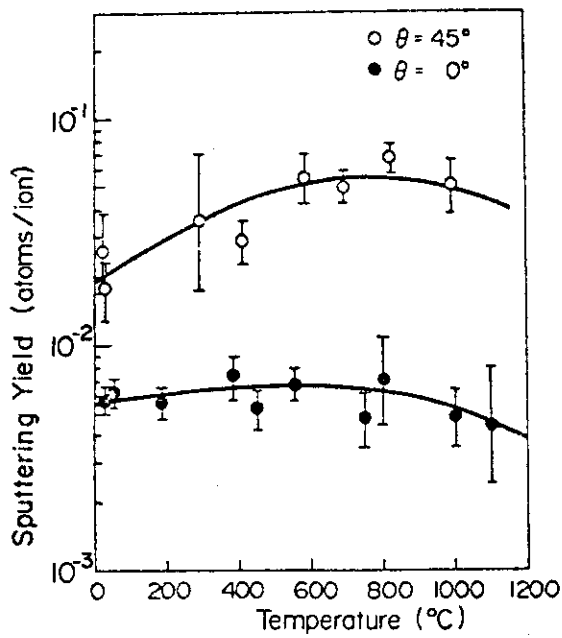


Fig. 6 Variation of sputtering yield with target temperature for 10 keV hydrogen ions on silicon carbide. θ is the angle of incidence.²⁾

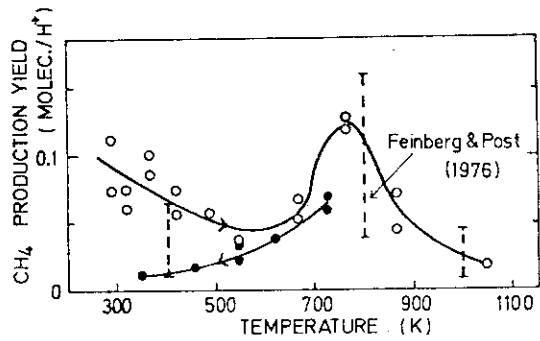


Fig. 7 Experimental data of proton chemical sputtering (methane production) yield as a function of target temperature. Proton energy: 1 keV. Experimental data by Feinberg and Post are also shown.⁵⁾

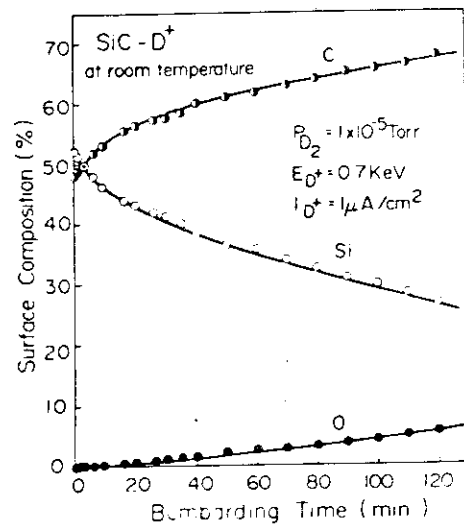


Fig. 9 The variation of surface composition of clean SiC during deuteron sputtering at room temperature.⁷⁾

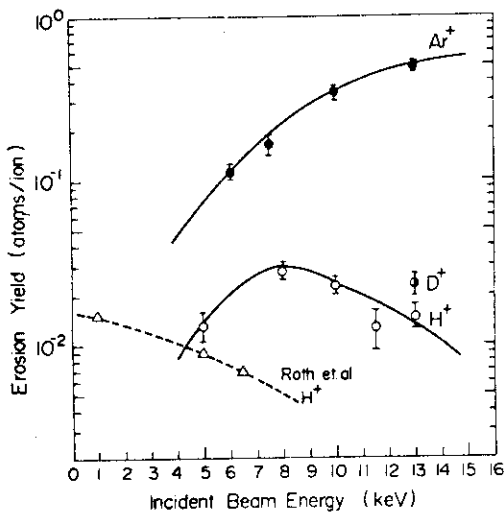


Fig. 8 Erosion yields as a function of incident beam energy at 45° incidence, obtained from the volume loss of silicon carbide surface sputtered by Ar^+ , H^+ and D^+ . Data of Roth et al. are plotted.⁶⁾

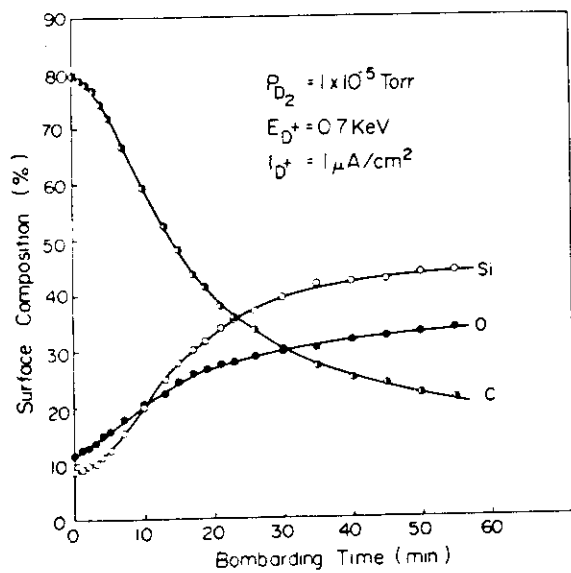


Fig. 10 The variation of surface composition of SiC during deuteron sputtering when the oxide exists on the surface.⁷⁾

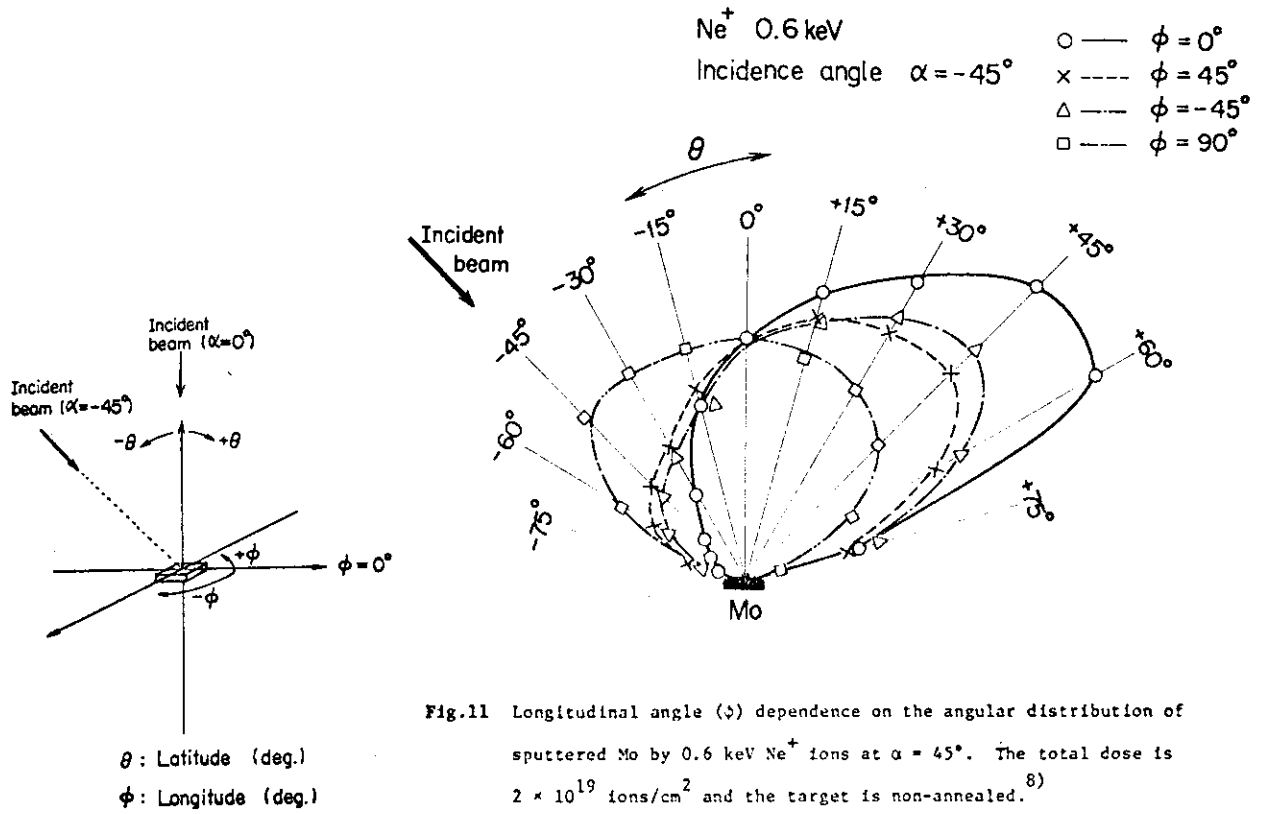


Fig.11 Longitudinal angle (ϕ) dependence on the angular distribution of sputtered Mo by 0.6 keV Ne⁺ ions at $\alpha = 45^\circ$. The total dose is 2×10^{19} ions/cm² and the target is non-annealed.⁸⁾

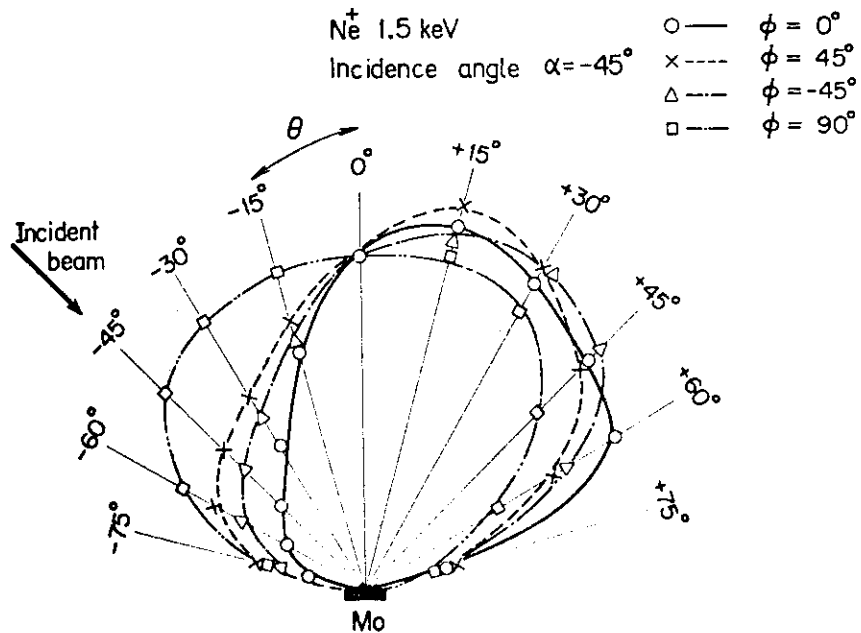


Fig.12 Longitudinal angle (ϕ) dependence on the angular distribution of sputtered Mo by 1.5 keV Ne⁺ ions at $\alpha = 45^\circ$. The total dose is 2×10^{19} ions/cm² and the target is non-annealed.⁸⁾

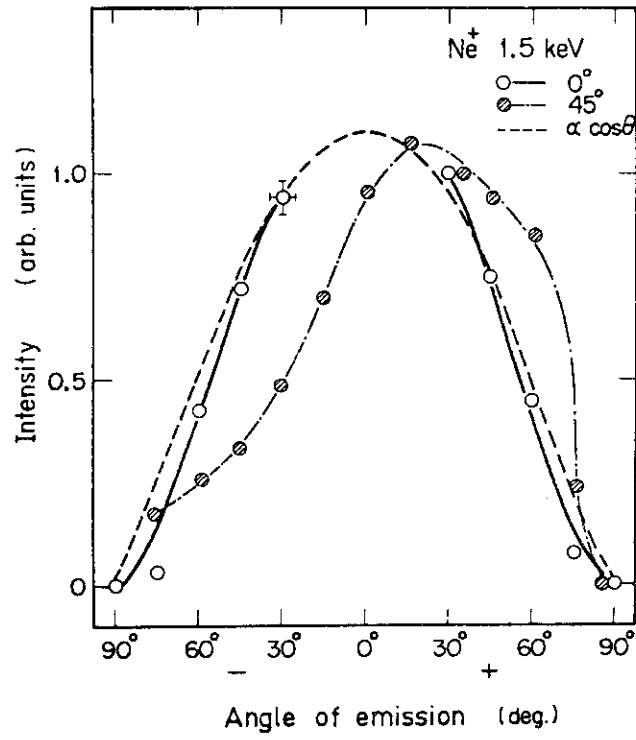


Fig.13 Angular distribution ($\phi = 0^\circ$) of sputtered Mo at $\alpha = 0^\circ$ and 45° by 1.5 keV Ne^+ ions. The total dose is $2 \times 10^{19} \text{ ions/cm}^2$ and the targets are non-annealed.⁸⁾

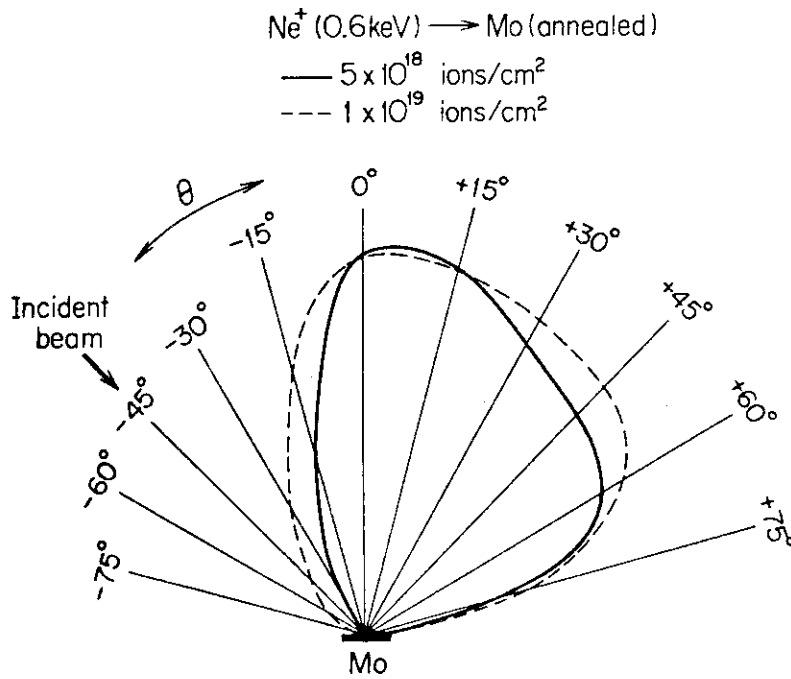


Fig.14 Angular distribution ($\phi = 0^\circ$) of sputtered Mo at $\alpha = 45^\circ$ by 0.6 keV Ne^+ ions. The target is annealed.⁸⁾

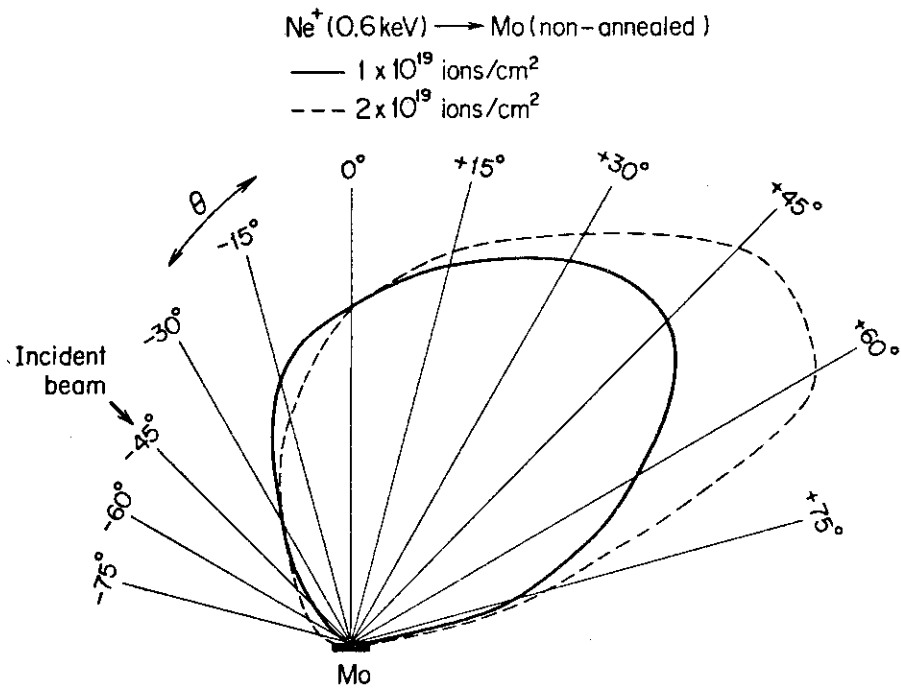


Fig.15 Angular distribution ($\phi = 0^\circ$) of sputtered Mo at $\alpha = 45^\circ$ by 0.6 keV Ne^+ ions. The target is non-annealed.⁸⁾

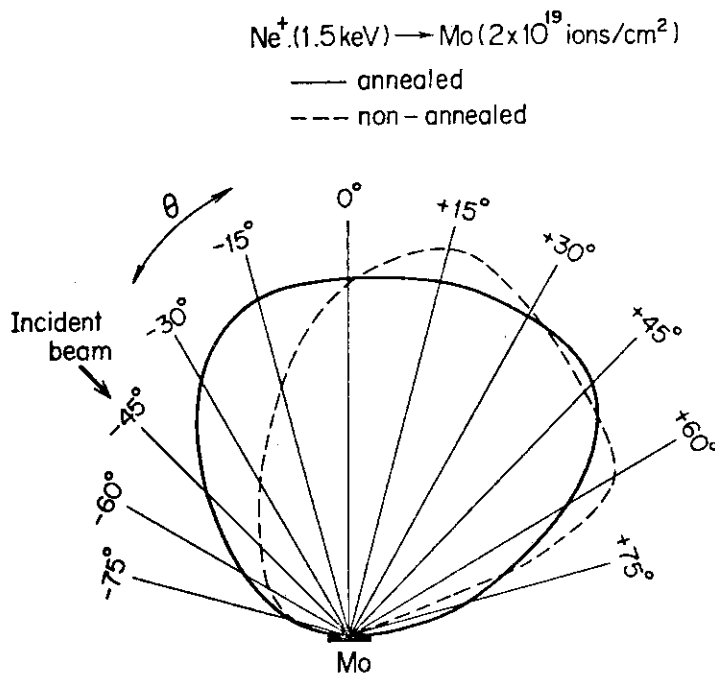


Fig.16 Angular distribution ($\phi = 0^\circ$) of sputtered Mo at $\alpha = 45^\circ$ by 1.5 keV Ne^+ ions. The total dose is $2 \times 10^{19} \text{ ions/cm}^2$.⁸⁾

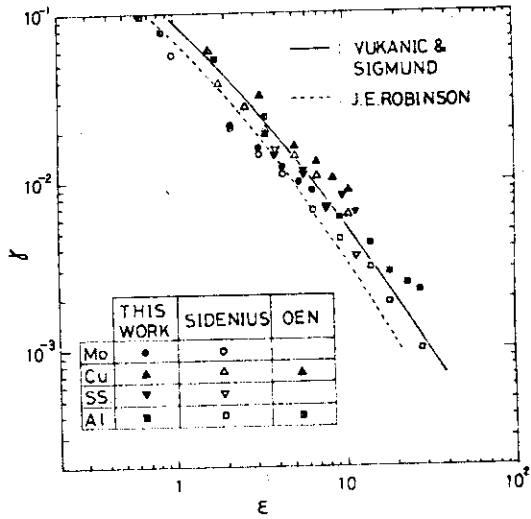


Fig.17 The energy reflection coefficient, γ , as a function of the reduced energy, ϵ . Also shown are the experimental results of Sidenius and Lenksjaer and the theoretical results of Oen and Robinson, J. E. Robinson and Vukanic and Sigmund.⁹⁾

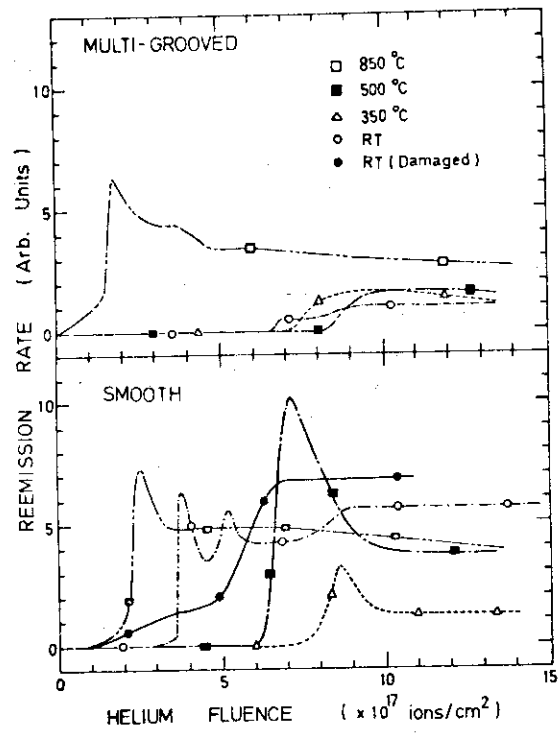


Fig.18 Helium re-emission rate as a function of the fluence of helium ions of 100 keV incident energy for multi-grooved and smooth molybdenum surfaces at various target temperatures. RT denotes room temperature bombardment, and RT (damaged) room temperature bombardment of molybdenum target pre-damaged with 100 keV helium to a fluence of 2×10^{18} ions/cm².¹⁰⁾

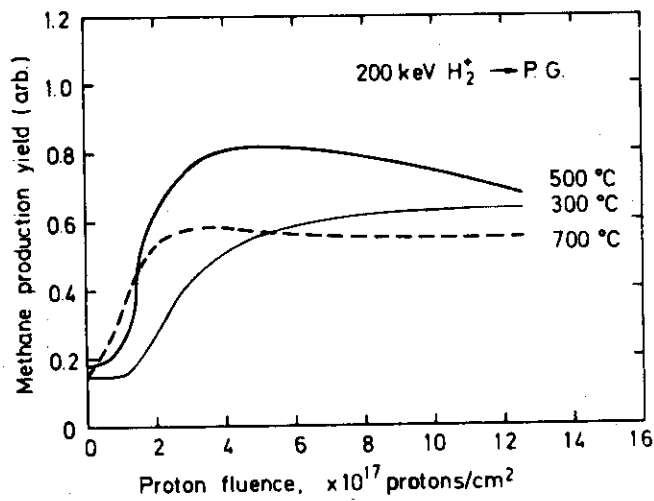


Fig.19 Methane production yield by the bombardment of pyrolytic graphite with 200 keV H_2^+ as a function of proton fluence.¹¹⁾

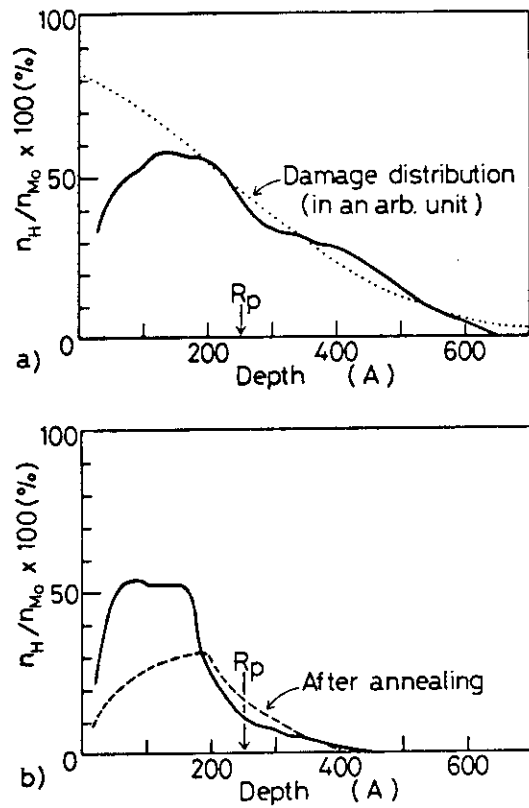


Fig.20 Depth profiles of 12-keV H_3^+ implanted in polycrystalline molybdenum at a dose rate of 0.18 mA/cm^2 to a dose of 0.95 C/cm^2 , where n_H and n_{Mo} are the number densities of hydrogen and molybdenum atoms, respectively; the projected range of 4-keV H^+ calculated with the LSS theory is indicated by R_p . (a) Profile for the implantation at 440 K (—) and one for the calculated damage distribution (.....). (b) Profile for the implantation at 780 K (—) and one after annealing at 780 K for 30 minutes (---).¹²⁾

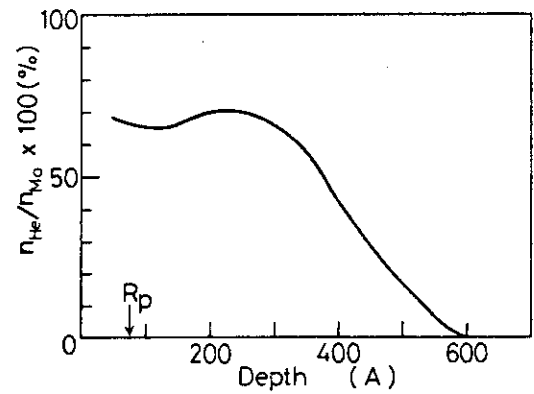


Fig.21 Depth profile of 2-keV He^+ implanted in polycrystalline molybdenum at a dose rate of 0.012 mA/cm^2 to a dose of 0.19 C/cm^2 at 300 K, where n_{He} is the number density of helium atoms; the projected range of 2-keV He^+ calculated with the LSS theory is indicated by R_p .¹²⁾

(ii) Blistering

(a) Introduction

Blistering is the surface deformation due to the internal gas pressure of the lenticular bubble formed in the sub-surface layer.

Following subjects have been investigated:

- Energy dependence of critical fluence for blistering and flaking.
- Energy dependence of blister diameter.
- Energy dependence of cover thickness in comparison with projected range.
- Temperature dependence of critical fluence.
- Blister size distribution.
- Relation between blister diameter and cover thickness.
- Estimation of erosion rate due to blistering.
- Direct measurements of erosion rate due to ion bombardments.
- Theoretical interpretation of blistering and flaking.

(b) Comments on Japanese works

Japanese investigations include following subjects:

- In-situ observations of blistering and flaking processes.¹⁾²⁾
- Investigations on Ne and Ar blisterings.³⁻⁸⁾
- Investigations of blistering and flaking on low Z materials (graphite and SiC).⁹⁻¹²⁾
- Effects of surface structures on blistering.¹³⁾¹⁴⁾
- Investigations on erosion processes.¹⁵⁻²²⁾
- Theoretical investigations of blistering and flaking on the basis of linear elasticity theory.²³⁻²⁶⁾

(c) Theoretical predictions on blistering

A critical relation between the radius a and the cover thickness h , both of a blister, is given by

$$0.81 \left(\frac{a}{h} \right)^{3.20} \left(\frac{P}{\sigma_{ys}} \right)^2 = 1. \quad (1)$$

The ratio of internal gas pressure P to plastic yield stress of material σ_{ys} , P/σ_{ys} , in Eq. (1) ranges, depending on the ion energy, from 0.05 to 0.2 for Ni, V and Nb, and from 0.017 to 0.04 for Be, empirically, in the energy range of 10 ~ 500 keV for He⁺.²⁵⁾

References

- 1) M. Saidoh, K. Sone, R. Yamada and H. Ohtsuka, JAERI-M 7997 (1978) in Japanese.
- 2) K. Kamada and H. Naramoto, to be published in Radiation Effects.
- 3) K. Hayashi, K. Fukuya, S. Ishino and Y. Mishima, submitted to First Topical Meeting on Fusion Reactor Materials, Bal Harbour, Florida, January 29-30 (1979).
- 4) M. Tanaka, K. Fukai and K. Shiraishi, JAERI-M 6585 (1976) in Japanese.
- 5) K. Kamada, Y. Kazumata and K. Kubo, Rad. Effects 28 (1976) 43.
- 6) K. Kamada, H. Naramoto and Y. Kazumata, J. Nucl. Mat. 71 (1978) 249.
- 7) H. Naramoto and K. Kamada, J. Nucl. Mat. 74 (1978) 186.
- 8) K. Kamada, unpublished work.
- 9) Y. Kazumata, J. Nucl. Mat. 68 (1977) 257.
- 10) Y. Kazumata, *ibid.* 71 (1977) 178.
- 11) K. Sone, T. Abe, K. Obara, R. Yamada and H. Ohtsuka, *ibid.* 71 (1977) 82.
- 12) S. Miyagawa, Y. Moriya and Y. Ato, unpublished work.
- 13) K. Sone, M. Saidoh, R. Yamada and H. Ohtsuka, J. Nucl. Mat. 76/77 (1978) 240.
- 14) M. Saidoh, K. Sone, R. Yamada, H. Ohtsuka and Y. Murakami, JAERI-M 7182 (1978).
- 15) Y. Nakamura, T. Shibata and M. Tanaka, J. Nucl. Mat. 68 (1977) 253.
- 16) K. Watanabe, M. Sasaki, M. Mohri and T. Yamashina, *ibid.* 76/77 (1978) 235.
- 17) K. Watanabe and T. Yamashina, J. Catalysis 17 (1970) 272.
- 18) K. Watanabe and T. Yamashina, J. Vacuum Soc. Japan 13 (1970) 327.
- 19) T. Kimura, S. Okuda, J. Kobayashi and H. Akimune, to be published in Jpn. J. Appl. Phys.
- 20) T. Kimura, S. Okuda, J. Kobayashi and H. Akimune, to be published in Jpn. J. Appl. Phys.
- 21) S. Okuda and H. Akimune, to be published in Jpn. J. Appl. Phys.
- 22) S. Okuda and S. Imoto, unpublished work.
- 23) Y. Higashida and K. Kamada, J. Nucl. Mat. 73 (1978) 30.
- 24) K. Kamada and Y. Higashida, *ibid.* 73 (1978) 41.
- 25) K. Kamada and Y. Higashida, to be published in J. Appl. Phys.
- 26) Y. Higashida and K. Kamada, unpublished work.

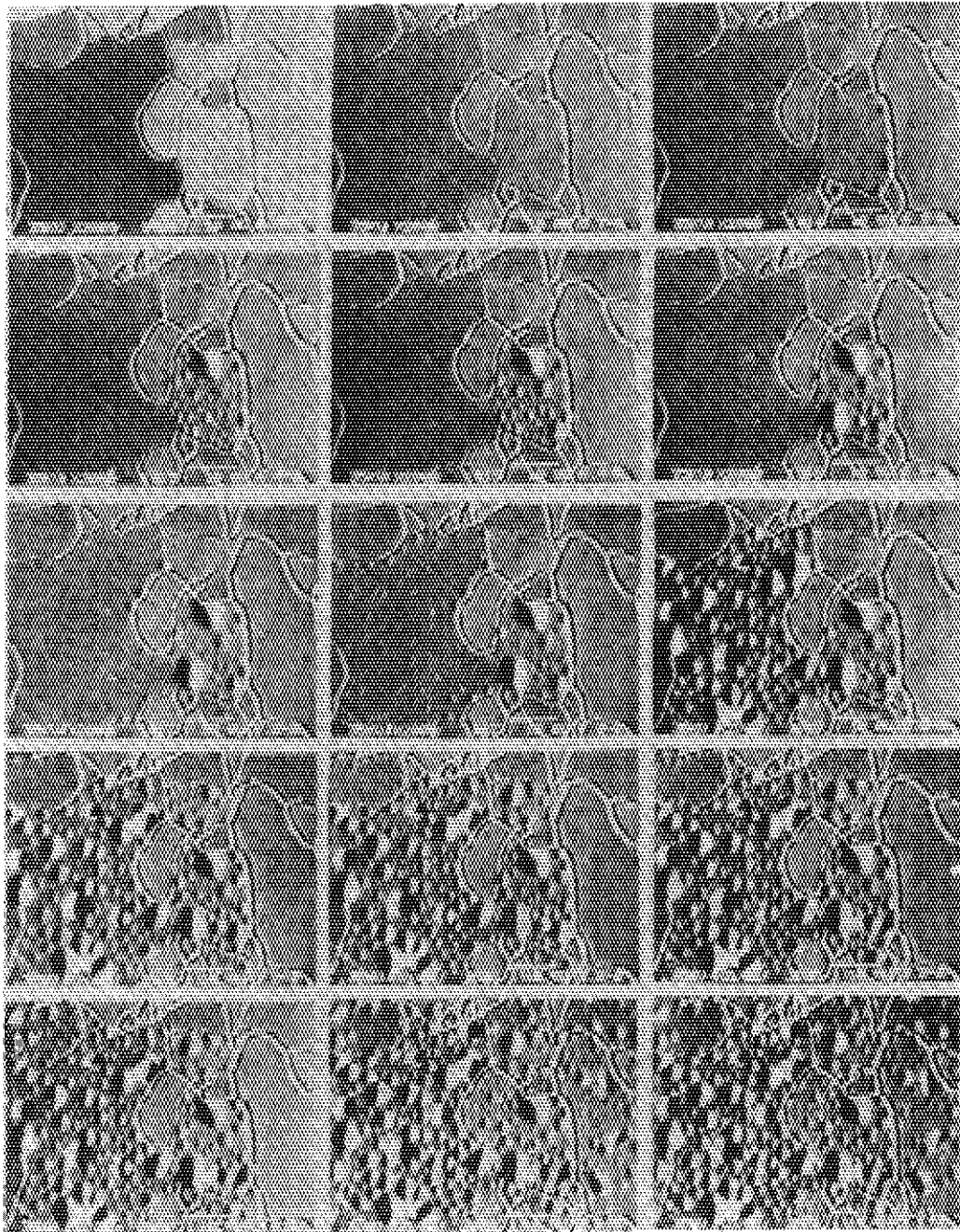


Fig.1 Scanning electron micrographs showing the development of surface erosion with 100keV He bombardment on Mo surface at room temperature. The ultimate dose is $9.0 \times 10^{17} \text{He}^+/\text{cm}^2$. Prior to the bombardment the target was annealed at 1300°C for 1 hour. Image contrast was made by detecting backscattered electrons.

450keVNe⁺ on Nb(100), Dose Rate=2.6x10¹⁴Ne⁺/cm²/sec.

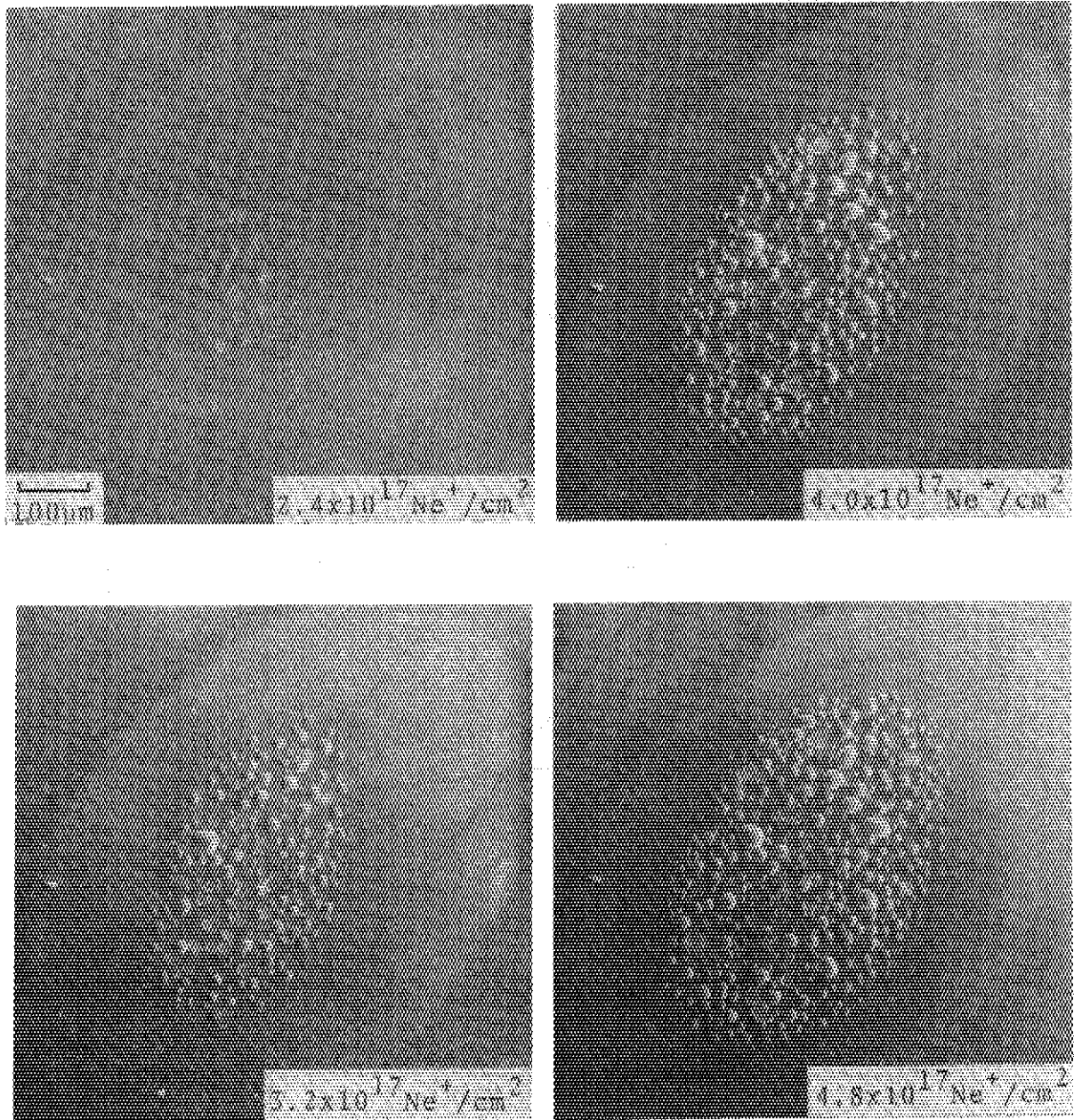


Fig.2 Successive observations of 450 keV Ne blistering on single crystalline Nb (100) surface at room temperature.

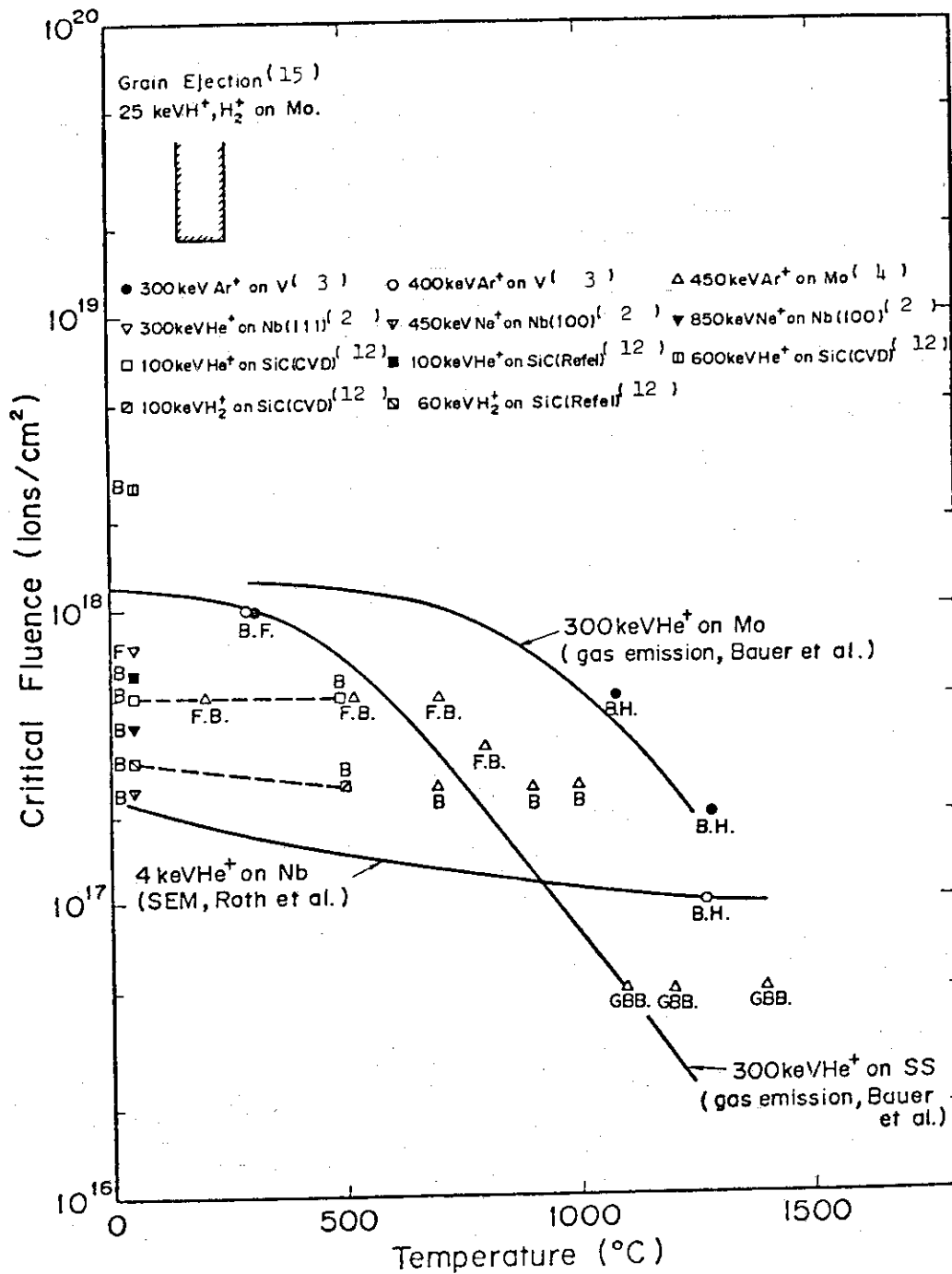


Fig.3 Temperature dependences of critical fluences of blistering and flaking measured by SEM. Data of Ar on metals were taken on subsequent annealing at each temperatures after the bombardments at room temperature. B,F and H attached on the data points specify blistering, flaking and hole formation, respectively. Curved lines show critical fluences of blistering measured by SEM or gas emission on the indicated systems.

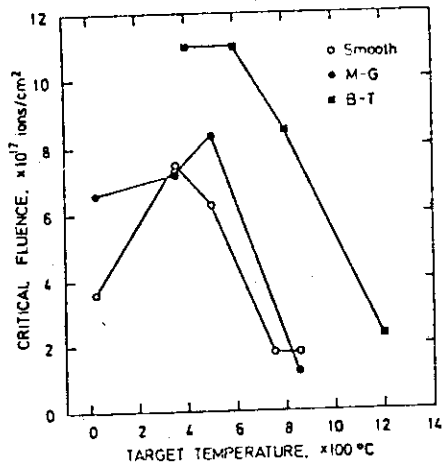


Fig. 4 Critical fluence of helium ions of 100 keV incident energy as a function of target temperature for multi-grooved (M-G) and smooth molybdenum surfaces. B-T denotes the experimental data by Bauer and Thomas in case of 300 keV helium ion bombardment of smooth surface.¹³⁾

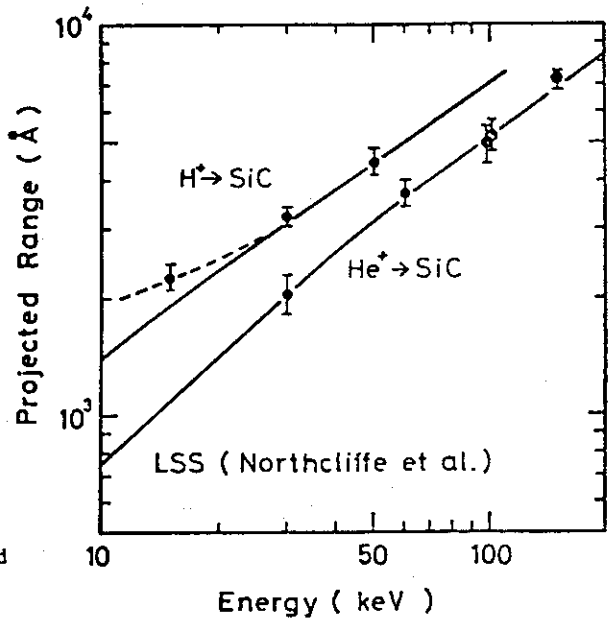


Fig. 5 Energy dependences of blister cover thickness, measured by SEM, and projected range, calculated by LSS theory, for H⁺ and He⁺ bombardments on SiC (CVD) at room temperature¹²⁾.

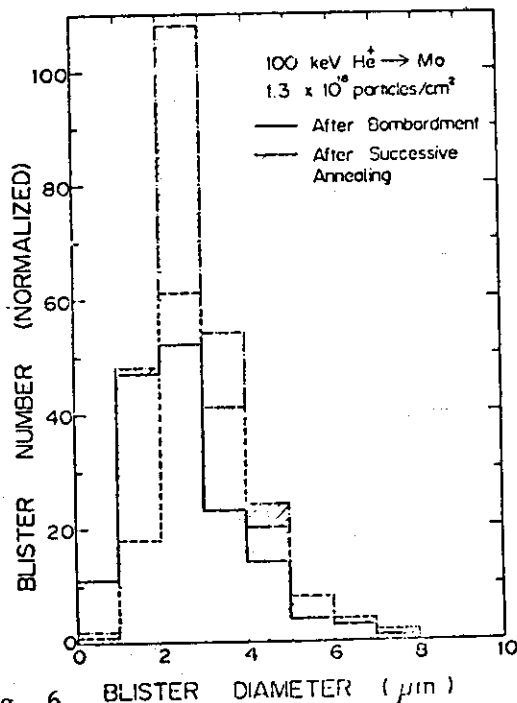


Fig. 6 Blister size distributions. Solid line shows after 100 keV helium bombardment to a fluence of 1.3×10^{18} He⁺/cm², chain line after successive annealing at 400 °C for 1 hour after bombardment and broken line size distribution of the blisters formed by the pre-bombardment after annealing.

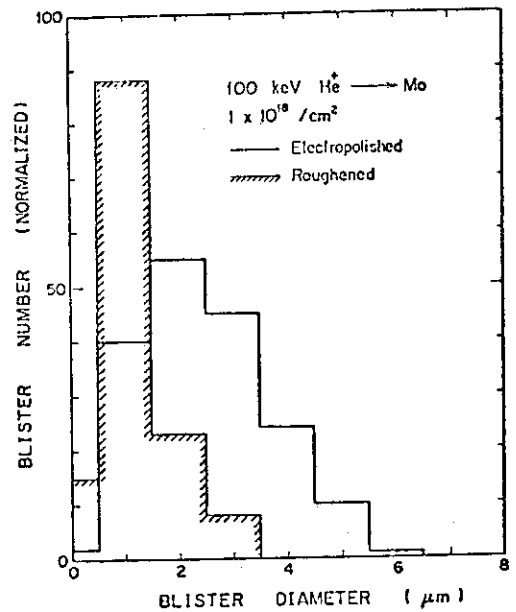


Fig. 7 Size distributions of blisters formed by 100 keV helium ion bombardment of molybdenum with electropolished surface (—) and rough surface abraded with emery paper of #1200 (---).¹⁴⁾

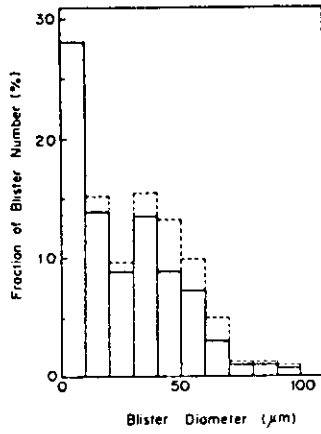


Fig. 8 Distribution of blister diameters measured on single crystalline Nb (100) surface after the bombardment with 850 keV Ne⁺ at -130 °C.⁷⁾

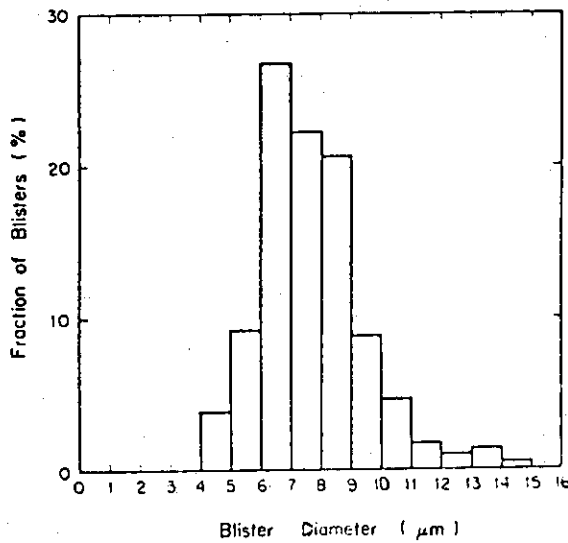


Fig. 9 Distribution of blister diameter measured on Ge surface by bombardment with 450 keV Ar⁺ at room temperature.⁸⁾

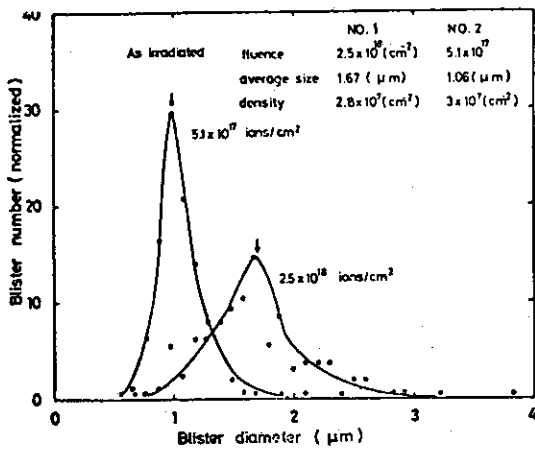


Fig. 10 Size distribution of argon blisters produced by argon ion bombardment.

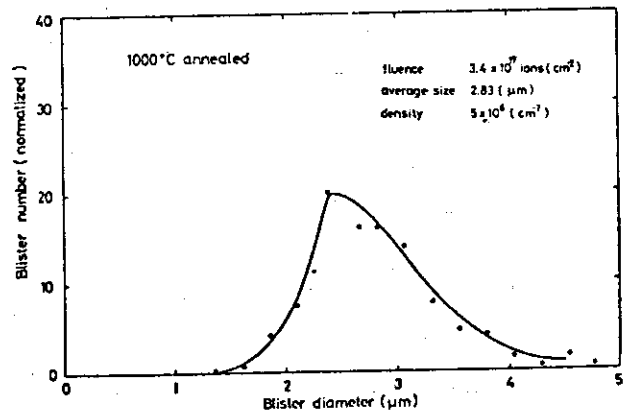


Fig. 11 Size distribution of argon blisters produced by argon ion bombardment and annealing.

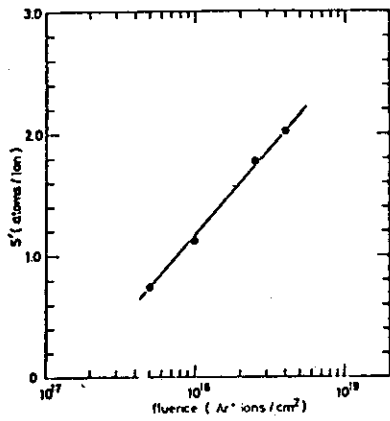


Fig. 12 Change in surface erosion rate (S') with Ar^+ dose in molybdenum bombarded at ambient temperature¹⁹⁾

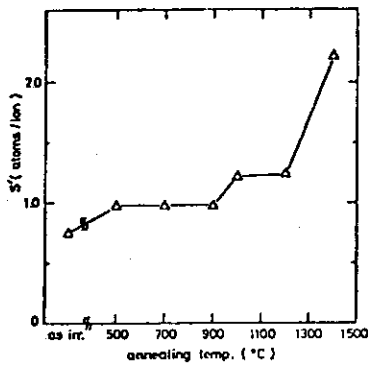


Fig. 13 Change in surface erosion rate (S') with annealing temperature in molybdenum bombarded with Ar^+ ion to 5.1×10^7 ions/cm² at ambient temperature¹⁹⁾

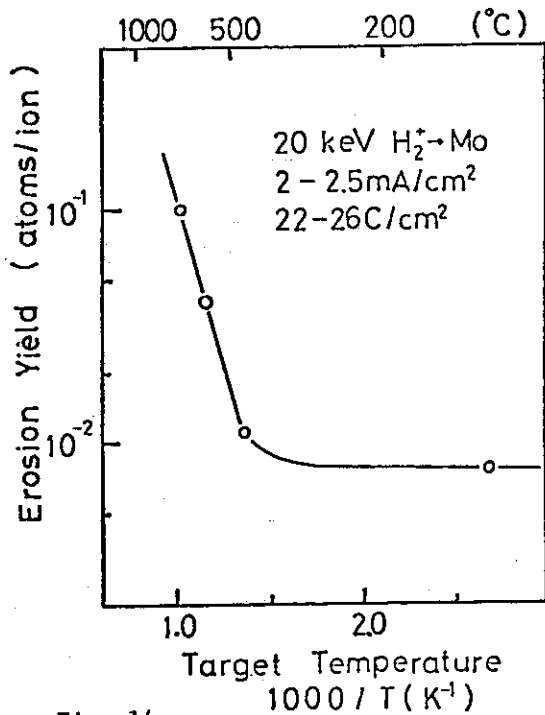


Fig. 14 Temperature dependence of erosion yield of polycrystalline Mo surface bombarded with $20 \text{ keV } H_2^+$ up to doses of $22-26 \text{ C/cm}^2$ ¹⁹⁾

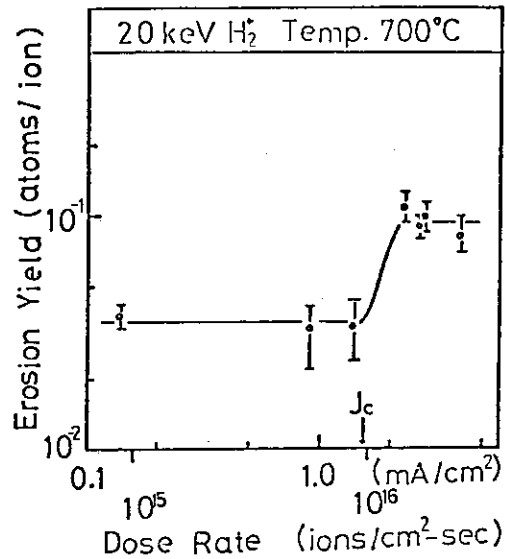


Fig. 15 Dose dependence of erosion yield of polycrystalline Mo surface bombarded with $20 \text{ keV } H_2^+$ ¹⁹⁾

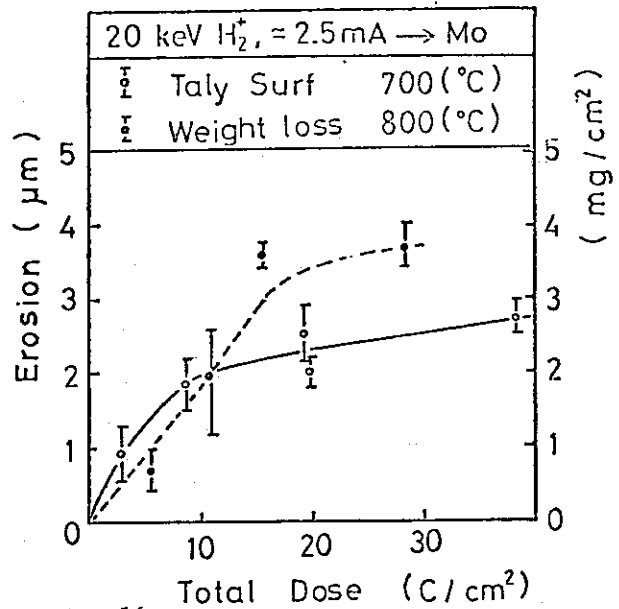


Fig. 16 Dose dependence of surface erosion of polycrystalline Mo bombarded with $20 \text{ keV } H_2^+$ ¹⁹⁾

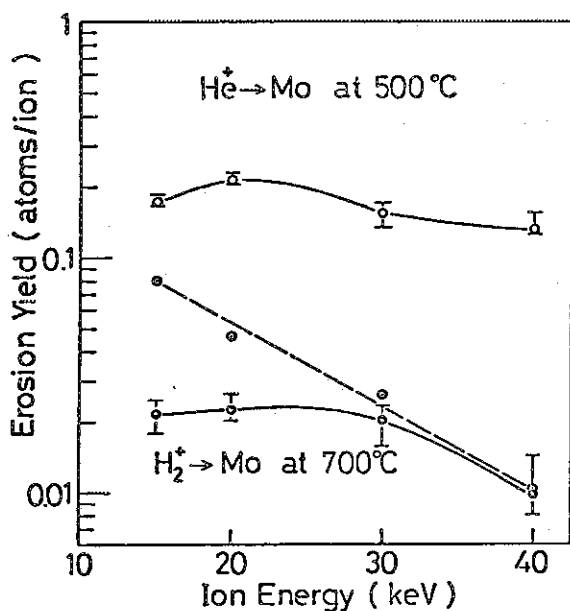


Fig. 17
Energy dependences of average erosion yields of polycrystalline Mo surfaces bombarded with following conditions; He⁺ with dose-rate of 0.8-1.2 mA/cm² up to dose of 5-6 C/cm² at 500 °C, and H₂⁺ with 1.3-1.5 mA/cm² up to 18-22 C/cm² at 700 °C. Dashed line shows the maximum erosion yields observed in relatively low dose range of H₂⁺ bombardment.²¹⁾

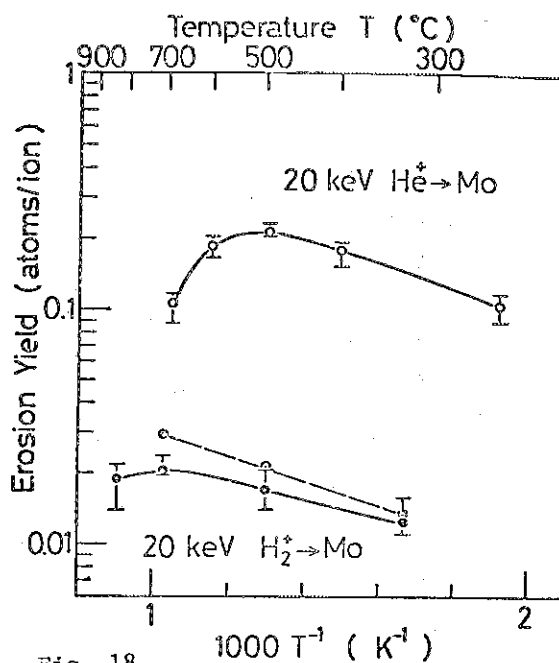


Fig. 18
Temperature dependences of erosion yields, averaged over wide dose range, of polycrystalline Mo surface bombarded with following conditions; 20 keV He⁺ at dose-rate of 1.1-1.3 mA/cm² up to 5-7 C/cm², and 20 keV H₂⁺ of 1.3-1.5 mA/cm² up to dose of 19 C/cm². Dashed line shows the maximum erosion yield observed at relatively low dose range of H₂⁺ bombardment.²¹⁾

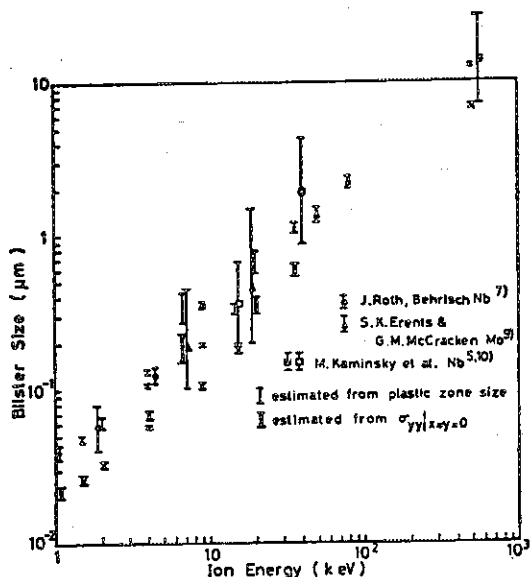


Fig. 19
Comparison of the theoretical results obtained by eq.(1) with experimental results on Mo and Nb.²⁵⁾

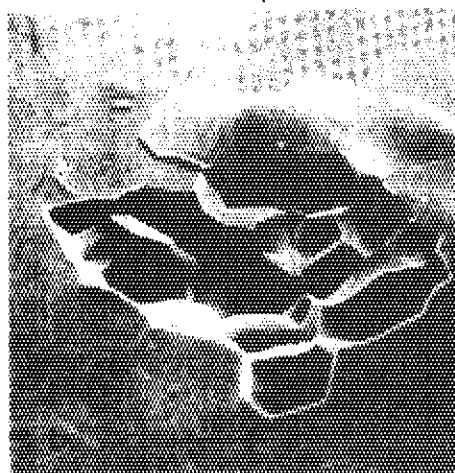


Fig. 20 Grain ejection observed on polycrystalline Mo surface after the bombardment up to 3 C/cm² with 25 keV H⁺ at 200 °C.¹⁵⁾